AUTOMATED DETECTION OF DISCONTINUITY PROPERTIES USING TERRESTRIAL LASER SCANNING DATA

A THESIS SUBMITTED TO
THE GRADUATE SCHOOL OF NATURAL AND APPLIED SCIENCES
OF
MIDDLE EAST TECHNICAL UNIVERSITY

BY

DENİZ ÜNLÜSOY

IN PARTIAL FULFILLMENT OF THE REQUIREMENTS
FOR
THE DEGREE OF DOCTOR OF PHILOSOPHY
IN
GEOLOGICAL ENGINEERING

DECEMBER 2020

Approval of the thesis:

AUTOMATED DETECTION OF DISCONTINUITY PROPERTIES USING TERRESTRIAL LASER SCANNING DATA

submitted by **DENİZ ÜNLÜSOY** in partial fulfillment of the requirements for the degree of **Doctor of Philosophy** i**n Geological Engineering, Middle East Technical University** by,

Prof. Dr. Halil Kalıpçılar
Dean, Graduate School of **Natural and Applied Sciences** _____

Prof. Dr. Erdin Bozkurt
Head of the Department, **Geological Engineering, METU** _____

Prof. Dr. Mehmet Lütfi Süzen
Supervisor, **Geological Engineering, METU** _____

Examining Committee Members:

Prof. Dr. A. Aydın Alatan
Electric and Electronics Engineering, METU _____

Prof. Dr. M. Lütfi Süzen
Supervisor, Geological Engineering, METU _____

Prof. Dr. B. Taner San
Geological Engineering, Akdeniz University _____

Assist. Prof. Dr. A. Arda Özacar
Geological Engineering, METU _____

Assist. Prof. Dr. Özgür Aktürk
Geological Engineering, Akdeniz University _____

Date: 24.12.2020

I hereby declare that all information in this document has been obtained and presented in accordance with academic rules and ethical conduct. I also declare that, as required by these rules and conduct, I have fully cited and referenced all material and results that are not original to this work.

Name, Last name : Deniz Ünlüsoy

Signature :

ABSTRACT

AUTOMATED DETECTION OF DISCONTINUITY PROPERTIES USING TERRESTRIAL LASER SCANNING DATA

Ünlüsoy, Deniz
Doctor of Philosophy, Geological Engineering
Supervisor : Prof. Dr. Mehmet Lütfi Süzen

December 2020, 182 pages

Traditional ground surveying methods for the determination of rock mass discontinuity characteristics are costly and time consuming when large survey areas are involved. In addition, some rock mass surfaces cannot be observed with ground, airborne, or satellite surveying methods. Terrestrial laser scanning offers new avenues in fieldwork, making the acquisition of large amounts of survey data possible. However, there is a need for new approaches and accompanying software for the analysis of such data. In this study, a methodology that uses point cloud data obtained by terrestrial laser scanning is developed and implemented by a software for automated analyses of the physical properties of discontinuities of rock masses. The software processes the point cloud data of the outcrop surface and detects planar structures using density-based scanning on surface normals to determine discontinuity sets. For each set, orientation, spacing, persistence, block size, and roughness are calculated. This study also proposes a novel, simple, accurate, and reliable method for the estimation of joint roughness coefficient from terrestrial laser scanning data using power spectral density. The method is based on the similarity of sample and reference surface profiles by their power spectral density. The accuracy

and the reliability of the proposed method is validated by comparison with the classical methods and back-calculated results obtained from the literature. The method is then extended to estimate the JRC of entire surfaces using multiple profiles. This areal JRC estimation method is applied on point cloud data of a rock outcrop for a case study.

Keywords: Remote Sensing, Terrestrial Laser Scanning, Discontinuity, Power Spectral Density, Joint Roughness Coefficient

ÖZ

KARASAL LAZER TARAMA VERİLERİ KULLANARAK SÜREKSİZLİK ÖZELLİKLERİNİN OTOMATİK BELİRLENMESİ

Ünlüsoy, Deniz
Doktora, Jeoloji Mühendisliği
Tez Yöneticisi: Prof. Dr. Mehmet Lütfi Süzen

Aralık 2020, 182 sayfa

Kaya kütlesi süreksizlik özelliklerinin belirlenmesi için geleneksel zemin etüt yöntemleri, büyük etüt alanları söz konusu olduğunda yüksek maliyetli ve zaman alıcıdır. Buna ek olarak, bazı kaya kütlesi yüzeyleri kara, hava veya uydu ölçüm yöntemleri ile gözlemlenemeyebilir. Karasal lazer tarama, saha çalışmasında yeni yöntemler sunar ve büyük miktarda saha verisinin elde edilmesini mümkün kılar. Ancak, bu tür verilerin analizi için yeni yaklaşımlara ve uygulama yazılımına gereksinim vardır. Bu çalışmada, kaya kütlelerinin süreksizliklerinin fiziksel özelliklerinin otomatikleştirilmiş analizleri için karasal lazer taraması ile elde edilen nokta bulutu verilerini kullanan bir metodoloji ve uygulama bir yazılımı geliştirilmiştir. Yazılım, çıkıntı yüzeyinin nokta bulutu verilerini işler ve süreksizlik kümelerini belirlemek için yüzey normları üzerinde yoğunluğa dayalı tarama kullanarak düzlemsel yapıları bulur. Her küme için, oryantasyon, aralık, açıklık, kalıcılık, blok boyutu ve pürüzlülük hesaplanır. Bu çalışma aynı zamanda güç spektral yoğunluğu kullanarak karasal lazer tarama verilerinden eklem pürüzlülük katsayısının tahmini için yeni, basit, doğru ve güvenilir bir yöntem önermektedir. Yöntem, örnek ve referans yüzey profillerinin güç spektral yoğunlukları ile benzetimlerine dayanmaktadır. Önerilen yöntemin doğruluğu ve güvenilirliği, klasik

yöntemlerle ve literatürden elde edilen deneysel verilerden elde edilen sonuçlarla karşılaştırılarak doğrulanmıştır. Yöntem daha sonra çoklu profiller kullanılarak tüm yüzeylerin JRC'sini tahmin etmek için genişletilmiştir. Bu alansal JRC tahmin yöntemi, vaka çalışması için bir kaya çıkıntısının nokta bulutu verilerine uygulanmıştır.

Anahtar Kelimeler: Uzaktan Algılama, Karasal Lazer Tarama, Süreksizlik, Güç Spektral Yoğunluğu, Eklem Pürüzlülük Katsayısı

To my family

ACKNOWLEDGMENTS

Firstly, I would like to express my sincere gratitude to my advisor Prof. Dr. M. Lütfi Süzen for the continuous support of my Ph.D. study and related research for his patience, motivation, and knowledge. His guidance helped me throughout my research and writing of this thesis. I am fortunate to have him as my advisor and mentor for my Ph.D. study.

Besides my advisor, I would like to thank the rest of my thesis committee: Assist. Prof. Dr. A. Arda Özacar and Prof. Dr. B. Taner San, for their insightful comments and encouragement, but also for the constructive criticism which incented me to improve my research from various perspectives.

Last but not least, I would like to thank my family. I thank my father for encouraging me to start my Ph.D. study and continual support me throughout my studies. I thank my mother for giving her spiritual support throughout the thesis process and my life in general.

TABLE OF CONTENTS

LIST OF TABLES

TABLES

LIST OF FIGURES

FIGURES

CHAPTER 1

INTRODUCTION

1.1 Definition of the Problem

Discontinuities are among the most important characteristics when analyzing the structure of a rock mass. In geotechnical engineering, a discontinuity is a plane or surface that defines a change in physical or chemical characteristics in a soil or rock mass. A discontinuity can be bedding, schistosity, foliation, joint, cleavage, fracture, fissure, crack, or fault plane. The identification of the properties of physical discontinuities is essential to the determination of the mechanical properties of a rock mass.

The basic properties that describe a discontinuity are orientation, spacing, persistence, roughness, wall strength, aperture, filling, seepage, number of sets, and block size. The definitions of these properties are listed below, as given by the International Society for Rock Mechanics (ISRM), 1978c:

- Orientation of a discontinuity is specified by the dip angle and the dip direction.

- Discontinuity spacing is the distance between successive discontinuities along a scanline.

- Persistence is the observed discontinuity trace length. It gives a rough measure of the extent/penetration length of a discontinuity.

- Roughness includes roughness and waviness of a surface and measured with respect to the mean plane of a discontinuity.

- Wall strength is the effective compressive strength of the bordering rock walls of a discontinuity.

- Aperture is the perpendicular distance between adjacent rock walls of a discontinuity. The space between layers is filled with air or water.

- Filling is the material that separates the rock walls of a discontinuity. It is generally weaker than the rock walls.

- Seepage is the water flowing and the visible moisture in individual discontinuities or in the entire rock mass.

- Number of Sets is the number of discontinuity sets of the intersecting discontinuity system.

- Block size is the dimension of the rock blocks formed by the intersection of discontinuity sets.

The properties listed above are the physical descriptions of a discontinuity or joint. Discontinuities are planes of weakness relative to surrounding rock mass, in which the tensile strength perpendicular to the discontinuity or the shear strength along the discontinuity is lower. Thus, these properties are essential in determining the strength of the rock mass just as the types of rocks forming the rock mass. Discontinuity properties find use in engineering applications wherever jointed rock masses are present. Slope stability analysis, mining, tunneling, and dam construction are some of the many examples in which shear strength of jointed rock masses play a vital role, Figure 1.1. The failure criterion and safety factor of rock masses depend on the shear and tensile strength of rock masses which in turn are calculated using properties of discontinuities present in the rock mass (Priest, 1993).

Figure 1.1. Effects of discontinuity orientation on slope stability. (a) Persistent J1 discontinuities dipping out of face forms potentially unstable sliding blocks, (b) closely spaced, low persistence discontinuities cause ravelling of small blocks, (c) persistent J2 discontinuities dipping into face form potential toppling slabs, Wyllie and Mah (2004).

For the detailed examination and analysis of geological structures, classical ground-based fieldwork has been the usual approach. The need to cover large areas led geologists to utilize airborne and satellite platforms to collect data. However, problems still arise in cases such as the presence of vegetation cover, vertical wall of the outcrop, dug up trenches, or outcrop properties too small to be seen by satellite or airborne images. Thus these surveys often require accompanying fieldwork for detailed examination. Therefore, ground-based surveying is still essential for the examination of geological structures.

However, classical ground surveys to analyze discontinuities on a regional scale with long scan lines require large numbers of samples to be taken and analyzed. Therefore, standardized conventional procedures followed in the field for the determination of discontinuity properties of rock masses tend to be time-consuming, laborious, and costly (Priest, 1993). Further, outcrops that are difficult to approach on the ground may involve safety risks and may even be impossible to realize in cases where rock faces are inaccessible.

One relatively recent solution to overcome the hardships of groundwork is the use of Terrestrial Laser Scanning (TLS) which is a remote sensing tool. TLS allows surveyors to obtain a three-dimensional (3D) image of the outcrop from a distance without spending much time and exposing no one to the hardships of the terrain, as shown in Figure 1.2. Therefore, in the last decade or so, manual field survey procedures have been mostly replaced by TLS based surveying techniques which

alleviate most of the disadvantages associated with the conventional manual field surveys. TLS approach allows fast and low-cost collection of point cloud data which are later processed to obtain the relevant properties of discontinuities, among which are the orientation, spacing, persistence, and roughness properties.

Figure 1.2. TLS data acquisition of a basalt quarry, Gomes et al. (2016).

The 3D dataset obtained by TLS is called point cloud data. Global Positioning System (GPS) is used to determine the coordinates of the starting point, i.e. when the TLS device is activated. From there on, surfaces recorded are formed by points with x, y, and z coordinates relative to the starting coordinates. The 3D surface data then can be analyzed in the laboratory in detail. However, it is also possible to analyze outcrops in the field using a portable computer with software that can perform the analysis.

Despite all the advantages of TLS, the success of the modeling and analysis fully depends on the algorithms developed to process the data collected for the specific targets of the study. Many different software dedicated to analyzing point cloud data and creating models of geological structures are being developed every day.

Substantial research effort is devoted to the development of improved collection, analysis, and processing presentation of the point cloud data for better automation and accuracy.

1.2 Motivation

Traditional fieldwork involves mechanical tools like compasses for orientation and profilometers for roughness determination. These methods may not faithfully represent the actual conditions as they are somewhat open to the subjectivity of the surveyor and analyst, and thus lack precision. Although more advanced tools exist, they are mostly restricted for laboratory use and can only examine samples brought from the field. In fieldwork, discontinuity samples are often taken in large intervals in order to reduce time and cost. In certain projects, however, it is imperative to take a large number of samples along long scanlines. In such cases, it is desirable to have tools for automatic data collection and analysis. TLS fulfills the first requirement providing the cloud data. TLS technology provides the opportunity for more objective analysis in the field comparable to the laboratory equipment and more data than samples taken from the field can provide. Yet, TLS itself can only provide a large number of data points and the evaluation of the properties from the cloud data still presents a formidable task. An analysis methodology making use of computer power, in an automatic or at least semi-automatic manner, could provide the solution to the second requirement. Thus the point cloud data should be analyzed by special software developed for this purpose.

The main target of this study is to develop a software that can automatically determine selected discontinuity properties for large amounts of data obtained for a surface of interest with simple, accurate, and reliable methods. It is envisioned that this software will be used during fieldwork, as soon as cloud data obtained by TLS is ready to be processed. In order to go through this large amount of data, the analysis process must be as automatic as possible with minimal input from the user.

Literature survey reveals that some TLS software has been developed in various studies carried out for geological analysis. However, these algorithms are mostly specialized for the analysis of individual or selected sets of discontinuity properties (Mah et al., 2011, Riquelme et al., 2015). The algorithms in the software to be developed in this study will be aimed to provide the best choices for the extraction of relevant information for almost all of the significant discontinuity properties that can be derived from TLS data.

Recent technological developments, including the development of TLS and computer software for processing cloud data, have made it possible to obtain discontinuity surfaces on long scan lines. There is still left the long and tedious task of estimating the Joint Roughness Coefficient (JRC) values for the large number of profiles obtained from these surfaces. In the context of the TLS data processing, the literature survey has shown that the existing methods for the estimation of the JRC have not yet been sufficiently matured to produce an objective and accurate result that can be integrated into the general software. Thus, during the study, one of the major subjects has been the development of a method that will satisfy the requirements of objectivity, reliability, and accuracy.

1.3 Scope

The methodology developed and implemented in the software is used to determine the discontinuity properties of rock mass surfaces obtained by TLS. First, the cloud data is pre-processed by the selection of the study area and removal of the outliers. The next step is the determination of the orientation, spacing, persistence, block size, roughness, and the number of sets of discontinuities.

The TLS cloud data does not include characteristics such as color and water content. Thus, filling and seepage cannot be determined by the analysis of TLS data. Aperture often cannot be differentiated from spacing and filling in point cloud data. Wall strength, on the other hand, is a characteristic that should be calculated rather than directly obtained from TLS data. As a result, the discontinuity properties of interest are limited to orientation, spacing, persistence, block size, roughness, and the number of sets of discontinuities.

JRC is one of the important parameters to determine the shear strength of joints for the calculation of the shear strength of joints in rock. This parameter can only be back-calculated for a definitive value. Numerous methods have been proposed for the estimation of JRC without relying on back-calculation. The software also includes a novel method for the estimation of JRC of sample surface profiles using power spectral density.

The scope is limited to finding parameters that can be used in the calculation of shear strength of discontinuities. The properties obtained here can later be used in other software to calculate additional rock mass discontinuity parameters such as shear strength, rock mass index, etc.

1.4 Contributions

This study includes two novel contributions. First is the development of a method implemented in a graphical user interface (GUI) on the Matlab (2019a) platform, that incorporates a sequential methodology to calculate and determine discontinuity properties including orientation, spacing, frequency, persistence, block size, roughness, and the number of sets from TLS point cloud data. Even though there exists a large number of publications in the literature related to the processing of the point cloud data, most of these publications involve processes relevant to the application or the particular property of interest in the study. Therefore, the selection of the methods of analysis in each step may not be compatible when all the properties

are to be considered. The methodology used in the developed Matlab algorithm is structured to achieve high efficiency in the determination of all the significant properties of discontinuities automatically under a single software application, instead of relying on multiple specialized software. The Matlab GUI also allows processing vast amounts of data in a relatively short time and allows use in the field when necessary. Further, it is usable for incorporation as a module in a general software.

The second contribution is a novel method for the estimation of JRC of discontinuity surface profiles. The conventional method of estimating JRC in ISRM is based on a profilometer to get a profile of the surface of interest. This surface profile is then compared with ten reference JRC profiles provided by Barton and Choubey's (1977) in order to estimate its JRC value. This procedure is prone to be subjective as different analysts may reach different conclusions as reported in the literature. The basic method of finding JRC is the back-calculation from the laboratory test of the shear strength of the discontinuity. However, such an approach is not suitable for the analysis of the large number of samples that may be required for long scan lines. As noted in the literature survey, there are a considerable number of methods in the literature for the estimation of the JRC value. However, they all involve a certain level of error and they are applicable to the particular samples used in the original studies. Thus, the subject is still open to improvement. In this study, a novel and accurate method for JRC estimation using Power Spectral Density (PSD) is proposed. The proposed method is relatively simple and efficient. It is based on the PSD of the surface profile and involves a minimum number of steps of analysis, and the algorithm can be suitably embedded as a module in a large software. The method has been tested on a large number of surface profiles available in the literature and is shown to provide more accurate and precise results compared with the commonly used methods.

1.5 Organization of the Thesis

The first chapter of this thesis is devoted to provide a brief introduction to the fundamental concepts as well as the motivation and scope of the study. The second chapter includes the review of literature related to TLS technology with a primary focus on the application to geological engineering. Another focus of interest is on the literature related to the estimation of the JRC. The third chapter deals with the definitions, significance, and characteristics of discontinuities.

A general block diagram for the main body of the thesis study is given in Figure 1.3. In accordance with this work structure, the fourth chapter deals with the format, registration, outlier removal of the TLS cloud data. The fifth chapter presents the plane detection algorithms. The detailed information on the evaluation of potential plane fitting methods as well as classification and clustering methods are presented in this chapter. The algorithms of the selected methods are also included here. The sixth chapter is dedicated to the estimation of JRC. The details of the proposed novel, objective, accurate, and reliable method are presented in this chapter. In chapter seven, a case study with the developed software 'Discontinuity Analysis' is carried out step by step. The eighth chapter is an extension of the novel JRC estimation method from single profiles to entire surface areas. The areal JRC is applied on a rock outcrop point cloud data as a case study. The thesis ends with the ninth chapter which contains the conclusions of the study and recommendation for future work in the subject.

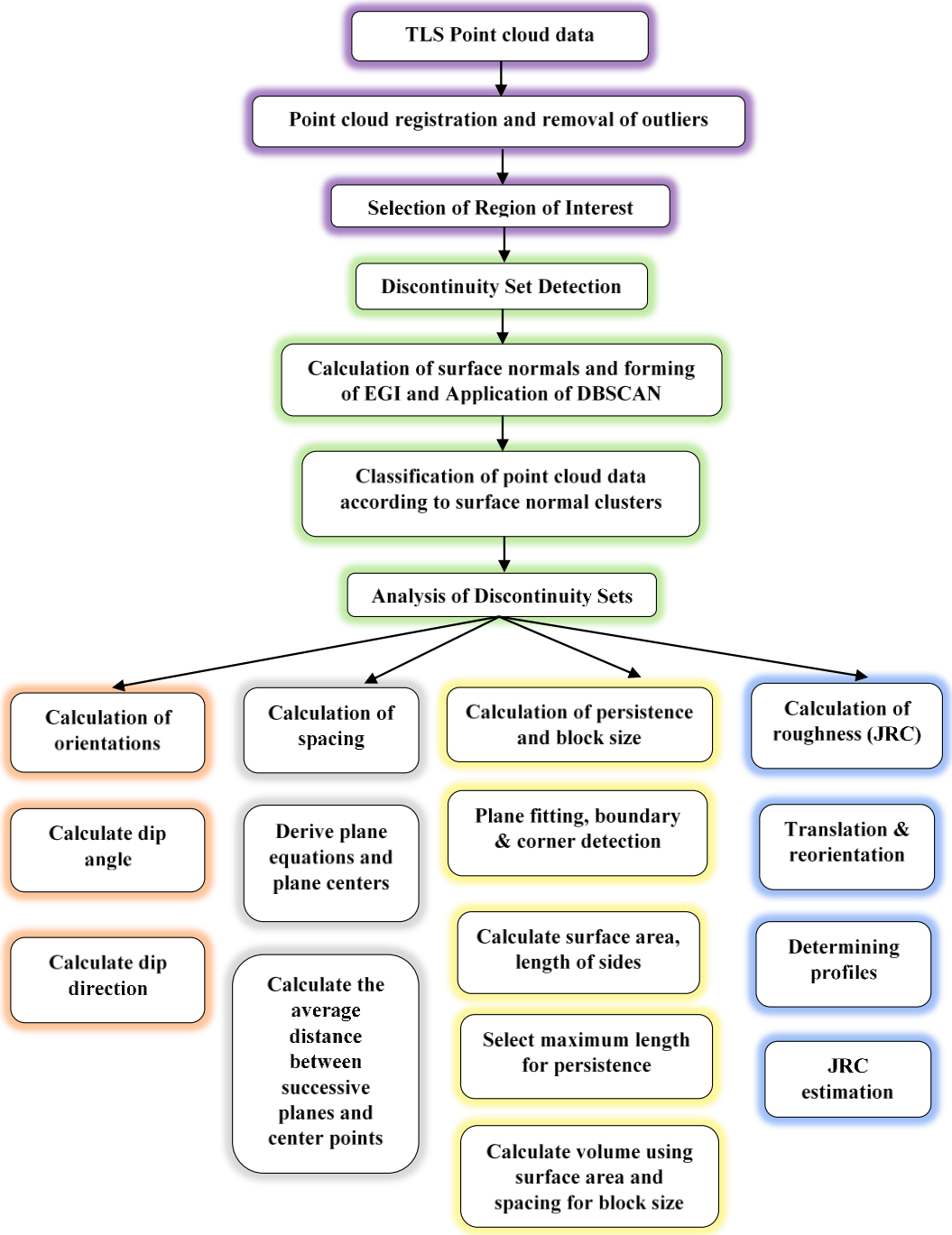

Figure 1.3. Block diagram of the main body of the study.

CHAPTER 2

LITERATURE REVIEW

Many methods have been proposed for the collection of TLS data to analyze the discontinuity properties of rock masses. Although the literature covers a wide variety of such publications, this review will focus on several themes that emerge repeatedly throughout the literature reviewed, with a primary focus on their application to geological engineering. These themes are TLS technology, geological applications of TLS, and JRC estimation.

One of the significant outcomes in the determination of joint properties by the TLS approach is the estimation of the shear strength of rock joints. A significant part of this study is concerned with the development of a novel method for the estimation of the JRC. Thus, the third focus of interest will be on the literature related to this subject.

2.1 Terrestrial Laser Scanning Technology

Terrestrial laser scanning has been in development since the start of the 21st century. Thus, it is a new technology and originally meant for surveying applications where very precise distances and angles are required. TLS is based on distance measurement using laser pulses. It makes 3D location within mm accuracy, potentially over hundreds of meters, possible. Improving TLS and Light Intensity Detecting and Ranging (LiDAR) technology is the main topic of numerous articles. One such example is the proposal by Carrera et al. (2016) for a new terrestrial LiDAR intensity correction which takes into consideration the range, the incidence angle,

and the geometry of the scanned surfaces. The corrected intensity values significantly improve material differentiation.

Schofield et al. (2016), introduced a novel dual wavelength full waveform TLS for measuring forest canopies called The Salford Advanced Laser Canopy Analyzer (SALCA). The sophistication of the radiometric response to the range, reflectance, and laser temperature seen in the results display that apparent reflectance can be estimated accurately by neural networks for both wavelengths. New opportunities for quantitative data analysis become available when the trained network is used to calibrate full hemispherical scans in a forest environment.

Yang et al. (2016), stated in their study that point clouds collected by TLS from large-scale urban scenes contain a wide variety of objects (buildings, cars, pole-like objects, and others) with symmetric and incomplete structures, and relatively low-textured surfaces, all of which pose great challenges for automatic registration between scans. To address the challenges, the paper proposed a registration method to provide marker-free and multi-view registration based on the semantic feature points extracted. Experiments have demonstrated that the proposed method performs well in various urban environments and indoor scenes with accuracy at the centimeter level and improves the efficiency, robustness, and accuracy of registration in comparison with the feature plane-based methods.

Tan and Cheng (2016), in their study, investigated the impacts of incidence angle and distance on intensity data of the Faro Focus3D 120 TLS. They proposed a new technique which eliminates the incidence angle and distance effects. The linear interpolation of the intensity values of reference targets previously scanned at different incidence angles and distances form the basis of the proposed method. An important advantage of this method compared to available methods is the estimation of the specific function forms of incidence angle versus intensity and distance versus intensity is no longer required. These are cancelled out when the scanned and reference targets are measured at the same incidence angle and distance. The results indicate the proposed method is simple and accurate for the elimination of incidence

angle and distance effects. The method can also significantly reduce the intensity variations caused by these effects on homogeneous surfaces.

Rodríguez-Caballero et al. (2016), state that filtering TLS data from unwanted objects like vegetation and artificial structures is necessary to generate a digital terrain map (DTM). Older filtering methods, even if successful in applied to airborne laser scanning (ALS), heavily smooth the terrain surface and do not retain their real morphology sufficiently for TLS data. The authors introduce a novel technique for filtering TLS data. This new method is based on the geometric and radiometric properties of the scanned surfaces. Two case study areas of differing vegetation type and density were used to validate this method. The results show that the DTM accuracy improved by ~30% under dense canopy plants and over ~40% on the open spaces between plants., whereas other methodologies greatly underestimated the real surface heights. This resulted in a more accurate representation of the soil surface and micro-topography than up-to-date techniques, eventually having strong implications in hydrological and geomorphological studies.

The articles in this section display the continuous development of new TLS technology and refinement of existing ones. It can be seen that the maturity of TLS data collection and validation have been improving across the years. While TLS still has many obstacles to overcome before it can achieve its full potential, even in its current state is a powerful tool for geological studies.

2.2 Geological Applications of Terrestrial Laser Scanning

TLS technique can be applied in an interactive manner, proceeding step by step through the processes involved (Fekete et al., 2010; Xie and Lu, 2017). However, the direct application of the technique does not allow the full realization of the advantages of the approach. Therefore, semi-automatic (Trinks et al., 2005; Riquelme et al., 2014), and fully automatic (Roncella and Forlani, 2005) processing of the cloud data has been the subject of recent studies.

Jahn and Truckenbrodt (2004) present a simple procedure for analyzing the roughness of surface profiles. The procedure is a fractal analysis based on a power law for stochastically self-affine functions. A new parameter other than the fractal dimension is introduced. Root Mean Square (RMS) roughness' fractal equivalent is described by this parameter. This new method was tested in case studies that used milled, turned, lapped, and polished surfaces successfully. The results display the smaller computation effort relative to other fractal evaluations.

Slob et al. (2005) describe the interim results of a study to characterize discontinuous rock masses using 3D laser scanning data. This method can perform accurate, rapid, unbiased, and cheap discontinuity analysis. 3D laser scanning can measure rock faces with restricted access or hazardous environment. This technique allows for an accurate reconstruction of the original rock surface in the form of a 3D interpolated and meshed surface using different interpolation techniques since the density of the point cloud can be high. Through geometric analysis of this 3D mesh and plotting of the facet orientations in a polar plot, it is possible to observe clusters, which represent different rock mass discontinuity sets. Individual discontinuity sets can be outlined automatically, and the mean orientations of these identified sets can be computed with fuzzy k-means clustering algorithms. Further demonstration display the ability to remove the facet outliers, assuming a Fisher's distribution. Finally, the study shows that it is possible to calculate discontinuity spacing as well.

Mah et al. (2011) evaluated the application of 3D laser imaging to measure joint orientation. A field trial was conducted at a road cut with three well expressed joint sets. Joint orientation was evaluated with point cloud data using two methods. First was a commercially available 2.5D method based on a triangular irregular network (TIN). Second was a new 3D pole density contouring method where the orientation of each triangular mesh element in the 3D model is determined. Validated against field measurements, the 2.5D and 3D methods were applied manually, and the resultant average angular differences were 13.31 and 3.81, respectively, indicating that the 3D method is very accurate. When automated, the 2.5D and 3D methods yielded results with average angular differences of 14.41 and 9.91. The effects of

image resolution, triangular mesh element size, and joint face geometry on the performance of the 3D pole density contouring method were assessed. Image resolution had minimal effect on measurement accuracy. Increasing the triangular mesh element size had an adverse effect because holes started to appear in the 3D model.

Garcia-Selles et al. (2011) presented a workflow for the supervised and automated identification and reconstruction of near-planar geological surfaces that have a three-dimensional exposure in the outcrop. The original point cloud is used without modifications, and thus no decimation, smoothing, intermediate triangulation, or gridding is required. The workflow is based on planar regressions carried out for each point in the point cloud, enabling subsequent filtering and classification to be based on orientation, quality of fit, and relative locations of points. A coarse grid pre-processing strategy is implemented to speed up the search for neighboring points, permitting analysis of multi-million point clouds. The identified surfaces are classified according to their orientations and regression quality parameters. These can then be used as foundations for outcrop reconstructions or analyzed further to investigate their characteristics such as geometry, dimensions, intersections, spacing, and morphology.

Gigli and Casagli (2011) developed a Matlab tool called DiAna (DiscontinuityAnalysis) to analyze the 2D and 3D geo-structure of discontinuities on high resolution TLS data. The approach the authors propose can semi-automatically retrieve some relevant rock mass parameters. These include orientation, persistence, spacing/frequency, number of sets, block size, and roughness. All these are accomplished by the analysis of high resolution TLS data.

Bitenc et al. (2016) tested 2D wavelet transform (WT) and non-local mean (NLM), which are denoising methods, to obtain roughness estimations suitable for rock engineering. Both methods were applied in two variants of both methods were applied. Conventional discrete wavelet transform (DWT) and stationary wavelet transform (SWT) for WT. Classic non-local mean (NLM) and probabilistic non-local

mean (PNLM) for NLM. The noise effect and denoising performance were studied in relation to the TLS effective data resolution. A very precise Advanced TOpometric Sensor (ATOS) was used on a 20x30 cm rock joint sample to analyze the acquired reference data. The noisy and denoised surfaces were compared to the original ATOS surface to compute the roughness ratio. The success of all denoising methods are indicated by the roughness ratio. The results also show that SWT oversmooths the surface and the performance of the DWT, NLM, and PNLM vary with the noise level and data resolution. As data resolution decreases, the noise effect becomes less important.

Chunxia et al. (2017) obtained the roughness of plowed and sowed surfaces by using a laser profiler. The precision of fractal dimensions based on the Weierstrass–Mandelbort (W–M) function were evaluated. The authors found the structure spectral and rescaled (R/S) analysis methods unsuitable for calculating the fractal dimension on a soft terrain surface. As a result, an analysis of the fractal dimension, correlation coefficient, and non-scale range for each terrain type were performed with using root mean square, power spectral density, and variate-difference methods. Plowed terrain had large fractal dimension with minor fluctuations and it had complex internal structure. The root mean square method calculated fractal dimension was more accurate for soft terrain surface compared to power spectral density method. In addition, the correlation coefficient of linear regression when using the root mean square method was good and the range of non-scale variation was small.

Gomes et al. (2016) introduces a novel method for the detection and estimation of the orientation of planar structures. This automatic procedure results in the reduction of processing and analysis times. It also increases sampled area by fitting the best plane for every surface. Point clusters are detected by the algorithm, which belong to the same plane on basis of the principal component analysis (PCA) technique. The results show that the algorithm’s detection and orientation of fracture planes are precise when applied to real cases.

Franny (2017) compared traditional orientation measurement using Brunton compass to more modern methods using smartphone applications and TLS to find which is more accurate and suitable for rock slope stability determination. The case study site is chosen is a rock outcrop along Stroubles Road on Price Mountain, in Montgomery County, VA. The Price Mountain structure is a doubly plunging anticline exposed in a window in the Pulaski Thrust Sheet. The rock outcrop consists of a Mississippian sandstone mapped as the Upper Price Formation. The site features a set of bedding planes that dip steeply into the cut slope face, yielding toppling failures. In addition, two distinct sets of joints exist, creating both planar and wedge failures in the cut slope. Discontinuity orientations were measured along 61 meters of rock surface using window mapping. A Brunton compass, a smartphone application, and a laser scan were used for measurement. The different method's resulting measurements were compared with stereonet analysis to find their relative accuracy. Brunton compass and the smartphone application showed strong correlation in their measurements. However, the laser scan data required calibration with field measurements and observations to get results on par with other methods. The author concludes that remote sensing methods using laser scanning, should not be used fully independently from traditional field characterization and input from experienced professionals.

Riquelme et al. (2017) in their study introduce the novel technique, named Structure from Motion (SfM). This new technique is stated to be less expensive than three dimensional laser scanning. Both techniques are examined by comparing their point cloud generation of a rock slope and the orientation extractions from the main discontinuity sets. To accomplish this, a sector selected from a cretaceous sedimentary rock cut slope placed in Alicante (Spain) was analyzed with TLS and photogrammetric point clouds. TLS scanned printed targets were used to extract ground control points with accurate coordinates. Thus, less than 3 mm adjustment error was achieved. The results of the comparison yielded sufficient correlation when surface was orthogonal to the line of sight. On the other hand, inaccuracies were observed with SfM dataset on sub-horizontal and oblique surfaces. Finally, a

geometrical analysis was performed by means of Discontinuity Set Extractor (DSE) software. Three discontinuity sets were extracted from both point clouds with two from TLS and one from SfM dataset.

Ting et al. (2017) proposed an unbiased and basic fracture identification method that utilizes 3D surface models generated from TLS data. This method can find surface density which in turn is a major additional data for fracture related research. A case study is done using an outcrop from the Shizigou anticline in the Qaidam Basin (NW China). The method was validated, and its optimal parameters were found by comparing with reference field data and high resolution photographs. The results show that with suitable parameters, the proposed method can identify most structural fractures quickly, providing a solution of extracting structural fractures from virtual outcrops based on TLS data.

Telling et al. (2017) wrote a full review article regarding the application of advanced remote sensing technologies, including TLS. They pointed out that TLS data based products are commonly used tools in Earth sciences. These include Triangulated Irregular Networks (TIN) and Digital Surface Models (DSM), which are used to measure various geological structures and processes which are explained in detail. The review is concluded with a discussion of developments in TLS equipment and their impact on the future of Earth sciences. Articles of interest, which are based on structural geology and mass waste (rockfalls and landslides) are summarized in Tables 2.1. and 2.2.

Table 2.1 Reviewed publications applying TLS to structural geology studies, Telling et al. (2017).

Feng et al. (2001)	Example of initial laser based structural surveys
Slob et al. (2002)	Early use of TLS for discontinuity identification utilizing 3D Delaunay triangulation surfaces
Schulz et al. (2005)	Geomechanical processes and displacements with early scan procedures
Rahman et al. (2006)	Surface roughness of discontinuities and methods
Kokkalas et al. (2007)	3D TIN based virtual outcrops for fault structure and process analysis
Sagy et al. (2007)	Fault roughness and geometries via spectral characteristics of TLS surveys
Sturzenegger et al. (2007b)	Limitations and biases when using TLS in structural surveys
Rotonda et al. (2007)	Plane orientations, early methodology and viability testing
Oldow and Singleton (2008)	Reconstruction of displacements and DEM use for paleoseismic survey
Olariu et al. (2008)	Automatic fracture identification and property extraction
Sturzenegger and Stead (2009a, 2009b)	Review of TLS pertaining to discontinuity characterizations
Candela et al. (2009)	Expansive study of fault topography and roughness
Sagy and Brodsky (2009), Brodsky et al. (2011), Candela et al. (2011), Bistacchi et al. (2011)	TLS methods and analysis for fault roughness, geometry, slip, and fault evolution to smooth surfaces
Lato et al. (2009)	Proper application, methodology, and error analysis for TLS structural survey
Wilson et al. (2009)	Modeling fault surfaces and throw for mechanical, stratigraphic, and displacement evaluation
Jones et al. (2009), Gold et al. (2012), Wiatr et al. (2013)	Workflows to identify fault kinematics, geometry, and slip vectors
Pollyea and Fairley (2011, 2012), Mah et al. (2013)	Roughness measurement methodology and validations
Sturzenegger et al. (2011)	Discontinuity mapping in structural surveys
Candela and Renard (2012)	Methods and geometric nature of faults from the scaling of surface roughness
Haddad et al. (2012)	TLS for identification of paleoseismic structures and geomorphic features
Seers and Hodgetts (2013, 2016)	TLS and photo derived TIN models to identify fracture networks and build 3D trace maps
Wiatr et al. (2015)	High resolution elevation and backscatter models for fault surface properties

Table 2.2 Reviewed publications applying TLS to Mass Wasting studies. S indicates a single scan study and T indicates a temporal scan study, Telling et al. (2017).

Landscape and rockfall applications	
Rowlands et al. (2003)	(S) Early validation of TLS for mass wasting analyses
Kemeny and Turner (2008)	Methodology and specific slope mapping TLS application
Prokop and Panholzer (2009)	(T) Techniques, error and precision analysis for landslide survey
Jaboyedoff et al. (2009a)	Compilation of single and temporal mass wasting surveys
Jaboyedoff et al. (2010)	Complete review of LiDAR use for landslides
Abellán et al. (2014)	Review of TLS use for rock slope instabilities
Landslide applications	
Collins et al. (2007)	(T) Topographic surface modeling and volume change analyses
Sturzenegger et al. (2007a)	(S) TLS and ALS combo for landslide structure and morphology
Teza et al. (2007, 2008a, 2008b)	(T) Landslide kinematics, strain, and displacement methods and analysis
Priest et al. (2008), Olsen et al. (2012a)	(T) Movement and erosion from change in Johnson Creek Landslide
Travelletti et al. (2008)	(T) Change detection methods and mudslide kinematics
Dunning et al. (2009)	(S) Application of TLS in hazardous areas
Baldo et al. (2009)	(T) Multi-instrument monitoring of landslides
Jaboyedoff et al. (2009b)	(T) Slope and flow safety factors of earth flows with TLS, ALS, and GPS
Kasperski et al. (2010)	(T) 2D DEM differencing and surface change
Schürch et al. (2011)	(T) Quantification of scan error, uncertainties, and ambiguities
Oppikofer et al. (2012a)	(T) Landslide survey methodology
Bremer and Sass (2012)	(T) TLS and ALS differencing for debris flow analyses
Aryal et al. (2012, 2015)	(T) 2D and 3D displacement fields with subsurface analyses
Conner and Olsen (2014); Olsen (2013)	(T) Natural object change detection algorithm for displacement fields
Kuhn and Prüfer (2014)	(T) Landslide geometry and erosion form surface model differencing
Blasone et al. (2014)	(T) Quality assessment, DEMs of difference, debris flow morphology

Table 2.2. Continued. Reviewed publications applying TLS to Mass Wasting studies. S indicates a single scan study and T indicates a temporal scan study. Telling et al. (2017).

Rockfall applications	
Janeras et al. (2004), Abellán et al. (2006)	(S) Early TLS and DEM applications to rockface structures and rockfall hazards
Jaboyedoff et al. (2007)	(S) Software and analysis tools
Rosser et al. (2007), Abellán et al. (2010, 2011)	(T) Monitoring, assessment, and prediction via spatial and temporal pattern analyses and methods
Jaboyedoff et al. (2008), Pedrazzini et al. (2010)	(S) Rockface structure assessment for rockfall hazards
Abellán et al. (2009); Heckmann et al. (2012); Rabatel et al. (2008)	(T) Error assessments of rockfall surveys
Oppikofer et al. (2008, 2009)	(T) Modeling rockfall volumes, displacements, slope movements, and structures for hazard analysis
Alba et al. (2011)	(T) Near infrared vegetation filtering for better rockface characterizations
Oppikofer et al. (2012b), Corsini et al. (2013)	(T) High resolution DEM mapping of rockslides and hazard assessment
Zimmer et al. (2012)	(S) Multi-instrument, comprehensive rockfall survey
Brideau et al. (2012)	(S) Rockfall risk survey and methodology with TLS and photo
Tonini and Abellan (2014)	(T) Cluster analyses and methods for rockfalls
Teza et al. (2014)	(S) TLS and thermal imagery for monitoring optimization
Carrea et al. (2015)	(T) Semi-automatic methodology for rockfall detection and volume computation
Olsen et al. (2015)	(T) Methods and evaluations of approaches to identify, measure, and detect change from rockfalls
Kromer et al. (2015)	(T) Techniques and errors of rockfall hazard management project
Strunden et al. (2015)	(T) Large, high temporal resolution rockfall survey and prediction

2.3 Joint Roughness Coefficient Estimation

One of the significant outcomes in the determination of joint properties by the TLS approach is the estimation of the shear strength of rock joints to be used for the determination of the mechanical properties of rock masses. The shear strength of rock joints depends strongly on the rock joint roughness.

The empirical equation proposed by Barton and Choubey (1977) has been the most commonly used formula for the estimation of peak shear strength of a joint. It contains the peak shear strength of the rock joint, the normal stress, the strength of the joint wall, and the basic friction angle. In this equation, it is possible to obtain all the parameters except JRC by standard tests. The JRC of a particular rock joint profile, however, needs to be estimated. The estimation is done traditionally by visually comparing the sample profile with the 10 standard profiles with JRC values ranging from 0 to 20.

This approach was also adopted by and Muralha et al. (2014) to the International Society for Rock Mechanics (ISRM) (1987) descriptions, and has been widely used in practice since its publication.

To analyze the reliability of this traditional visual assessment method, Beer et al. (2002) performed a survey based on three granite block profiles with 125, 124, and 122 answers from people with different levels of experience, using an internet-based survey system. The results indicated that a wide range of JRC estimation values could be obtained even in the case of experienced survey subjects.

Graselli and Egger (2003) randomly extracted three different profiles from different samples in the shear direction. JRC was estimated both with visual comparison and with back analysis from shear test results. The results clearly confirmed that it was not easy to uniquely estimate the JRC value using the visual assessment method.

Alameda-Hernandez et al. (2014) performed a similar visual estimation survey with 90 trained subjects undertaking the survey test. The results of the survey clearly showed systematic inaccuracies in the visual evaluation procedure. As a result, the conclusion

that the visual assessment procedure of JRC is strongly subjective and thus not suitable for a reliable estimation has been widely stated in the literature. It is clear that the visual evaluation for the estimation of JRC is not suitable for use in a fully automated procedure either.

With the recognition of the subjectivity of the traditional assessment method, researchers turned their attention to the development of objective methods. A considerable number of publications for the determination of the JRC, mainly using statistical parameters and fractal dimension of the joint profiles have thus appeared in the literature.

Tse and Cruden (1979) investigated the correlations between JRC and surface parameters by using back-calculated JRC values of Barton and Choubey's 10 reference surface profiles. As surface parameters, they adopted the RMS of the first derivative of the profile (Z_2) suggested by Myers (1962), and the structure-function (SF), which was related to the autocorrelation function proposed by Sayles and Thomas (1977). They concluded that the joint roughness coefficient of a rock surface could be well predicted by the Z_2 and SF.

Yu and Vayssade (1991), while supporting the proposition that a strong correlation exists between JRC and Z_2 or SF, stressed the fact that these parameters were sensitive to sampling interval and thus were insufficient in practice.

Yang et al. (2001) showed that due to the self- affinity transformation law, scaling of the reference JRC profiles did not influence the final JRC values.

Tatone and Graselli (2010) modified the equations relating JRC to Z_2 given by Tse and Cruden (1979) for different sampling intervals.

Zhang et al. (2014) modified Z_2 and its application by including dilation angle, which could be attributed as positive or negative, in order to account for the directional dependencies.

In their literature survey, Li and Zhang (2015) listed 47 empirical equations for the estimation of JRC of a joint profile using Z_2, SF, and other statistical parameters as the variables. They noted that previously published equations may misestimate of the JRC

of a profile and stressed once more that special caution should be paid when using these equations.

Recently Wang et al (2019) proposed still another roughness parameter PZ including the influence of the amplitude height of the rock joint profile to the modified Z_2 proposed by Zhang et al. (2014). The calculation of PZ requires a rigorous and difficult analysis procedure to estimate JRC. While this study presents the most detailed treatment of the problem to this day, the calculation of PZ requires a rigorous and difficult analysis procedure to estimate JRC.

Another approach for the estimation of JRC values has been the use of fractal dimension (Carr and Benzer, 1991). Coastlines best represent deterministic fractals and fractal (Hausdorff-Besicovitch) dimensions. They suggest a divider method to calculate fractal dimensions for these features. A divider measurement method yields a fractal dimension, which is a measure of the complexity of the shape. Noise models are used to develop another type of fractals, named stochastic fractals. Spectral and variogram methods are used to estimate fractal dimensions for stochastic fractals. It is stated that when estimating the fractal dimension, the objective of the analysis must be consistent with the method chosen for fractal dimension calculation. Spectral and variogram methods yield fractal dimensions, which indicate the similarity of the feature under study to noise (e.g., Brownian noise).

Brown and Scholz (1985), and Develi and Babadağlı, (1998) noted that fracture surfaces fitted well to self-affine fractal behavior. Thus, surfaces have been evaluated in terms of their fractal dimension through methods that are applicable to self-affine fractal objects.

For the determination of the fractal dimension of a rock joint profile compass-walking (also known as divider) method: Maerz et al. (1990), Bae et al. (2011), Xu et al. (2012), or box-counting method Cheng (1997) have been commonly used. It is possible, however, to obtain different values of fractal dimension (D) using the two methods for the same profile as indicated by Li and Huang (2015).

On the other hand, Outer et al. (1995) investigated the characterization of the roughness of a discontinuity in terms of a fractal and/or fractal dimension and concluded, from the relations between the JRC and fractal dimension, that either the roughness profiles were not fractals or the divider method was not suitable for determining the fractal dimension.

Nevertheless, a large number of studies have been conducted on the relation between fractal dimension and JRC, among which are Lee et al. (1990), Huang et al. (1992), Xu et al. (2012), Jang et al. (2014). In these studies, the fractal dimension has been found to correlate reasonably well with JRC values and numerous empirical equations were proposed for estimating JRC using fractal dimension. 19 such empirical equations were collected and examined critically by Li and Huang (2015). They noted that each equation reflected the method used by the authors to determine the value of D, the differences between the profiles assessed, and the data collection and processing procedures followed. They further noted that the empirical equations showed inconsistencies, sizable variations from one another, and most of them appeared to be correct only over specific ranges of D and JRC.

In an early assessment of these methodologies for joint roughness coefficient determination, Hsiung et al. (1993) concluded that none of the methods might be capable of providing a reasonable JRC value. This conclusion seems to be still valid. Whether one selects the statistical parameter Z_2 and its variants or the fractal dimension D for the estimation of JRC, it is difficult to choose one of the many equations proposed for use in the application in mind. Each equation seems to give good results for the samples analyzed by the authors. However, tests of proposed equations for the accuracy of JRC estimation for samples tested/analyzed by other researchers are not easily found in the literature. As a result of this critical examination of the major methods related to the determination of JRC of rock masses, one may conclude that there exists no universally accepted method for the accurate and reliable estimation of the value of JRC of a sample surface profile yet, in spite of the large number of research studies carried out since the publication of the major reference study by Barton and Choubey almost half a century ago.

CHAPTER 3

DISCONTINUITY PROPERTIES

According to ISRM (1978), “any separation in a rock mass having zero or low tensile strength is defined as discontinuity”. This general term includes most types of joints, weak bedding planes, weak schistosity planes, weakness zones, and faults. Rock masses are different from other engineering materials due to discontinuities. Thus, a detailed characterization of discontinuities is essential in determining the engineering properties of rock masses. As Palmström (2002) noted: “The engineering properties of a rock mass often depend far more on the system of geological defects within the rock mass than on the strength of the rock itself. Thus, from an engineering point of view, a knowledge of the type and frequency of the joints and fissures are often more important than the types of rock involved. The observations and characterization of the joints should therefore be done carefully.”

3.1 Types of Discontinuities

Discontinuities and their formations are explained in textbooks in particular by Price (1966), Hills (1972), Blyth and de Freitas (1974), Hobbs (1976), and Priest (1993). These sources provide valuable discussions on this subject in terms of engineering. The following subchapters list the important types of discontinuities and their properties in engineering applications.

3.1.1 Faults

Faults are a type of discontinuity identified by the presence of past shear displacement. In faults, the relative displacement of the two sides can be observed. Faults are classified according to the sense of the relative displacement. Faults can be prevalent throughout large areas or they may be contained locally usually in grades or groups. Similarly, fault thickness varies between meters and millimeters depending on whether they are regional or local faults. Materials like fault gouge (clay), fault breccia (recemented), rock flour or angular fragments may be present within the fault plane. Due to the relative displacement, the walls are usually slickensided and sometimes covered with minerals such as graphite and chlorite. Faults are zones of low shear strength where rock layers may slip and the ground bordering the fault can be affected by the displacement of the rock mass.

3.1.2 Bedding Planes

Sedimentary rocks are divided into layers or beds by bedding planes. These are break-offs in the rock mass deposits and thus usually have persistent features. Beddings can be discordant or cross depending on how rapidly the sediment is deposited due to water or wind currents. When bedding planes include parting material of varying size, the shear resistance between bedding planes will be determined by friction alone even if cohesion is increased by lithification. The orientation of the parting material will determine the planes of weakness in the bedding planes.

3.1.3 Joints

Among all discontinuities, joints are the most commonplace and important discontinuity types when geotechnical applications are concerned. Joints are open, filled, or healed breaks in rock mass that do not involve relative displacement. Joints parallel to each other form a joint set and joint sets in a region are part of a joint system. Joints can be named after layers or other discontinuities they form parallel to such as cleavage joint, bedding joint, or foliation joint. Regular joints often end when they encounter other layers, however, master joints can cross multiple layers without being terminated.

3.1.4 Cleavage

Rocks splitting into thin layers due to metamorphism is called cleavage. In general, rock cleavage is divided into flow cleavage and fracture cleavage depending on its origin. Fracture cleavage formed compression and cementation, while flow cleavage is formed by recrystallization due to pressure and high temperature. Cleavage is generally visible in some metamorphic rocks (schists, slates, phyllites, etc.) and they mostly possess tensile strength that cannot be ignored. Thus, they are not part of the discontinuity system. However, cleavages may create anisotropy that contributes to the strength and deformability of rock masses. This can lead to geological processes like faulting and folding which in turn can create discontinuities that contribute to planes of weakness.

3.2 Description of Discontinuities

The ISRM (1978) publication contains methods for the quantitative description of discontinuities in rock masses. The characteristics of discontinuities are defined by the ten parameters listed below:

1. **Orientation** is related to the attitude of a discontinuity in space. The dip direction (azimuth) and dip angle of the line of steepest declination in the plane of the discontinuity define orientation.
2. **Spacing** gives the perpendicular distance between adjacent discontinuities. In the case of a set of discontinuities, it is the mean or modal spacing of the set.
3. **Persistence** is the observed discontinuity trace length. It gives a rough measure of the extent/penetration length of a discontinuity. Persistence is reduced if the discontinuity is terminated in solid rock or against other discontinuities.
4. **Roughness** is the term describing the surface roughness and waviness of the rock mass. It is relative to the mean plane of a discontinuity. Both roughness and waviness are related to shear strength. The local dip may be affected by large-scale waviness.
5. **Wall Strength** refers to the effective compressive strength of the adjacent rock walls of a discontinuity. Weathering or alteration of the walls may result in a wall strength lower than rock block strength. If rock walls are in contact, its contribution to shear strength will be significant.
6. **Aperture** is the perpendicular distance between adjacent rock walls of a discontinuity. The space between layers is filled with air or water.
7. **Filling** is the material that is in between the adjacent rock walls of a discontinuity. It is generally weaker than the rock walls. Common filling materials are sand, silt, clay, breccia, gouge, mylonite. Thin mineral coatings and healed discontinuities like quartz and calcite veins may also be considered as filling materials.
8. **Seepage** is the water flowing or visible moisture in discontinuities or in the entire rock mass.
9. **Number of Sets** refers to the number of discontinuity sets of the intersecting discontinuity systems.
10. **Block Size** is the rock block dimensions of the blocks formed by intersecting discontinuity sets. Block size depends on the spacing of the individual sets.

The geometrical properties of discontinuities included in the scope of this study; orientation, spacing, persistence, block size, and roughness are detailed in the following sections.

3.3 Discontinuity Orientation

Orientation is related to the attitude of a discontinuity in space. The elements that define discontinuity orientation are; the dip direction is measured clockwise from true north (azimuth) and dip angle from the horizontal plane in the plane as seen in Figure 3.1.

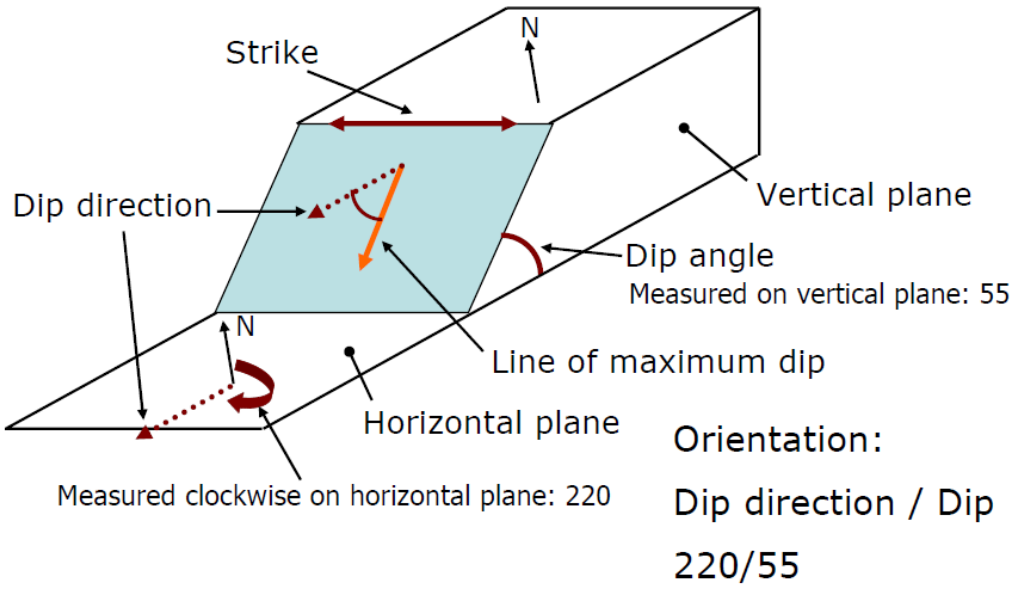

Figure 3.1. Plane orientation and its defining properties, Zhang (2017).

The easiest method of joint orientation measurement is making use of exposed and accessible rock faces. Underground excavations and slope cuts are similarly useful. A geological compass is the simplest way to measure orientation. From the readings dip angle (inclination) and dip direction (bearing) can be measured with a Brunton compass displayed in Figure 3.2.

Inaccessible outcrops can also be made useful in finding the orientation of discontinuities by making use of surveying methods applied on daylighted jointed planes. Measurements taken from exposed surfaces will give the orientation of daylighted lines and these can be used to find the orientations of the same joint plane's daylighted traces.

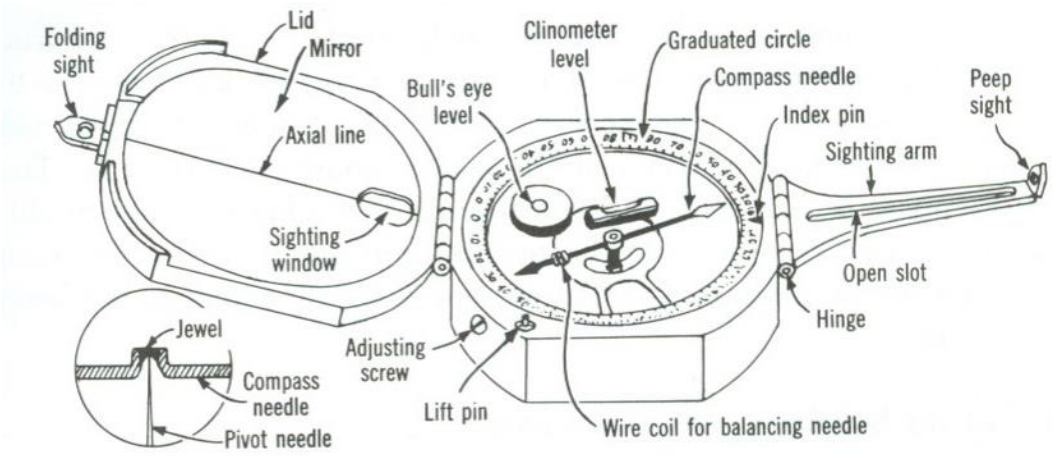

Figure 3.2. The standard Brunton compass and its most essential parts. (University at Buffalo, 2020)

If two trace line orientations represented as α_1, β_1, and α_2, β_2 (plunge and trend) are known from 3D geometry, as shown in Figure 3.3., then dip angle α and dip direction β can be found in the equation,

$$\frac{\tan \alpha_2}{\tan \alpha} = \cos(|\beta - \beta_1|) \tag{3.1}$$

and

$$\frac{\tan \alpha_2}{\tan \alpha} = \cos(|\beta - \beta_2|) \tag{3.2}$$

when the two equations above are combined the result is,

$$\frac{\tan \alpha_1}{\tan \alpha_2} = \frac{\cos(|\beta - \beta_1|)}{\cos(|\beta - \beta_2|)} \tag{3.3}$$

The dip direction of the plane β can be found using this equation, provided α_1, β_1, and α_2, β_2, are known. A substitute β can be used in the earlier equations to find dip angle α.

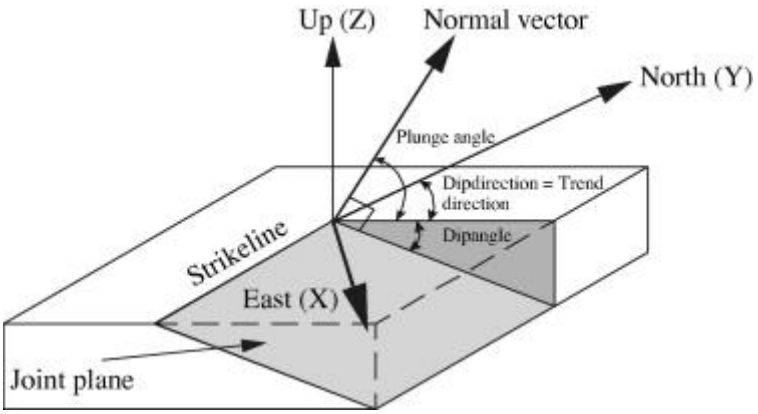

Figure 3.3. The relation between dip direction, trend direction, dip angle, and plunge angle. (Ge et. al., 2014)

The apparent dip in the dip angle is displayed by the day-lighted joint plane trace, which is always less than the true dip. This is due to the true dip being set as the maximum dip angle of the plane.

The strike of the discontinuity may also be measured instead of the dip direction. Dip direction (three digits) and dip angle (two digits) are presented in the form $035^o/75^o$ and $290^o/30^o$. The orientation of discontinuities relative to an engineering structure largely controls the possibility of unstable conditions or excessive deformations developing. The importance of orientation increases when other conditions for deformation are present, such as low shear strength and a sufficient number of discontinuities for slip to occur. The mutual orientation of discontinuities will determine the shape of the individual blocks, beds, or mosaics comprising the rock mass.

The orientation of discontinuities is measured from core samples or from outcrops using one or two-dimensional scanlines. It is usual to plot the measured orientation data on stereonet. Such a plot on a polar stereonet of the poles of 351 individual discontinuities was presented by Hoek and Brown (1980). The orientations of the discontinuities were measured at a particular field site. In Figure 3.3. different symbols have been used for three different types of discontinuities, i.e., bedding planes, joints, and a fault. The dip direction of the fault is 307^o and its dip angle is 56^o. The preferred orientations of the various discontinuity sets are indicated by the contours of pole concentrations for the bedding planes and joints. The contours of pole concentrations obtained from Figure 3.4. are shown in Figure 3.5. The orientations of the center of the two prominent joint sets are obtained as $347^o/22^o$ and $352^o/83^o$. For the bedding planes, the orientation is given as $232^o/81^o$.

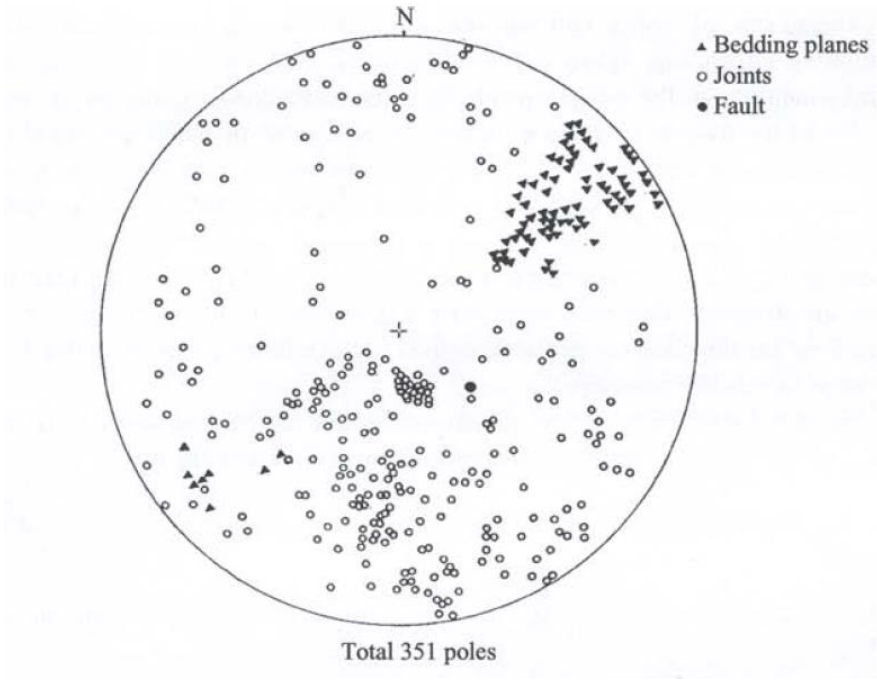

Figure 3.4. The plot of poles of 351 discontinuities, Hoek and Brown (1980a).

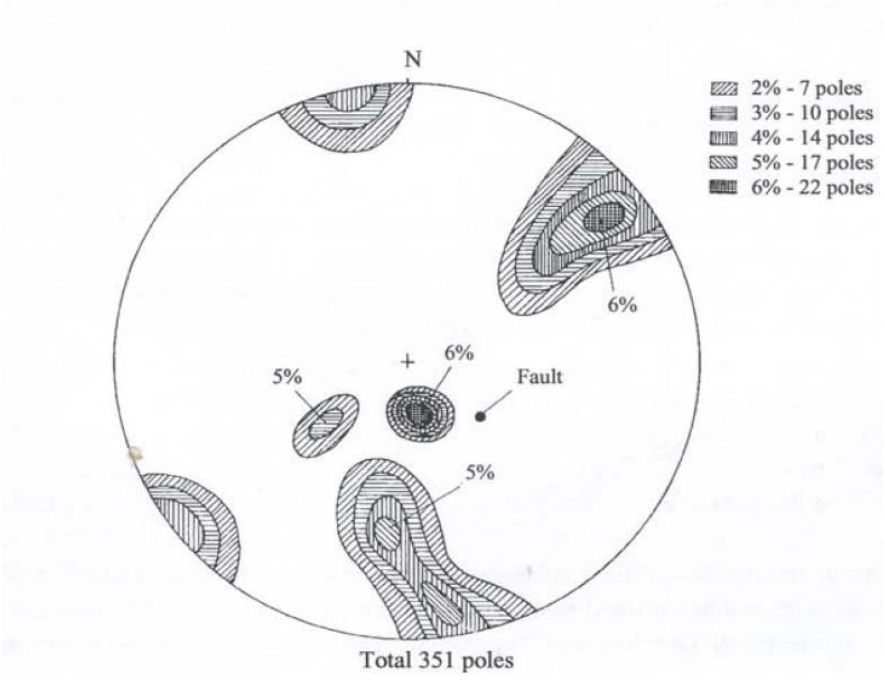

Figure 3.5. Contours of pole concentrations for the data plotted in Fig. 3.3., Hoek and Brown (1980a).

3.4 Discontinuity Spacing

Discontinuity spacing is defined as the distance between adjacent discontinuities in a scanline. If a particular discontinuity set is considered, the spacing is called the set spacing. The spacing is named normal set spacing in the case of a scanline parallel to the mean normal to the discontinuity set, Priest (1993). The terminology for the description of discontinuity spacing magnitude used by ISRM (1978c) is given in Table 3.1.

Table 3.1 Classification of discontinuity spacing, ISRM (1978c).

Description	*Joint Spacing (m)*
Extremely close Spacing	< 0.02
Very close spacing	0.02 - 0.06
Close spacing	0.06 - 0.2
Moderate spacing	0.2 - 0.6
Wide spacing	0.6 - 2
Very wide spacing	2 - 6
Extremely wide spacing	> 6

The spacing of a joint set is often defined by the average spacing of individual joints within the set under ideal conditions. If the exposed rock face does not reveal a sufficient amount of information, then apparent spacing is used to represent the joint set. The differences between individual, apparent, and true spacing are illustrated in Figure 3.6. Such measurements on the exposed surface give apparent joint spacing, which is directional. Thus, results will depend on the scanline direction. The average spacing is used when assessing the degree of rock fracturing. However, it should be noted that average joint spacing can change depending on what is revealed in the rock exposure as shown in Figure 3.6.

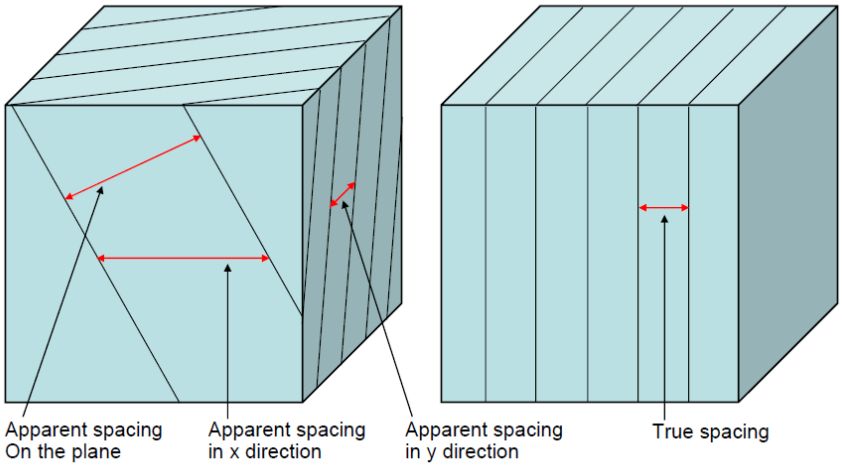

Figure 3.6. Joint spacing, apparent spacing, and true spacing, Zhang (2017).

3.5 Discontinuity Persistence

Persistence is the observed discontinuity trace length within a plane. It gives a rough measure of the extent/penetration length of a discontinuity. It can be visually quantified by discontinuity trace lengths on outcrops if only a rough measure is sufficient. To classify persistence, the modal trace lengths of each set of discontinuities measured on exposed rock faces are given by ISRM (1978c) in Table 3.2.

Table 3.2 Classification of discontinuity persistence, ISRM (1978c).

Description	Modal trace length (m)
Very low persistence	<1
Low persistence	1-3
Medium persistence	3-10
High persistence	10-20
Very high persistence	>20

Discontinuity persistence is among the most significant of the rock mass parameters, but it is challenging to determine. The persistence of discontinuities of different sets is usually different as well. Smaller sets are terminated in solid rock or against major discontinuities. The sets of discontinuities can be classified as persistent, sub-persistent, and non-persistent. The persistence of various sets of discontinuities is illustrated in Figure 3.7. by a set of sketches and block diagrams. It is obvious that the persistence of discontinuities will be influential in the development of shear strength in the plane of the discontinuity.

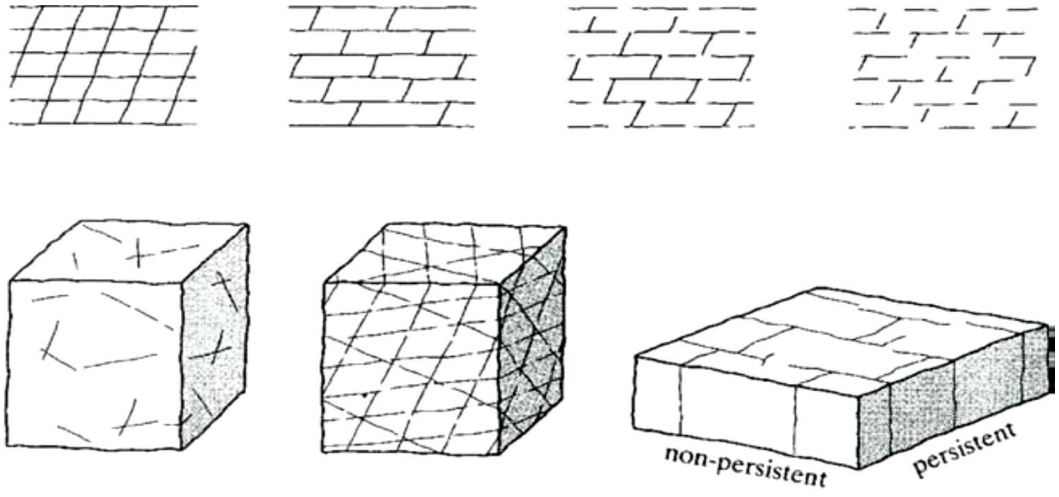

Figure 3.7. Sketches and block diagrams displaying persistence of various sets of discontinuities, ISRM (1978c).

Discontinuity persistence is usually defined using persistence ratio (PR), which is often found using the following equation:

$$PR = \lim_{A_S \to \infty} \frac{\sum_i a_{Si}}{A_S} \tag{3.4}$$

in which S is a region on the discontinuity plane with area A_S; and a_{Si} is the area of the i^{th} discontinuity in S, Figure 3.8. (Einstein et al., 1983). The summation in the equation above is over all discontinuities in S. An alternative expression of PR as limit length ratio along a line on a plane is given as:

$$PR = \lim_{L_S \to \infty} \frac{\sum_i l_{Si}}{L_S} \tag{3.5}$$

in which L_S is the length of a straight line segment S and l_{Si} is the length of the i^{th} discontinuity segment in S, Figure 3.9. (Zhang, 2017). The following equation is used to estimate PR for a finite sampling length L_S as illustrated in Figure 3.9.

$$PR = \frac{\sum DL}{\sum DL + \sum RBL} \tag{3.6}$$

where ΣDL is the sum of the length of all discontinuities; and ΣRBL is the sum of the length of all rock bridges (Zhang, 2017).

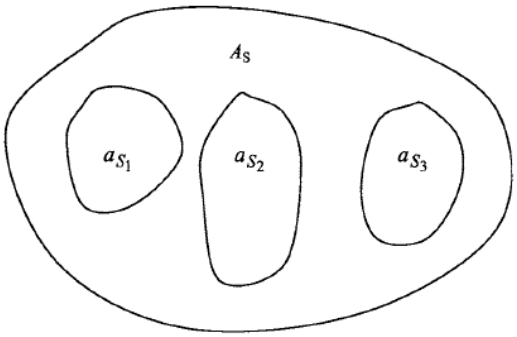

Figure 3.8. Definition of PR as area ratio, Einstein et al. (1983).

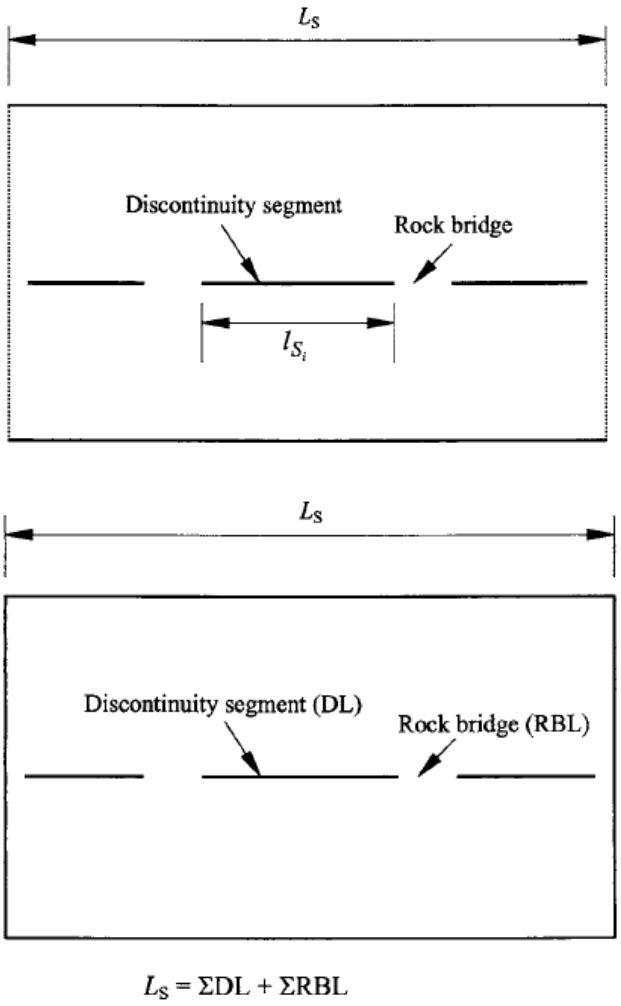

Figure 3.9. Definition of PR as length ratio and estimation of PR for a finite sampling length, Zhang (2017).

3.6 Discontinuity Block Size

Another significant parameter for the description of discontinuity intensity and rock mass behavior is the block size, which is the rock block dimensions of the blocks formed by intersecting discontinuity sets. Discontinuity sets' number, spacing, and persistence determine block size, while number and orientation determine block shape. Generally, block shapes cannot be clearly described due to their irregular nature. A clear definition of block shape can be given in regular jointings like in sedimentary rocks. Dearman (1991) displays block shape examples in Figure 3.10.

Where individual blocks can be observed on a surface, their volumes can be directly measured from relevant dimensions by selecting several representative blocks and measuring their average dimensions. Where three discontinuity sets occur, the block volume can be calculated as:

$$V_b = \frac{s_1 s_2 s_3}{\sin\gamma_1 \sin\gamma_2 \sin\gamma_3} \tag{3.7}$$

where s_1, s_2, s_3 are the normal set spacings respectively of the three discontinuity sets; and γ_1, γ_2, γ_3 are the angles between the discontinuity sets. The block volume is calculated with the equation below when the discontinuity sets intersect at right angles:

$$V_b = s_1 s_2 s_3 \tag{3.8}$$

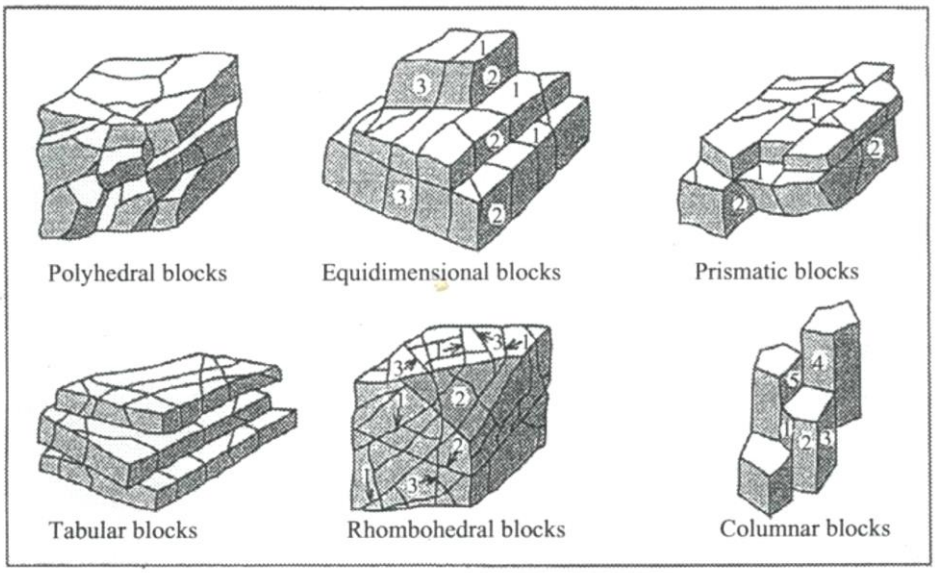

Figure 3.10. Examples of block shapes, Dearman (1991).

The volumetric discontinuity frequency λ_v can also be used to describe the block size as shown in Table 3.3. To describe both the block size and shape, the adjectives listed in Table 3.4. can be used to describe block shape and size.

Table 3.3 Terms for describing block size based on volumetric discontinuity frequency λ_v, ISRM (1978c).

Volumetric frequency λ_v (discontinuity/m^3)	Description
<1	Very large blocks
1-3	Large blocks
3-10	Medium sized blocks
10-30	Small blocks
>30	Very small block

Table 3.4 Adjectives for describing block size and shape, ISRM (1978c).

Adjective	Description
Massive	Few discontinuities or very wide spacing
Blocky	Approximately equidimensional
Tabular	One dimension considerably smaller than the other two
Columnar	One dimension considerably larger than the other two
Irregular	Wide variations of block size and dimensions
Crushed	Heavily jointed to “sugar cube”

3.7 Discontinuity Roughness

The natural waviness and unevenness of a surface relative to its mean plane are measured by roughness. The discontinuity roughness affects the shear strength of the rock mass. The presence of prior shear displacement, filling, or aperture decreases the significance of roughness.

Small scale irregularities and large scale undulations can be differentiated if discontinuities are being observed from drill cores or rock exposures as seen in Figure 3.11. It is possible to arbitrarily quantify these types of roughness or use descriptive terms as it is often done in the early phases of mapping as presented in Table 3.5. Alternatively, Figure 3.12. provides a roughness quantification on multiple scales, where the roughness is defined with both small and large scale descriptions.

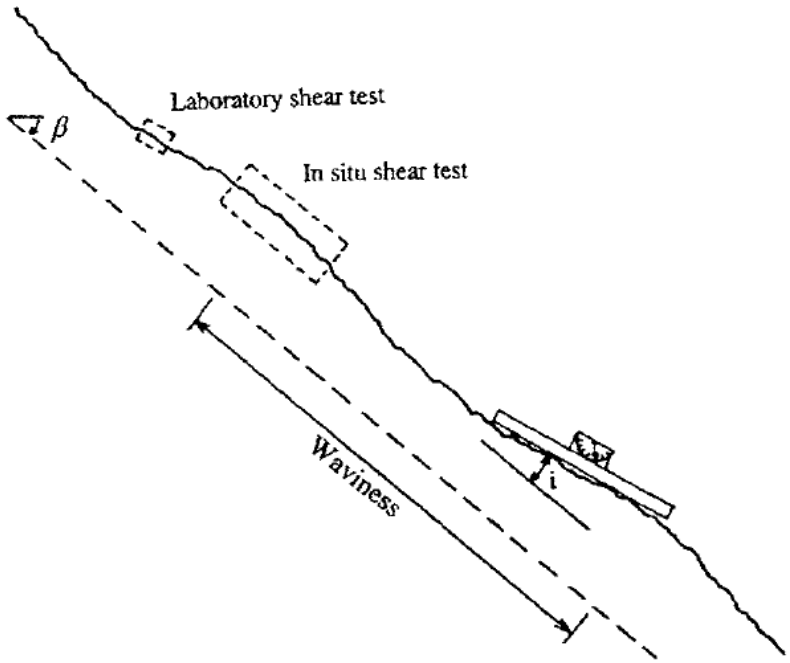

Figure 3.11. Different scales of discontinuity roughness are sampled by different scales of tests. The waviness can be characterized by the angle i, ISRM (1978c).

Table 3.5 Classification of discontinuity roughness, ISRM (1978c).

Class	Description
I	Rough or irregular, stepped
II	Smooth, stepped
III	Slickensided, stepped
IV	Rough or irregular, undulating
V	Smooth, undulating
VI	Slickensided, undulating
VII	Rough or irregular, planar
VIII	Smooth, planar
IX	Slickensided, planar

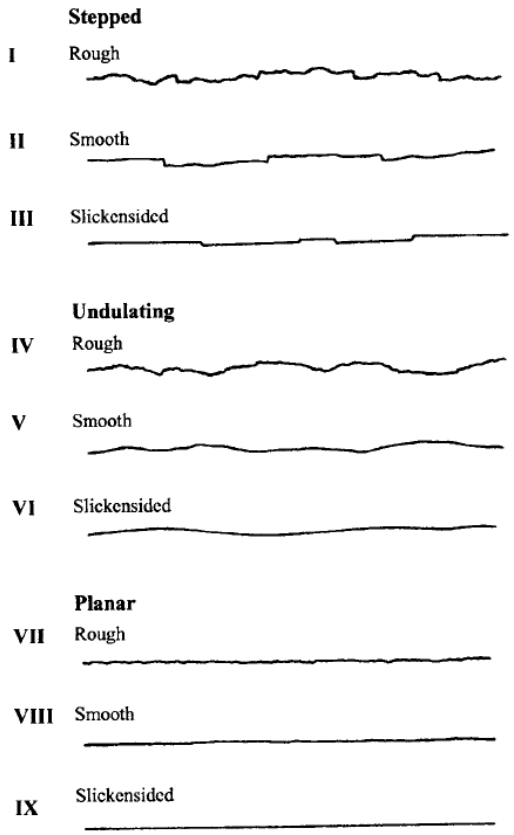

Figure 3.12. Typical roughness profiles and suggested nomenclature. The length of each profile is in the range of 1 to 10 meters. The vertical and horizontal scales are equal, ISRM (1978c).

Joint Roughness Coefficient (JRC) is another generally accepted classification for roughness and was proposed by Barton and Choubey (1977). JRC varies between smooth flat and very rough surface, which are assigned the values of 0 and 20 respectively. The 2D profiles that serve as templates for the proposed JRC are presented in Figure 3.13. JRC is dependent on the geometrical scale of the sample profiles compared with the template profiles, hence the value of JRC becomes less as size increases.

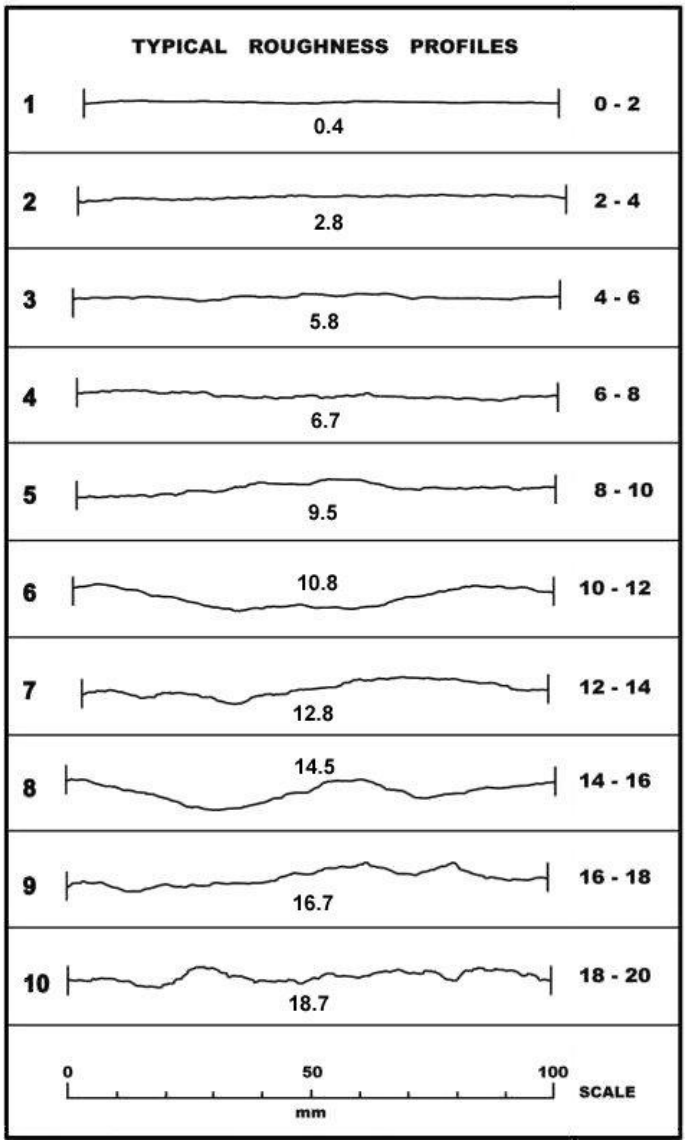

Figure 3.13. Template JRC profiles, Barton and Choubey (1977).

It is important to remember that discontinuity surfaces are actually 3D as displayed in Figure 3.14. The templates given earlier are all based on 2D profiles of discontinuity surfaces. Thus, it is recommended that multiple 2D profiles should be taken from the surface to achieve a more representative JRC estimation.

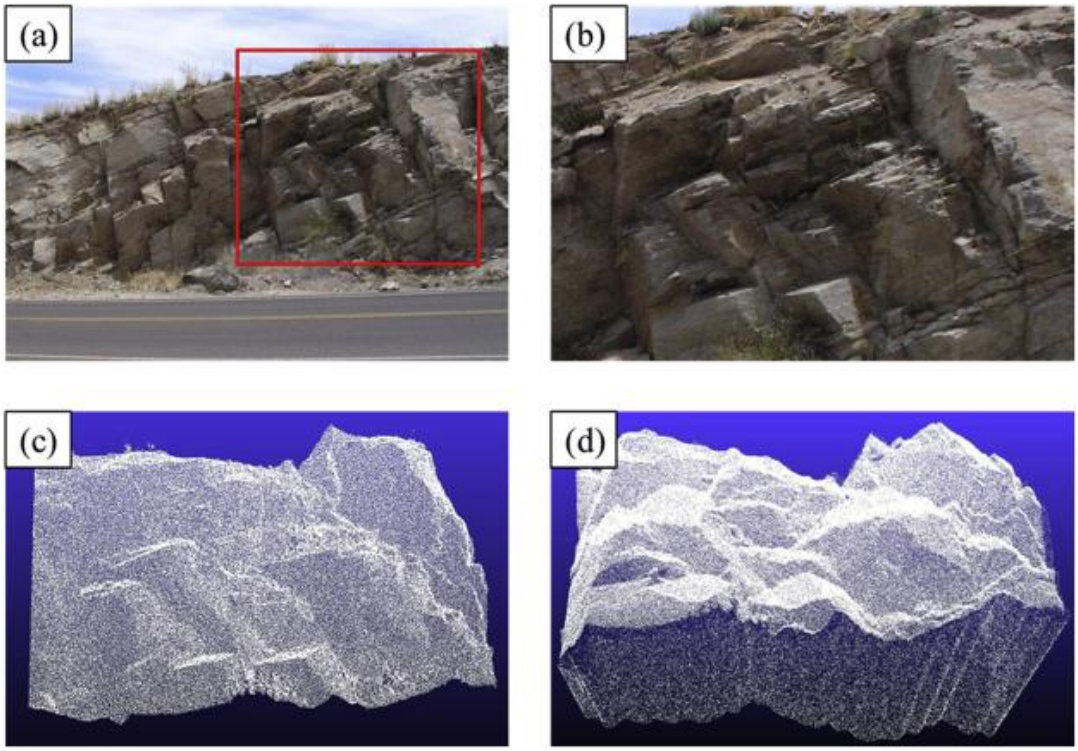

Figure 3.14. Three-dimensional presentation of a discontinuity surface. (Chen et. al., 2017)

3.8 Remaining Discontinuity Properties

The scope of the study is limited to data obtained by using TLS. As a result, some of the properties used to describe a discontinuity cannot be determined using point cloud data. Wall strength, filling, seepage, and aperture require different data from laboratory testing or photographs. Before discussing how the available properties are determined using TLS data, point cloud data will be explained in detail in the following chapter. The determination of surface roughness of discontinuities will be further elaborated in Chapter 7 since it involves a novel method.

CHAPTER 4

POINT CLOUD DATA

A large number of data points on the exterior surface of an object of a defined coordinate system constitute a point cloud. Such points are often defined by X, Y, and Z coordinates in three-dimensional coordinate systems. Point cloud data representing the external surface of an object are usually obtained by using a 3D scanner. A large number of points on the surface of an object are measured with these devices and the output is stored in a point cloud data file. Point clouds produced by 3D scanning process are used in many applications, and in many different areas. These applications vary from the creation of 3D CAD models for manufactured parts for quality inspection, visualization, animation, rendering, to modelling dentures for medical research and development.

In order to utilize the point cloud data, captured via laser scanning, in various applications, certain steps must be followed. In addition, since a Matlab application is designed certain steps will be added to reflect the full extent of the job done. The components of the point cloud data processing are as follows;

- Point Cloud Data Formats
- Data Registration
- Outlier removal

The applications of these steps to experimental point cloud data, as well as the algorithms for implementing each step are presented in the following sections. The relevant Matlab functions for each operation are also presented.

4.1 Point Cloud Data Format

TLS point cloud data may be obtained in different formats depending on the particular source. Thus, it is important to understand the basic structure of the available cloud data format types so that the software to be developed may operate on data with a wide range of possible format types.

Currently, the most common point cloud data formats regarding geology are PLY, Las, and XYZ files. STL format is also mentioned a lot in various sources, however, its main use appears to be in 3-D printing. Matlab has 'readPtCloud' command to read PLY files and 'importdata' command to import text and XYZ files. Additionally, the mat file format utilized by Matlab software is not a dedicated point cloud data format. However, this study uses Matlab extensively and point cloud data can be stored in mat files. Hence, it will be explained in detail as well.

The point cloud data of a rock slope excavated for limestone in El Campello, Spain named '00 Raw data - Site10 Ouray1 – Mesh.ply' by Riquelme et al. (2014) was used in the work in order to test the capabilities of the algorithms to be used in the Matlab program. The point cloud data is displayed in Figure 4.1. The sample has two distinct and visible joint surfaces in its upper half. The lower half has been weathered severely, thus hiding the joint surfaces. A slice from the upper half was taken to experiment with possible ways to detect discontinuity planes of the joints.

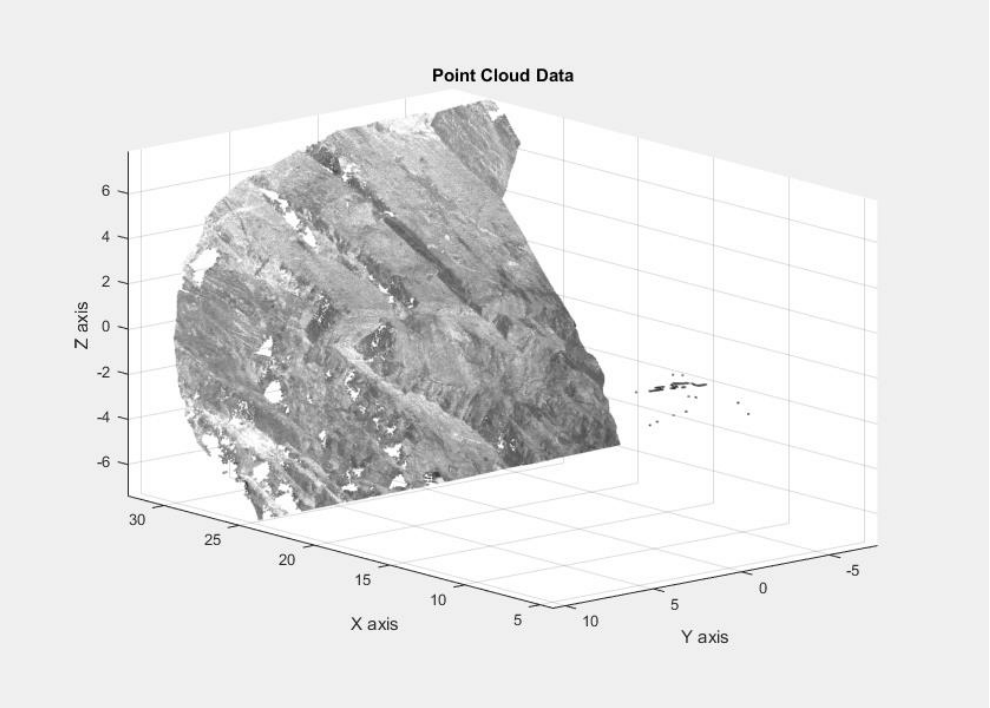

Figure 4.1. Point Cloud data used for Matlab code experiments, Riquelme et al. (2014).

4.1.1 Polygon File Format (PLY)

PLY is a computer file format known as the Polygon File Format or the Stanford Triangle Format. It was principally designed to store three-dimensional data from 3D scanners. There are two versions of the file format, one in ASCII (abbreviated from American Standard Code for Information Interchange, is a character encoding standard), the other in binary (Bourke, 2016).

The PLY format describes an object as a collection of vertices, faces, and other elements, along with properties such as color and normal direction that can be attached to these elements. A typical PLY object definition is simply a list of (x,y,z) triples for vertices and a list of faces that are described by indices into the list of vertices (Bourke, 2016).

A typical PLY file structure is as follows:

Header
Vertex List
Face List
(lists of other elements)

The complete ASCII description for a cube is presented below. (Bourke, 2016)

```
ply
format ascii 1.0          { ascii/binary, format version number }
comment made by Greg Turk  { comments keyword specified, like all lines }
comment this file is a cube
element vertex 8          { define "vertex" element, 8 of them in file }
property float x          { vertex contains float "x" coordinate }
property float y          { y coordinate is also a vertex property }
property float z          { z coordinate, too }
element face 6            { there are 6 "face" elements in the file }
property list uchar int vertex_index { "vertex_indices" is a list of ints }
end_header                { delimits the end of the header }
0 0 0                     { start of vertex list }
0 0 1
0 1 1
0 1 0
1 0 0
1 0 1
1 1 1
1 1 0
4 0 1 2 3                 { start of face list }
4 7 6 5 4
4 0 4 5 1
4 1 5 6 2
4 2 6 7 3
4 3 7 4 0
```

4.1.2 XYZ File Format

ASCII or binary files containing a et of vertices is called an XYZ file. AccuTrans 3D header is an optional choice if no other data is used. Users can enter information into a dialog box that appears when XYZ file is read, provided there is no optional header in use. X, Y, and Z coordinates that form the vertex is represented by a set of three floating point numbers.

A set of three floating-point numbers represents the X, Y, and Z coordinates of a vertex. Only the decimal point only has to be written in an ASCII file should it be necessary. Binary file formats can be Motorola or Intel. Their floating point numbers can be floats (4 bytes) or doubles (8 bytes) (Micromouse Productions, 2016).

The vertices of the mesh are arranged in an M by N array.

- M is the number of columns of data
- N is the number of rows of data. Each row of data must contain M sample points.
- The sample interval (row or column) between any two points is variable.
- Elevations can be either positive or negative.
- The coordinates can be stored using one of the three supported coordinate systems.
- Think of this mesh as a section of the screen removed from a screen window. The screen is bent and twisted as it is molded around some real-world 3D object.
- The vertices can be anywhere in 3D space and the only way of knowing how they relate to one another is by the values assigned to the M and N variables.
- The coordinates can be written to the ASCII file with just a single space between the coordinates or the data can be formatted with user-specified delimiters and any number of line terminators (carriage return or line feed or carriage return and line feed pair).

The data can be written as a polyline mesh to a DXF file after the data has been read by AccuTrans 3D from a file. Finally, the data is converted to a 3D object that can be saved to any supported file format. The data can be stored by row or by column and is not sorted after being read. (Micromouse Productions, 2016).

An array with three rows and four columns, twelve vertices in total, is used in the example shown in Figure 4.2. The row numbers are R1, R2, and R3. The column numbers are C1, C2, C3, and C4. Both the X and Y directions have 10 units of spacing in this array forming a basic rectangular grid, where Z coordinates are set to 0 units. The vertex in the lower left corner is set to X, Y, Z coordinates of 0, 0, 0. The vertex in the top right corner is set to X, Y, Z coordinates of 30, 20, 0. The twelve vertices saved by row or by column using optional header is displayed in Table 4.1. (Micromouse Productions, 2016)

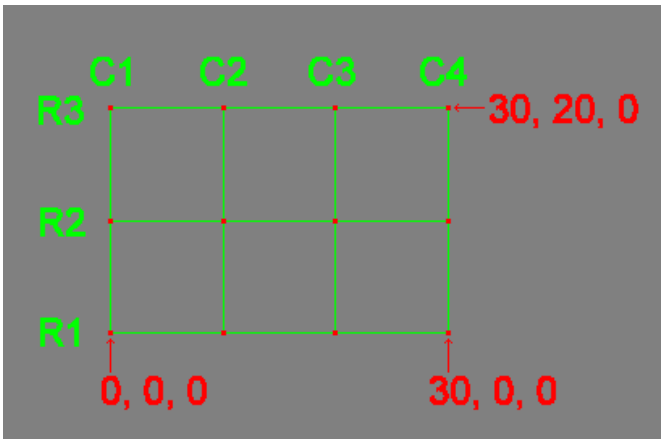

Figure 4.2. XYZ format example with all Z values at 0.

Table 4.1 Vertices of XYZ files saved by row and column (PLC).

Saved by Row	**Saved by Column**
AT3D_XYZ V01.00 Mesh A	AT3D_XYZ V01.00 Mesh A
Rows 3	Rows 3
Columns 4	Columns 4
Order By_Row	Order By_Column
Data	**Data**
0 0 0	0 0 0
10 0 0	0 10 0
20 0 0	0 20 0
30 0 0	10 0 0
0 10 0	10 10 0
10 10 0	10 20 0
20 10 0	20 0 0
30 10 0	20 10 0
0 20 0	20 20 0
10 20 0	30 0 0
20 20 0	30 10 0
30 20 0	30 20 0

4.1.3 LAS (LASer) File Format

The LAS file format is a public file format used for interchanging of 3D point cloud data between users. LAS files are an alternative to the commonly used ASCII file interchange system. Propriety systems in use are difficult to transfer between systems, which is based on two significant problem. The first problem is low performance due to slow evaluation of ASCII elevation data. This is because the file size is too big relative to the amount of data in the file. The next problem is the loss of LiDAR data specific information. The LAS file format solves these two problems as it is not too complex, and it maintains specific information. The LAS 1.4 Specification was approved by the ASPRS Board on November 14, 2011 and is the most recent approved version of the document (ArcGIS, 2019). A collection of LAS point clouds, forming a data set is shown in Figure 4.3. (GeoCue Group Support, 2019).

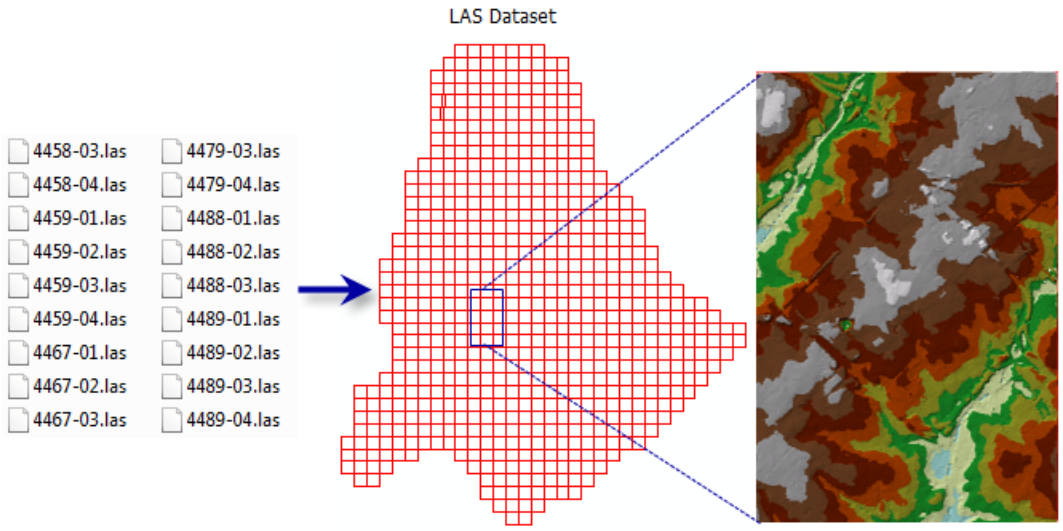

Figure 4.3. LAS dataset of an area (GeoCue Group Support, 2019).

4.1.4 MAT File Format

The .mat extension is a binary data container format developed by Mathworks to be used by Matlab software. Matlab is an application where algorithms are developed and visualized. This software is also used for computation and data analysis. MAT files data files in which variables, functions, arrays, and other information are included. MAT files can be saved in multiple formats within a version in the Matlab Preferences. (Reviversoft, 2019).

4.2 Point Cloud Data Registration

The process of aligning multiple point cloud data in a consistent model is called registration. The aim is finding orientations and relative positions of different views in a set global coordinate system. Thus, registration allows processes such as segmentation and object reconstruction to be applied on a single, complete data set. Figure 4.4. displays such an example in which a 2D laser unit is tilted to acquire a set of six individual datasets. Each of the six scans depict a fraction of the surrounding environment. Therefore, it is essential to register these together to obtain a complete point cloud model as represented in Figure 4.5. (PCL, 2016).

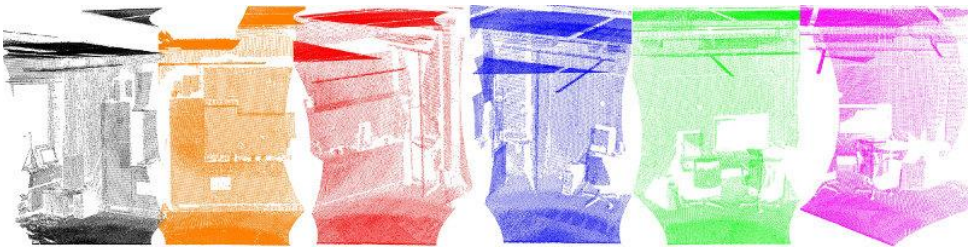

Figure 4.4. Six-point cloud datasets acquired from the same room (PCL, 2016).

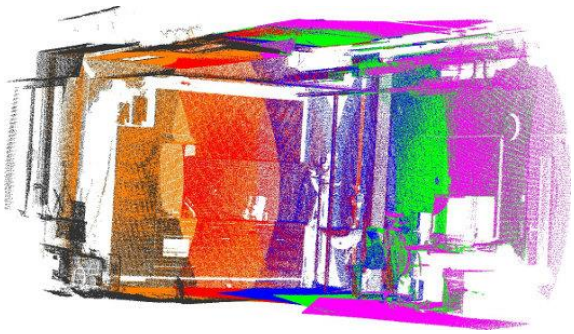

Figure 4.5. Registered point cloud data (PCL,2016).

The algorithm works to find correct matching points in the input datasets. It then estimates rigid transformations to rotate and translate each dataset to form a consistent global coordinate framework. The registration becomes easier to solve when the corresponding points in the input datasets are known exactly. The chart for the process of point cloud registration is given in Figure 4.6 (PCL, 2016).

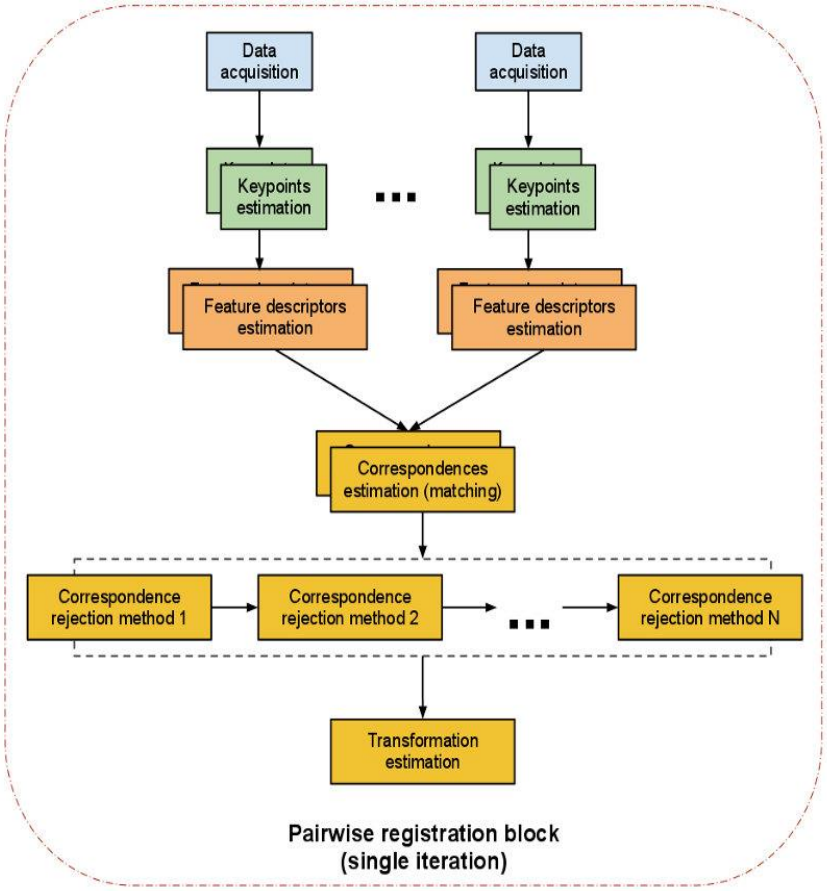

Figure 4.6. Process chart of point cloud registration (PCL, 2016).

The two datasets have straightforward steps for computation:

- Keypoints (points of interest) that best represents both datasets are selected from a point set;
- A feature descriptor is calculated at each point of interest;
- A feature descriptor set with their 3D coordinates are formed, a set of correspondence based on the similarities between features and positions are estimated;
- Poor correspondences that demerit the registration process are rejected, assuming data is noisy;
- Motion transformation is estimated from the remaining set of good correspondences.

Iterative Closest Point (ICP) is applied by Matlab in order to register two successive point clouds. Objects or world maps in 3D models can be developed for mapping and localization for simultaneous localization and mapping with ICP reconstruction.

```
dataFile = fullfile(toolboxdir('vision'), 'visiondata',
'livingRoom.mat');
load(dataFile);

% Extract two consecutive point clouds and use the first point cloud as
% reference.
ptCloudRef = livingRoomData{1};
ptCloudCurrent = livingRoomData{2};
```

The quality of registration depends on data noise and initial settings of the ICP algorithm. Preprocessing steps can be applied to filter the noise or set initial property values appropriate for the data. Here, the data is preprocessed by downsampling with a box grid filter and setting the size of the grid filter to be 10 cm. The grid filter divides the point cloud space into cubes. Points within each cube are combined into a single output point by averaging their X, Y, Z coordinates (Mathworks a, 2016).

```
gridSize = 0.1;
fixed = pcdownsample(ptCloudRef, 'gridAverage', gridSize);
moving = pcdownsample(ptCloudCurrent, 'gridAverage', gridSize);

% Note that the downsampling step does not only speed up the
registration,
% but can also improve the accuracy.
```

ICP algorithm is used to estimate the 3-D rigid transformation on the down-sampled data to align the two-point clouds. The first point cloud is used as the reference and then the estimated transformation is applied to the original second point cloud. The scene point cloud I required to merge with the aligned point cloud to process the overlapped points (Mathworks a, 2016).

The rigid transformation for aligning the second point cloud with the first point cloud is found at the beginning. This is used to transform the second point cloud to the reference coordinate system defined by the first point cloud.

```
tform = pcregrigid(moving, fixed, 'Metric','pointToPlane','Extrapolate',
true);
ptCloudAligned = pctransform(ptCloudCurrent,tform);
```

The world scene can now be created with the registered data. The overlapped region is filtered using a 1.5cm box grid filter. The merge size is increased to reduce the storage requirement of the resulting scene point cloud, and the merge size is

decreased to increase the scene resolution. The end result of a Matlab example is shown in Figure 4.7. (Mathworks a, 2016).

```
mergeSize = 0.015;
ptCloudScene = pcmerge(ptCloudRef, ptCloudAligned, mergeSize);

% Visualize the input images.
figure
subplot(2,2,1)
imshow(ptCloudRef.Color)
title('First input image')
drawnow

subplot(2,2,3)
imshow(ptCloudCurrent.Color)
title('Second input image')
drawnow

% Visualize the world scene.
subplot(2,2,[2,4])
pcshow(ptCloudScene, 'VerticalAxis','Y', 'VerticalAxisDir', 'Down')
title('Initial world scene')
xlabel('X (m)')
ylabel('Y (m)')
zlabel('Z (m)')
drawnow
```

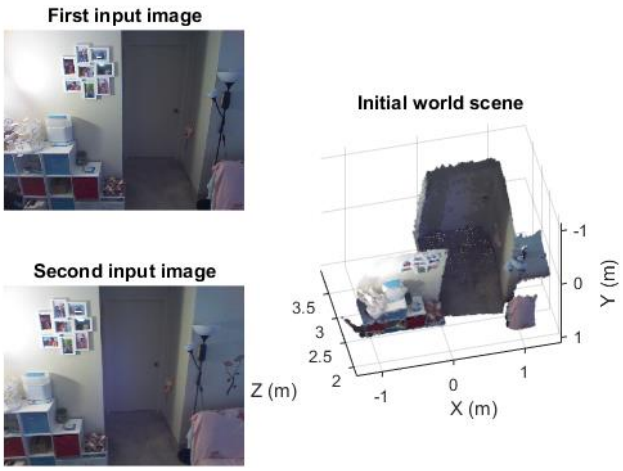

Figure 4.7. Registration of two images taken from different angles to form a 3D world scene (Mathworks a, 2016).

ICP is an algorithm that minimizes the difference in two point clouds. 2D or 3D surfaces from different scans are often reconstructed using ICP. Besl and McKay (1992) introduced the ICP algorithm.

ICP keeps the reference point cloud fixed while transforming the other point cloud to match the reference. The transformation used to minimize the distance between the reference and source point clouds is revised iteratively. The inputs into the algorithm are the reference and source point clouds and the criteria required to stop the iterative process. The output is the refined transformation.

The steps of the algorithm are:

- For each point in the source point cloud, find the closest point in the reference point cloud.
- Estimate the combination of rotation and translation using a mean squared error cost function that will best align each source point to its match found in the previous step.
- Transform the source points using the obtained transformation.
- Iterate (re-associate the points, and so on).

Iterative rigid registration is done by the algorithm, assuming all points in ***M*** corresponds with the closest point to it in ***S***. Then the least-squares rigid transformation is found. The best result is obtained when the initial position of ***M*** is close to ***S***. The pseudo algorithm is shown below:

Algorithm ICP (***M***, ***S***)
    $\theta := \theta_0$
    while not registered:
        X := Ø
        For $m_i \in T(\boldsymbol{M}, \theta)$:
        s_j := closest point in ***S*** to m_i
        X := X + $<m_i, s_j>$
    θ := least squares (X)
return θ

A point cloud data was used as mentioned in the earlier chapter. This example data has no multiple takes from different angles and as a result, required no registration.

However, to improve the running time during testing, a small area of the sample was used as shown in Figure 4.8.

The point cloud data was converted into separate X, Y, and Z vectors for easier manipulation of the data. The vectors are cropped to get a segment of the data. The resulting data were down-sampled by 1 to 10 in order to get results faster from each run of the Matlab code. The following procedures were later tested without down-sampling and the results were similar. The three vectors were then combined into a single matrix where each row represents the XYZ coordinates of a point in the point cloud.

The reason for choosing this sample area is the small area of the weathered/eroded rock surface and visibility of the two discontinuity sets. One discontinuity set has four exposed planes that have a relatively large area with more or less smooth surfaces. The second discontinuity set, however, have smaller areas combined with rough surfaces, which can prove to be a challenge when detecting the planes.

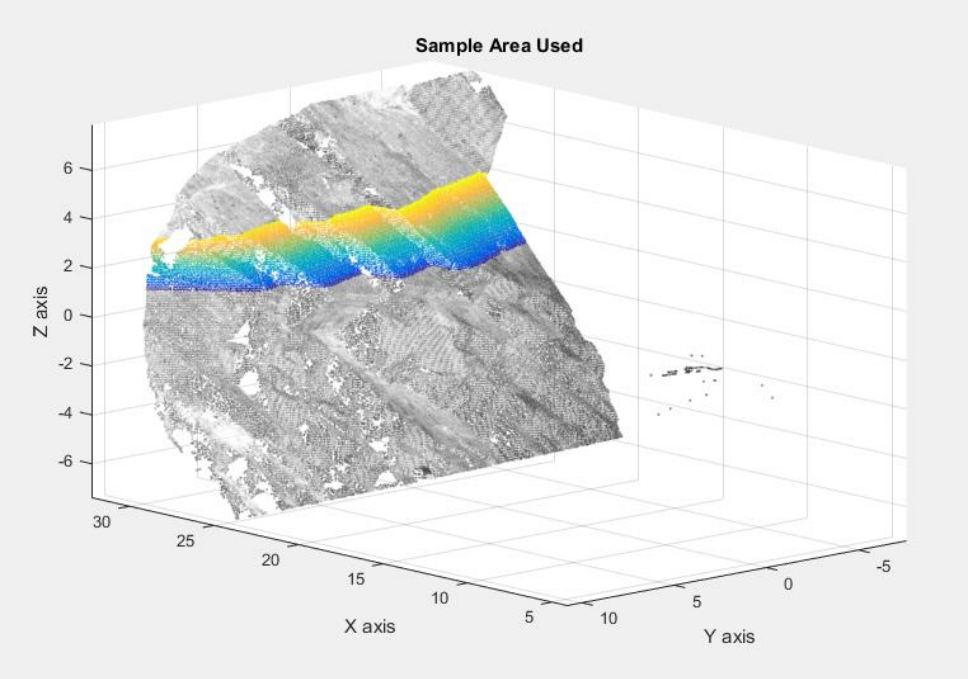

Figure 4.8. The sample area cropped from the point cloud data for experiments.

4.3 Point Cloud Data Outlier Removal

Some difficulties arise regarding laser scans. Point densities vary within point cloud datasets. Results are corrupted due to measurement errors arising from sparse outliers. Point cloud registration failures may occur and because of the errors in finding point cloud characteristics. Errors in the surface normal and curvature changes will deteriorate the estimation accuracy. A statistical analysis may be performed on the neighborhood of every point to leave out points that do not qualify, thereby resolving some of the problems. Sparse outliers may be removed first by the analysis of the point to neighbors' distances, through the determination of the mean distances between each point and all of its neighbors. The mean distances beyond a set interval described by the global mean distances and standard deviation are considered outliers and can be removed from the data. This is done with the assumption that the resulting distribution is Gaussian.

Matlab code for outlier removal (Mathworks b, 2016) and an example of its application are displayed below.

- `ptCloudOut = pcdenoise(ptCloudIn)` returns a filtered point cloud that removes outliers.
- `[ptCloudOut,inlierIndices,outlierIndices] = pcdenoise(ptCloudIn)` additionally returns the linear indices to the points that are identified as inliers and outliers.
- `[ptCloudOut,___] = pcdenoise(___Name,Value)` uses additional options specified by one or more Name,Value pair arguments, using any of the preceding syntaxes.

Next a point cloud is created.

```
gv = 0:0.01:1;
[X,Y] = meshgrid(gv,gv);
ptCloud = pointCloud([X(:),Y(:),0.5*ones(numel(X),1)]);

figure
pcshow(ptCloud);
title('Original Data');
```

Uniformly distributed random noise is added, Figure. 4.9.

```
noise = rand(500, 3);
ptCloudA = pointCloud([ptCloud.Location; noise]);

figure
pcshow(ptCloudA);
title('Noisy Data');
```

Remove outliers, Figure 4.9.

```
ptCloudB = pcdenoise(ptCloudA);

figure;
pcshow(ptCloudB);
title('Denoised Data');
```

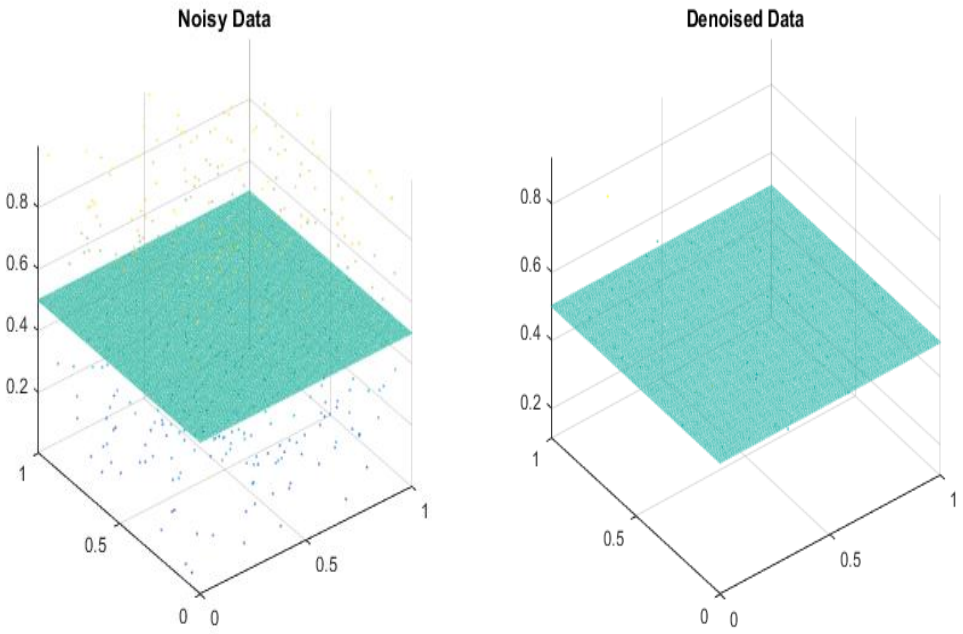

Figure 4.9. Noise added data and denoised data using remove outlier function (Mathworks b, 2016).

This very same command was applied to the point cloud sample of this study with little to no visible differences with the original data.

CHAPTER 5

PLANE DETECTION

5.1 Plane Fitting Method

In the first step after preprocessing point cloud data, the aim is to detect discontinuity planes and find their orientation with an automatic procedure. For this purpose, a plane detection algorithm is needed. The plane detection algorithm is used to discover the number of distinct planes without user input while being robust enough to ignore the imperfections of the discontinuity surfaces. Two main methods may be used to find these discontinuity surfaces. The first one is the utilization of plane fitting algorithms to detect discontinuity surfaces. The latter is the classification of point cloud data in a way that each class would represent a unique continuous surface.

Regarding the first method, i.e. plane fitting, three plane fitting algorithms were considered to see if they could adequately detect the discontinuity surfaces in the sample data. The first algorithm is the popular RANSAC algorithm. Hough Transform is another popular method. The second algorithm is the simple least-squares method. The RANSAC and least squares algorithms are tested and evaluated in detail in the following section. The point cloud sample which will be used for plane fitting is displayed in Figure 5.1. is a region of interest cropped from the data presented in Chapter 4, Figure 4.1.

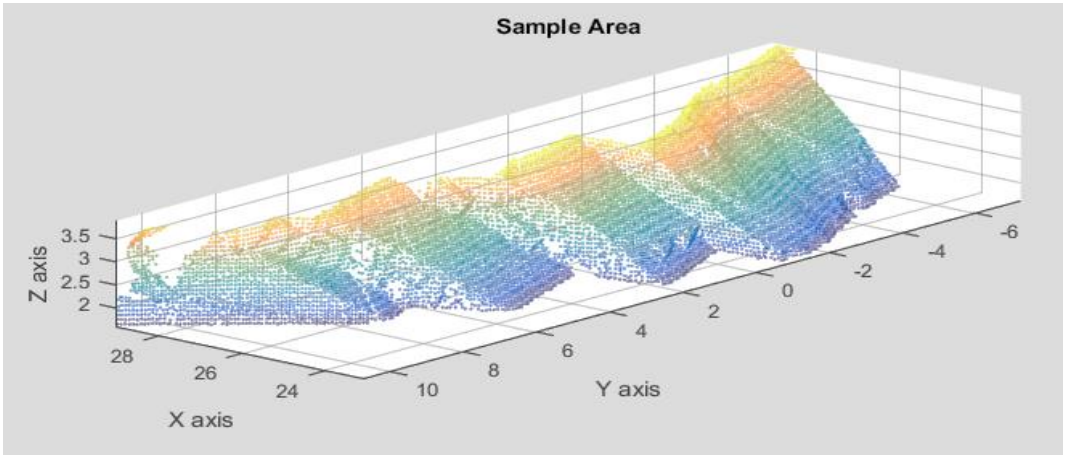

Figure 5.1. Sample point cloud data to be used for plane detection.

5.1.1 RANSAC Algorithm

The RANdom SAmple Consensus (RANSAC) is a general parameter estimation approach algorithm proposed by Fischler and Bolles (1981). The algorithm is a resampling method that generates candidate solutions by using the least amount of data points and is designed to handle a large ratio of outliers in the input data. RANSAC utilizes the smallest set available and proceeds to enlarge this set with consistent data points, contrary to conventional sampling techniques that use the maximum amount of data to obtain an initial solution and follow up by removing outliers (Fischler and Bolles, 1981).

RANSAC makes use of a voting scheme to find an optimal fitting to a dataset. Inliers and outliers should be included as data elements within the dataset as they are used to vote for one or multiple models. There are two assumptions in the application of this voting scheme. The first assumption is that the noisy features will not consistently vote for any single model (few outliers) and the second assumption is there are enough features to agree on a good model (few missing data). The RANSAC algorithm consists of two steps that are iteratively repeated (Fischler and Bolles, 1981):

1. In the first step, a small subset in the input data set is selected randomly. The dimension of the sample subset must be sufficient to determine the model parameters. The model parameters are calculated using the contents of this particular subset and a model is fitted.

2. In the second step, the consistency of the elements within the whole set with the model obtained from the estimated model parameters from the first step is checked. Data elements that do not fit the model will be labelled as outliers. In this step, some error threshold for the maximum deviation due to the effect of noise must be decided.

The consensus set consists of the set of inliers of the fitting model. The steps above will be repeated iteratively by the RANSAC algorithm until the obtained consensus set has a sufficient number of inliers.

The RANSAC algorithm needs as the input a set of scanned data values, a model for the observations, and confidence parameters. RANSAC reaches the final model by going through the steps below (Fischler and Bolles, 1981):

1. A subset named hypothetical inliers is selected randomly.
2. A model is fitted to the set of hypothetical inliers.
3. Next the model is tested against the data. Points become part of the consensus set if they fit the model with some margin of error specific to the model.
4. Should a sufficient amount of points are labelled as consensus set, then the estimated model is considered satisfactory.
5. The model can be tested against the consensus set to further improve it.

The procedure above produces a different model in each iteration. The resulting models with too few points in the consensus set are rejected. Models with size matching the consensus set are accepted. A generic RANSAC algorithm is provided in Appendix A.

It was observed that RANSAC had serious issues as a plane fitting algorithm. The initial seed points are selected randomly and as a result, the best x, y, z points change each run of the program. The resulting planes varied in each run as shown in Figure

5.2. Increasing the number of iterations helped with the accuracy of the plane fitting, however, this significantly slowed down the running time of the program.

To overcome the generic RANSAC algorithm's issues, a localized RANSAC algorithm developed for 3D data (Zaman, 2016) was tested on the sample data. Tests with the sample data show that even the modified RANSAC cannot deliver a reliable plane fitting with complex surfaces. Further modifications to this algorithm were done to enter seed points manually. Despite increasing the success slightly this modification went against the automatic application idea of the study. Not only RANSAC itself required the number of planes, the threshold used to identify a point that fits well, the number of iterations, and the number of nearby points required, but also on top of these the seed points were entered as well. As a result, the RANSAC algorithm was deemed unsuitable for this stage of the study.

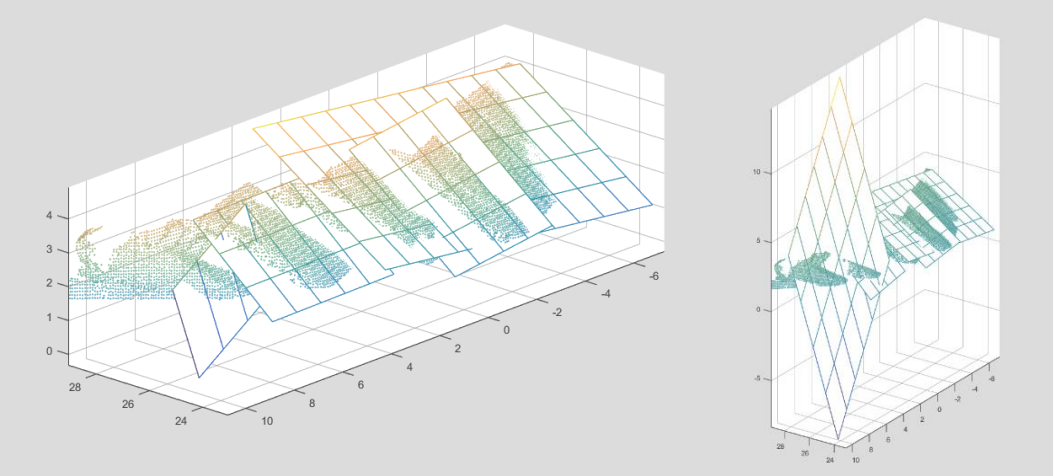

Figure 5.2. An example of RANSAC's varying results in two consecutive runs.

5.1.2 Least Squares Method

After the failure of the RANSAC algorithm, an effort to create a simple algorithm using least squares was experimented on. The idea was to use a basic method and improve its code to fit the present study's purposes. If planes representing discontinuity surfaces could be fitted into the data with accurate results and some degree of automation could be achieved, then this would be considered a success.

In cases where there are more equations than unknowns, an approximate solution is required for the sets of equations. A commonly accepted method to resolve this in regression analysis is the least-squares method. In this method, the squares of the errors made in the results are minimized in the approximate solution for every equation.

Data fitting is the most significant function in the least-squares. In terms of least-squares, the best fit is the minimization of the sum of squared residuals. These residuals are defined as the difference between observed and model values.

The following Matlab function 'Affine_fit' (Leygue, 2016) was modified to compute a plane that fits a set of data points best, using least-square of the normal distance to the plane. This code works in any dimension (2D, 3D, 4D,…) and its details are provided in Appendix B.

While this code was successful in fitting planes to the data, there were still many issues unresolved. An automated way of detecting how many planes existed in the data was still lacking. In addition, when handling multiple planes, the function will surely suffer inaccuracies similar to that of RANSAC.

In the end, both plane fitting methods were unsatisfying in proving a fast, simple, and automatic way of detecting discontinuity surfaces. A common issue both had was the inability to handle complex data. However, 'Affine_fit' function's plane fitting capabilities for single planes were impressive enough to be used later on in

the study. As a result, the next step of ideas was to utilize classification to detect the planes.

5.2 Classification and Clustering Methods

The idea of using statistical classification arises from the need to find the number of planes in a point cloud data. The process of assignment of a new observation into one of the categories in a population is called classification. This process is founded on a so-called training set of data, which contains data with known categorization. The presence of a training set makes classification a part of supervised learning. Should the classification lack any training set, then it is part of unsupervised learning. This is also named as clustering, which assigns data into clusters using some similarity measure or distance.

Since the point cloud data is to be obtained from the field and analyzed automatically without prior knowledge, no training set is available. This alone rules out supervised learning methods to detect planes in data. Clustering, on the other hand, is promising as the number of inputs required is limited. However, the problematic input in the clustering's case is the number of clusters. This causes a similar issue brought up by the RANSAC algorithm as it required entering the number of planes to be fitted. This particular issue was considered secondary as clustering had to function as a plane detector first. The initial idea was to use classification algorithms directly on the point cloud sample. For the clustering algorithm, K-means was chosen as it is a robust and commonly used method.

The commonly encountered problem of clustering can be solved with the easy unsupervised learning algorithm called K-means. This algorithm classifies a data set with a number of clusters defined prior to the procedure. The procedure is based on selecting a number of centers for every cluster. It is very important to place the centers carefully and as far away as possible from each other to avoid different outcomes resulting from a poor choice of center locations. In the following step is to

assign each point the data to the cluster of the closest center. The initial clustering is completed when every point is labelled into a cluster. Next, a new number of centers are found by calculating the barycenter of each new cluster found in the previous stage of the process. The earlier steps are repeated using these newly found centers until the latest centers found no longer move relative to the previous centers. As a final note, one of the K-means algorithm's purposes is to minimize the squared error function presented as:

$$J(V) = \sum_{i=1}^{c} \sum_{j=1}^{c_i} \left(\|x_i - v_j\| \right)^2 \tag{5.1}$$

where '$||x_i - v_j||$' is the Euclidean distance between x_i and y_j. 'c_i' is the number of data points in the *i*th cluster. The number of cluster centers is represented by 'c' (Data Clustering Algorithms, 2016),

Algorithmic steps for K-means clustering are;

Let $X = \{x_1, x_2, x_3, ..., x_n\}$ be the set of data points and $V = \{v_1, v_2, ..., v_c\}$ be the set of centers.

1. Cluster centers 'c' are randomly selected.
2. The distance between every point and cluster centers are calculated.
3. Data points are assigned to the cluster with the least distance from said point to the cluster center.
4. The equation $v_i = (\frac{1}{c_i}) \sum_{j=1}^{c_i} x_i$ is used to determine new cluster centers. The number of data in the i^{th} cluster is represented as 'c_i' in the equation.
5. The distance between every point and newly determined centers is calculated.

The process repeats from step 3 as long as new cluster centers are found. If there are no different centers, then the process stops.

The K-means algorithm was used on the point cloud data with various numbers of clusters by utilizing Matlab's own K-means command with the results presented in Figures 5.3. and 5.4. The results show that K-means disregards points being on the

same plane with the same orientation. Even though each plane is distinct enough, the nature of most classification algorithms is to find points within a certain proximity to the seed points thus ignoring whether they're on the same plane or not. Classifying each discontinuity plane required a different approach where the orientations of each plane can be classified.

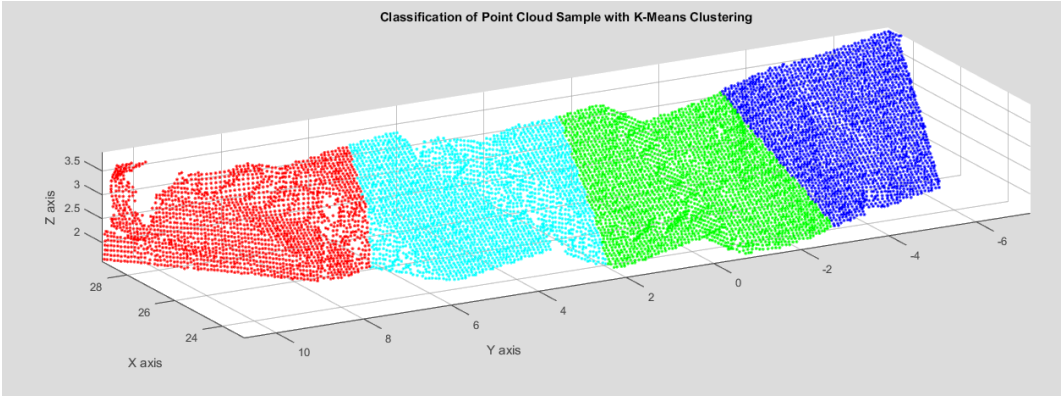

Figure 5.3. Four classes classified on study area using K-Means classification.

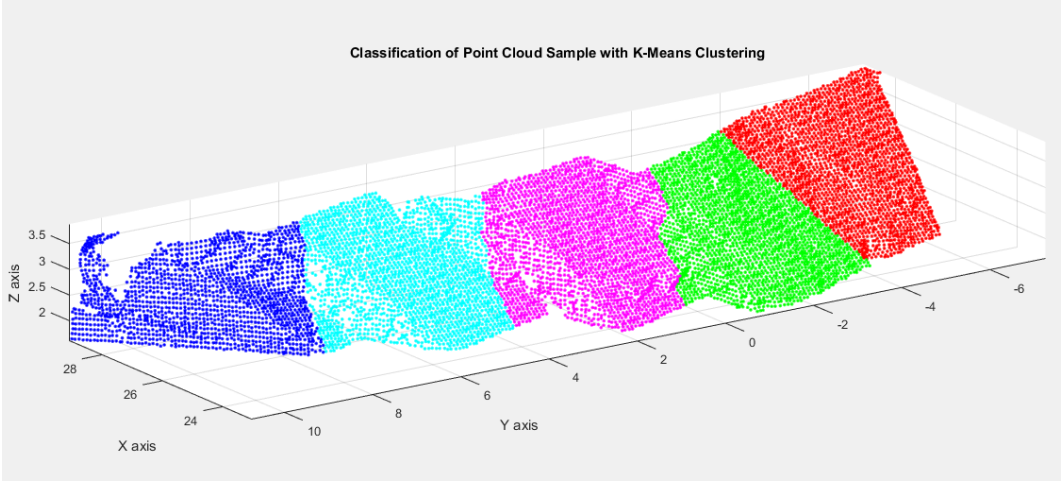

Figure 5.4. Five classes classified on study area using K-Means classification.

5.2.1 Surface Normal Estimation in Point Cloud Data

In the field, compasses can be used to find the orientation of a discontinuity surface. When plane geometry is considered, the plane equation reveals everything that is needed to be known about the plane. The plane equation can be derived from one point belonging to the plane, usually its center point, and the plane normal. The plane normal is basically a line perpendicular to the plane surface. From this line, it is possible to find the orientation of the plane, as well as the planar surfaces.

One of the more significant properties of geometric surfaces is the surface normal. This property is utilized a lot in many areas like lighting in visual effects. Inferring the normal direction of a point on a given surface is often unimportant since the normal vector will be perpendicular to the surface regardless. However, the point cloud does not fully represent the real surface. Thus, two methods are used to overcome this problem:

- Surface meshing is used to get the surface from the point cloud. Then the surface normal is computed using the mesh.
- Surface normals are deduced from the data set directly with the use of approximations.

In this study, the latter option was used since Matlab already has an in-built code for normal estimation directly at each point in the cloud.

The main idea of normal estimation once again comes down to plane fitting. Finding the normal of a point on the surface is similar to finding the normal of a plane tangent to a surface. The problem when defined in this way turns into a problem of least-square plane fitting estimation.

The estimation of the surface normal is carried out by Principal Component Analysis (PCA), which is an analysis of the eigenvectors and eigenvalues of a covariance matrix created from the nearest neighbors of the point in question. For each point p_i, the covariance matrix C is formed as shown in the following equation:

$$C = \frac{1}{k}\sum_{i=1}^{k}(p_i - \bar{p}) \cdot (p_i - \bar{p})^T, \qquad C \cdot \vec{v}_j = \lambda_j \cdot \vec{v}_j, \qquad j\epsilon\{0,1,2\} \qquad (5.2)$$

where k is the number of point neighbors considered in the neighborhood of p_i, p represents the 3D centroid of the nearest neighbors, λ_j is the *j*th eigenvalue of the covariance matrix, and v_j the *j*th eigenvector (PCL, 2016).

The orientation computed by PCA is not consistently oriented over the whole point cloud since there is no mathematical way to solve for the sign of the normal.

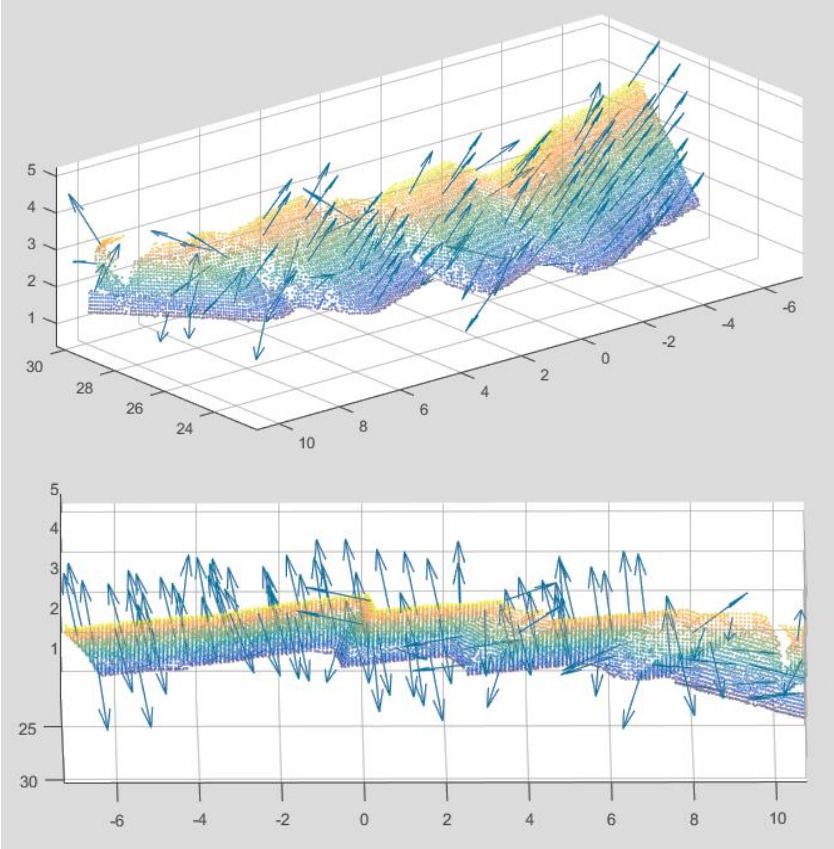

Figure 5.5. Visualization of surface normals with "quiver3" Matlab function. The normals showing the opposite direction on the same surfaces can be observed.

Even though the normal visualized in Figure 5.5. provide a neat image, it does not suit our purpose. The orientation of the surface normals can be displayed in what is called the Extended Gaussian Image (EGI). The data here show the orientation of every normal from the surface of the point cloud. In order to avoid the problem created by the sign of the normal, the absolute value of surface normal is taken. In Figure 5.6. it is noted that EGI is compressed from a sphere into a quarter of a sphere as a result.

Clusters of normal orientation points represent points that are facing the same direction thus they are on planes of similar orientation. Considering geological surfaces are not perfectly smooth, an approximation can be done for the surface. The solution to plane detection thus lies in finding large clusters of tightly packed normals.

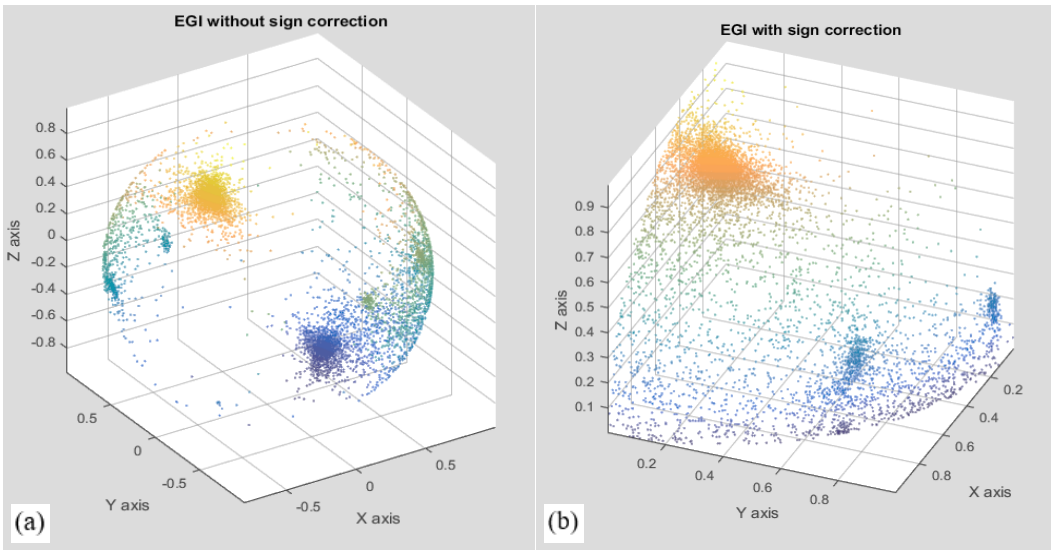

Figure 5.6. EGI of the point cloud sample before (a) and after (b) sign correction.

5.2.2 Clustering with Density Based Scanning

At this point in the study, clustering was to be applied to the EGI obtained in the previous section in order to cluster points on planes with similar orientation. Initially, the K-means clustering algorithm was tested. The results were discouraging as K-means classified every single point regardless of the fact that it made sense or not, as illustrated in Figure 5.7. Normal points that are far from clusters were added to classes despite clearly being on a different orientation.

After some trials, a density-based clustering algorithm (DBSCAN) was chosen. DBSCAN is a data clustering algorithm proposed by Ester et al. (1996). DBSCAN algorithm was modified for 3D data for the purpose of this study. With this algorithm, points far from closely packed points are tagged as outliers, whereas points with lots of neighboring points (high density) are clustered together.

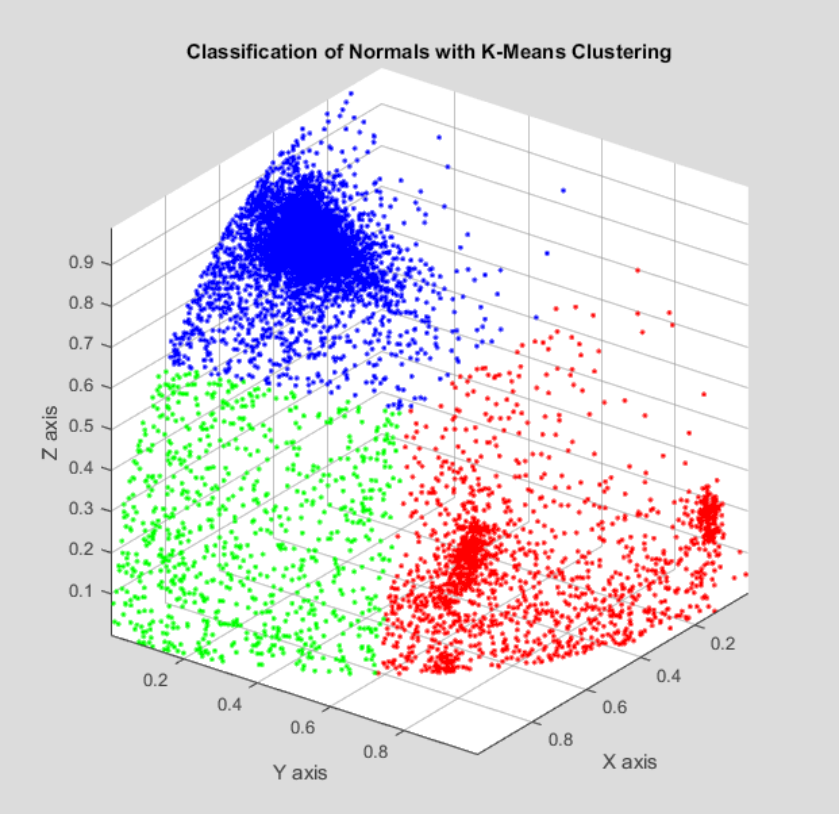

Figure 5.7. K-means applied to EGI for three classes.

ε (eps) and the minimum number of points (minPts) are two parameters necessary for DBSCAN. The process begins at an arbitrary and unvisited starting point. If the points within the ε-neighborhood are larger than minPts, a cluster is formed around this point. Otherwise, the point is labeled as noise. In the case, the point is part of a dense cluster, points within its ε-neighborhood is also assigned to that cluster. This process repeats until the entire cluster connected by the density of points is found. Once the process is over, a new starting point is selected and the process begins anew until all points within the dataset are labelled as part of clusters or as noise.

Numerous tests were conducted with different eps and minPts values and combinations, ranging from 0.1 to 0.01 and 5 to 100, respectively. While many combinations provided satisfactory results, the best clustering was achieved when eps was chosen as 0.02 and minPts was given the value of 47 for this specific point cloud sample. The results yielded three distinct clusters of surface orientations, which were visually observable in the EGI shown in Figure 5.8. Two of these surfaces were the discontinuity surfaces while the last one was a weathered surface.

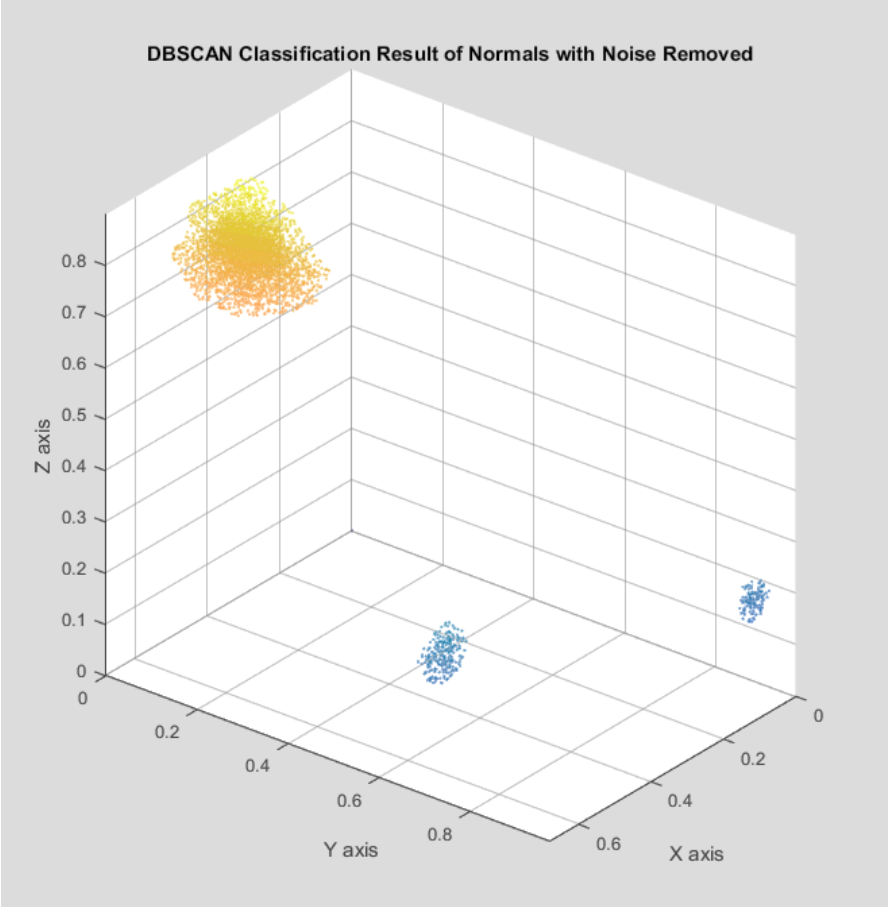

Figure 5.8. DBSCAN clustering result after the noise cluster was removed.

The DBSCAN algorithm provides a Class matrix, where point IDs are given a cluster number, 0 being the noise cluster. This caused the removal of 3948 points out of the 11484 points of the reduced (0.1 gridstep) sample. Since the ID number (row number) of a normal corresponding to a point in the point cloud, a simple code was written to match the cluster numbers with the points. The clusters are displayed with different colors in Figure 5.9 below.

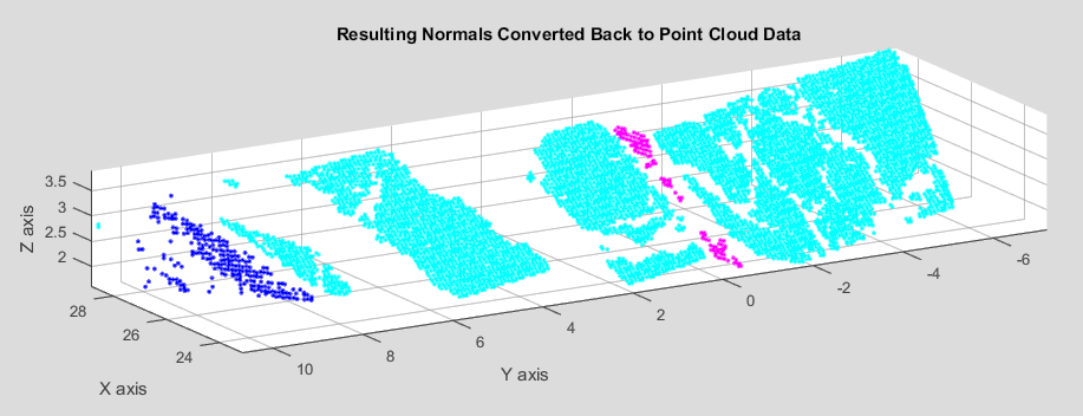

Figure 5.9. DBSCAN results on the point cloud data.

In Figure 5.9. it is seen that the cyan-colored cluster has four different surfaces. Each discontinuity surface has to be grouped within their set in order to find discontinuity properties other than plane orientation. DBSCAN is applied on the cyan cluster again. Another set of trials showed that eps (0.5) and minPts (10) were ideal for clustering the surfaces of the discontinuity set. This second clustering yielded the four surfaces as expected and are displayed below in Figure 5.10.

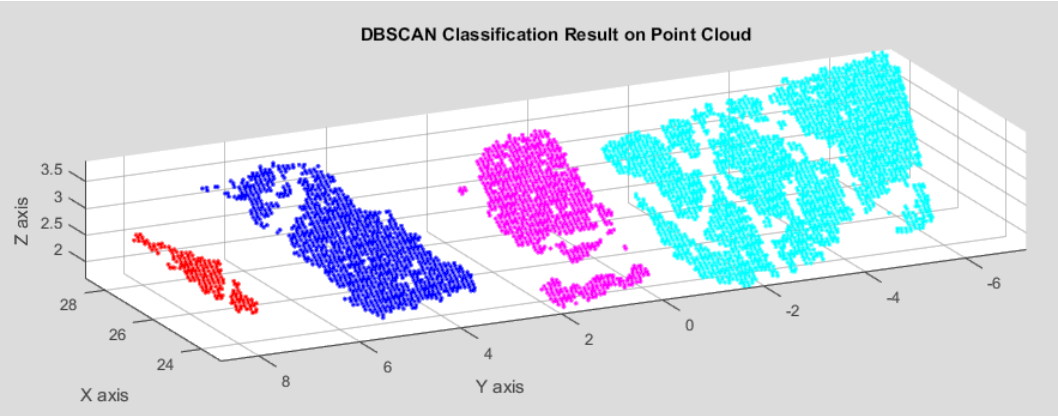

Figure 5.10. Sub-clusters based on distinct surfaces derived from the cluster based on orientation.

The DBSCAN proved to be the ideal clustering method for this study. The advantages of this method over other clustering algorithms are as follows:

- In k-means, the number of clusters prior to the process should be specified by the user. DBSCAN does not need this specification.
- DBSCAN is able to find clusters in various shapes and even arbitrary ones such as clusters surrounded by other clusters. The minPts parameter reduces the so-called single-link effect, i.e., different clusters being connected by a thin line of points.
- DBSCAN does not assign every point into a cluster as it can label points as noise. Thus, it is less susceptible to outliers.
- DBSCAN is not affected by the point ordering in the database since it needs only two parameters. However, there are cases like points at the edge of two clusters that might change cluster assignment if the point order is changed.
- An expert with a well-understanding of the data can set the parameters minPts and ε.

The disadvantages of DBSCAN are stated below:

- DBSCAN is not fully deterministic. For example, border points within reach of multiple clusters can be assigned to any depending on the order of points. However, this is a rare occasion that has minor effects on the end result. In other cases, DBSCAN is deterministic.
- DBSCAN quality can change with the choice of distance measure. The most common choice is Euclidean distance, which can become nearly useless for higher-dimensional data. This 'curse of dimensionality', which is also present in other algorithms, makes finding a suitable value for ε challenging.
- DBSCAN is mostly unsuccessful when a cluster has significant variations in density as the parameters will often fail to classify them as one cluster.
- Selecting ε for distance threshold can be challenging if the data is not well-understood.

While DBSCAN worked great in clustering the point cloud data, it is still one step away from being fully automatic. Like all classifiers, DBSCAN requires parameter inputs. These parameters are ε and minPts. Below are starting points on how to estimate these parameters.

A minimum value for minPts can be found by dataset dimension D, since minPts ≥ D + 1. Thus, in a 3D dataset, the minimum value should be 3. Larger values for minPts should be chosen however to match the size of the dataset. Usually the more points in the dataset the larger minPts should be.

In selecting the value for ε, the user first measures the distances from the selected points to k=minPts number of neighboring points on the k-distance plot. Good values of ε are obtained by the choice of a compromise value. Then the plot curves strongly. If a too small ε is chosen, then a large part of the data will not be labelled in the same cluster. If a too large value of ε is chosen, clusters will not be differentiated and the objects will belong mostly to the same cluster. In general, it is preferable to choose small values of ε since clustering all points into one big cluster will result in loss of information regarding the classification of data.

CHAPTER 6

ESTIMATION OF JOINT ROUGHNESS COEFFICIENT

6.1 Introduction

One of the significant outcomes in the determination of joint properties by the TLS approach is the estimation of the shear strength of rock joints to be used for the determination of the mechanical properties of rock masses. The empirical equation proposed by Barton and Choubey (1977) has been the most commonly used formula for the estimation of peak shear strength of a joint (Graselli and Egger 2003),

$$\tau = \sigma tan\left[JRC\ log_{10}\left(\frac{JCS}{\sigma}\right) + \varphi_b \right] \tag{6.1}$$

where τ is the peak shear strength of the rock joint, σ is the normal stress, JRC is the joint roughness coefficient, JCS is the strength of the joint wall, and φ_b is the basic friction angle. In this equation, it is possible to obtain all the parameters except JRC by standard tests. The JRC of a particular rock joint profile, however, needs to be estimated. The JRC value can be estimated by back-calculation from the shear test results using a rearranged form of Eq. (6.1) as detailed by Barton and Choubey (1977). In the absence of shear test data, the estimation is done traditionally by visually comparing the sample profile with the 10 standard profiles with JRC values ranging from 0 to 20 provided by Barton and Choubey. This approach was also adopted by the International Society for Rock Mechanics (ISRM) (Muralha et. al., 2014) and has been widely used in practice since its publication.

It has been noted that the existing empirical equations showed inconsistencies, sizable variations from one another, and most of them appeared to be correct only over specific ranges of JRC (Li and Huang, 2015). Further, it was concluded that none of the methods might be capable of providing a reasonable JRC value (Hsiung

et al., 1993). This conclusion seems to be still valid. Whether one selects the statistical parameter Z_2 and its variants or the fractal dimension for the estimation of JRC, it is difficult to choose one of the many equations proposed for use in literature for different possible applications. Each equation seems to give good results for the samples analyzed by the authors who propose different Z_2 parameters mentioned earlier. However, tests of proposed equations for the accuracy of JRC estimation for samples tested/analyzed by other researchers are not easily found in the literature. As a result of this critical examination of the major methods related to the determination of JRC of rock masses, one may conclude that there exists no universally accepted method for the accurate and reliable estimation of the value of JRC of a sample surface profile yet, in spite of a large number of research studies carried out since the publication of the major reference study by Barton and Choubey almost half a century ago.

Recent technological developments, including the development of TLS and computer software for processing cloud data, have made it possible to obtain discontinuity surfaces on long scan lines. There is still left the long and tedious task of estimating the JRC values for the large number of profiles obtained from these surfaces. Thus, the aim of this study is the development of a simple, accurate, and reliable method suitable for use in a fully automatic procedure for the estimation of the JRC of large numbers of surface profiles obtained from TLS point clouds; rather than to rigorously analyze and understand the relation between estimated JRC values and the peak shear strength of rock joints by back calculations from test samples.

A procedure is developed and proposed for the estimation of the JRC range of sample profiles based on a similarity measure between the polynomial functions fitted to the power spectral density (PSD) functions of a given sample surface profile and Barton and Choubey's 10 template profiles. As distinct from previous attempts making use of the PSD as an intermediate tool, the proposed method is based on the direct application of the PSD of the reference and sample surface profiles. The procedure is tested on the digitized surface profiles available in the literature, and the level of its accuracy is illustrated. The procedure is tested on the one hundred and two

digitized surface profiles found in the literature. To illustrate the accuracy and precision of the method, the normal probability density distribution of estimation errors of the results for the JRC estimation are compared with the results from the three versions of the well-known and commonly used Z_2 method.

6.2 Methodology

PSD has been used in a diverse list of applications such as surface characterization of optical components (Duparre et. al. 2002, Alcock et. al. 2010); surface generation in ultra-precision machining (Cheung et al.,2003); evaluation of surface changes in laser milling operations (Lorbeer et. al. 2018), and road surface classification (Durst et. al. 2011).

In a visual assessment of the roughness of a surface profile, the amplitude and the frequency content of the profile are the two major parameters that influence the perception of the level of roughness. In the literature, the effects of the statistical parameters involving the profile amplitude characteristics on the JRC value have been examined (Maerz et al., 1990; Jang et al., 2014; Zhang et al., 2014). A number of researchers noted the influence of the frequency content of the profiles and tried to incorporate this aspect into their approach to the characterization of the joint surface roughness by using the concept of the first order (primary) and second-order (secondary) asperities (Jing et al., 1992; Kana et al., 1996; Belem et al., 2000). Even though the views on the relative influence of the first and second-order asperities on the shear behavior differ among the researchers, the importance of both in capturing the actual roughness characteristics is recognized by all (Yang et. al. 2001). In a recent study, Pickering and Aydin (2015) used the Fast Fourier Transform (FFT) to decompose surface profiles into their constituent components. They tried to understand the contribution of each component by establishing the amplitude, frequency, and phase by performing FFT analysis on the original JRC profiles by Barton and Choubey (1977).

With the recognition of the importance of the frequency content as well as the amplitude of the surface profiles in determining the joint roughness, it is natural to look into the power spectral density (PSD) of the profiles as it includes both the amplitude and frequency information.

Early publications involving the spectral analysis of joint roughness mostly tried to obtain fractal dimension from the slope of PSD, rather than the use of PSD directly to determine JRC. Develi and Babadagli (1998) stated that the utility of the PSD was that it contained statistical information unbiased by the particular scan size and pixel resolution chosen by the researcher. The fractal dimension of a surface profile could be calculated from the slope of a log-log plot of power $S(k)$ versus wavenumber k. Brown and Scholz (1985) gave the functional relationship between $S_z(k)$ and the wavenumber k in the form

$$S_z(k) \alpha k^{-\beta} \tag{6.2}$$

where β is the slope of the log-log plot of S_z versus k. The fractal dimension, D, was then related to the slope, β of the log-log plot by the following equation:

$$D = \frac{5 + \beta}{2} \tag{6.3}$$

They also noted that the power spectral density of a perfectly self-affine surface has a power-law dependence on the spatial frequency of roughness, and its exponent was related to the fractal dimension of the surface.

The difficulties involved in this approach to determine the fractal dimension, however, were discussed by Klinkenberg (1994), and the major shortcomings of this method were determined to obtain the appropriate slope of the log-log plot and the noisy character of the dataset especially at higher frequencies.

Durst et al. (2011) used PSD as another parameter for profile variability to better predict the Root-Mean-Square (RMS) value of low-resolution data provided by Laser Imaging, Detection, and Ranging (LIDAR) and other means.

However, as noted by Wang et al. (2019), PSD of rock joint masses has not been used to estimate JRC directly. They recognized the usefulness of the information contained in the PSD; however, they made use of PSD of sample profiles to modify the expressions for Z_2 to propose a new roughness index PZ, rather than using PSD directly. Further, since the proposed index PZ is based on Z_2, the authors suggest that special caution should still be paid related to the sampling interval.

In the light of the foregoing analysis of the research in the literature, and noting that the statistical information contained in PSD is unbiased by the particular scan size and pixel resolution chosen by the researcher Jacobs et al. (2017), in this study a method to estimate the JRC of rock masses using the PSD of the surface profiles directly was decided.

6.2.1 Power Spectral Density

Power Spectral Density function (PSD) of a surface profile is a mathematical tool which may be used to identify the contributions of a range of spatial frequencies that make up the profile. It is most commonly used for time signals in electrical engineering, where the mean square of the zero-mean signal is attributed to the power in it. In this case, the PSD is interpreted as having a mean square value, which is proportional to power per unit frequency. On the other hand, when the PSD is used for spatial functions such as surface profiles, the mean square value of the profile will not be directly proportional to power. The formulation will still be the same, however, if one uses spatial frequency (or wavenumber) instead of temporal frequency.

The autocorrelation function of a real and stationary profile height $z(x)$ as a random function of distance x is defined by

$$R_z(\tau) = E\left[z(x)z(x+\tau)\right] \tag{6.4}$$

where *E[z(x)]* denotes the expected value of *z(x)*.

The power spectral density $S_z(k)$, where k is the spatial frequency, is defined as the Fourier transform of the autocorrelation function of the profile. (Newland 2005)

$$S_z(k) = \frac{1}{2\pi}\int_{-\infty}^{\infty} R_z(\tau)e^{-ik\tau}d\tau \tag{6.5}$$

The Fourier transform of the surface profile is given by

$$Z(k) = \frac{1}{2\pi}\int_{-\infty}^{\infty} z(x)e^{-ikx}dx \tag{6.6}$$

and it can be shown that over a finite-distance L:

$$S_z(k) = lim_{L\to\infty}\frac{1}{L}E\left[\left|Z(k)\right|^2\right] \tag{6.7}$$

Thus, if k has units of mm^{-1}, *Z(k)* has units of mm/mm^{-1}, and because of the $\frac{1}{L}$ term in Eq. (6.7), $S_z(k)$ has units of mm^3. Thus, a complete name for $S_z(k)$ is the mean square spectral density (Newland 2005). The PSD has several important properties. $S_z(k) \geq 0$ for all *k*, and Eq. (6.4) shows that $S_x(k)$ is an even function, i.e., $S_x(-k) = S_x(k)$. Further, since

$$\int_{-\infty}^{\infty} S_z(k)\,dk = R_z(0) = E\left[z(x)^2\right] = lim_{L\to\infty}\frac{1}{L}\int_0^L z(x)^2\,dx \tag{6.8}$$

for a zero mean signal, the area under the PSD gives the mean square value of the profile.

Experimental surface profiles are of finite length. Thus, in the application of the PSD analysis, if raw data is used directly, a rectangular window is automatically applied to the raw data. This is equivalent to the construction of an aperiodic function using

periodic functions. As a result, additional frequency components appear in the spectrum which is referred to as spectral leakage (Harris 1978, Newland 2005, Alessio 2016). To reduce this undesired feature, one can use a smooth, symmetric window function with zero value at the beginning and tapering to a maximum in the middle and then tapering down to zero again. Such a window acts as a low pass filter and reduces the spurious high-frequency components (Jacobs et. al. 2017). Hanning, Hamming, Bartlett, Welch, Parzen, and Blackman windows are the most popular windows. (Alessio, 2016)

For the numerical calculation of the PSD of a sample surface profile, there are several techniques. The most commonly used tools for this purpose are the traditional periodogram and its variant, the Welch method (Alessio 2016). Periodogram represents the simplest and classical tool for spectral estimation using discrete Fourier transform (DFT). An estimate of the power spectrum is obtained taking the Fourier transform of the autocorrelation. If a specific window is not implemented, a rectangular window is applied by default. A practical tool for this purpose is the periodogram command available in Matlab platform in the form

```
[pxx,k] = periodogram(x,window,nfft,fs)
```

where x is the discretized sample surface profile data, window is the window function to be used, and nfft is the number of points in the DFT, and fs is the sampling frequency. It is possible to select a window function among the 10 most popular windows, and a user-defined window facility is also provided.

6.2.2 Proposed Procedure

Various approaches to the discretization of 10 reference surface profiles have been described in the literature (Tatone and Graselli 2013; Jang et al., 2014; Li and Huang, 2015). Tatone and Graselli (2010) indicated that, since the original profiles were obtained with an instrument capable of sampling intervals above 0.5 mm, decreasing the sample interval will not provide any additional information. Digitized reference surface profiles sampled at 0.4 mm provided by Li and Zhang (2015) can be found in the online version of the publication, and data sets from this source are used to plot the original and digitized standard profiles in Figure 6.1. In the published literature, it is common to de-trend the data and work with zero mean profiles. As indicated by Durst et al. (2011) indicated that if raw data are used a non-zero value is obtained for the direct current (DC) offset, which may contain information about the profile's overall variability. In the procedure described here, the profile data were detrended using Matlab's 'detrend' function.

The PSD of the 10 reference profiles is obtained using the periodogram command. The Hamming window with a number of points equal to that of the data set is applied, and the same number of points is used in the DFT. The power function in the form

$$PSD_{pf} = Ak^{-b} + C \tag{6.9}$$

and the third-order polynomial function

$$PSD_{polyf} = a_1 + a_2 k + a_3 k^2 + a_4 k^3 \tag{6.10}$$

have been fitted to the PSD plots. Third-order polynomial fits are computationally more economical with respect to power fits and therefore preferred in the study. In Figure 6.2, the log-log plots of PSD versus spatial frequency are shown with the superimposed third-order polynomial fits. These plots now become the templates against which any sample surface profile is to be compared for the estimation of its JRC.

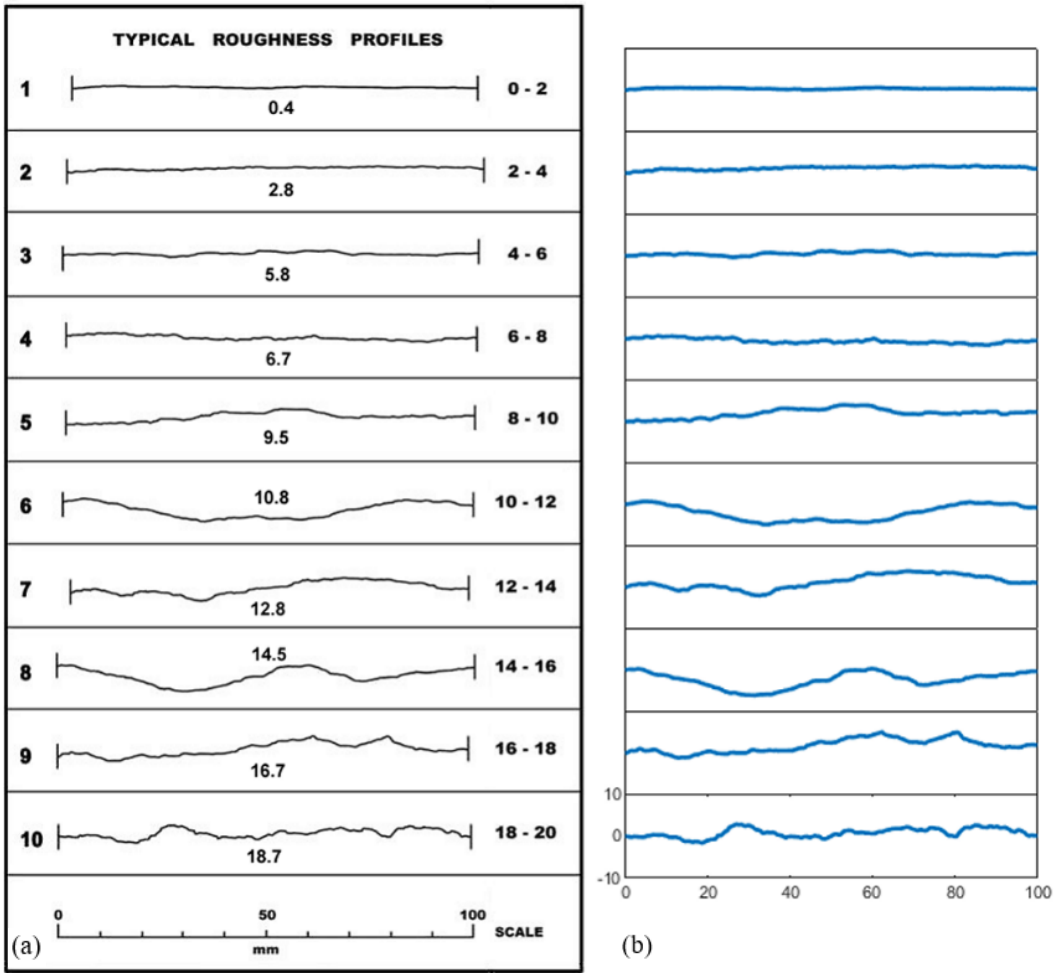

Figure 6.1. Reference profiles from Barton and Choubey (1977) (a) and their digitized plots (b).

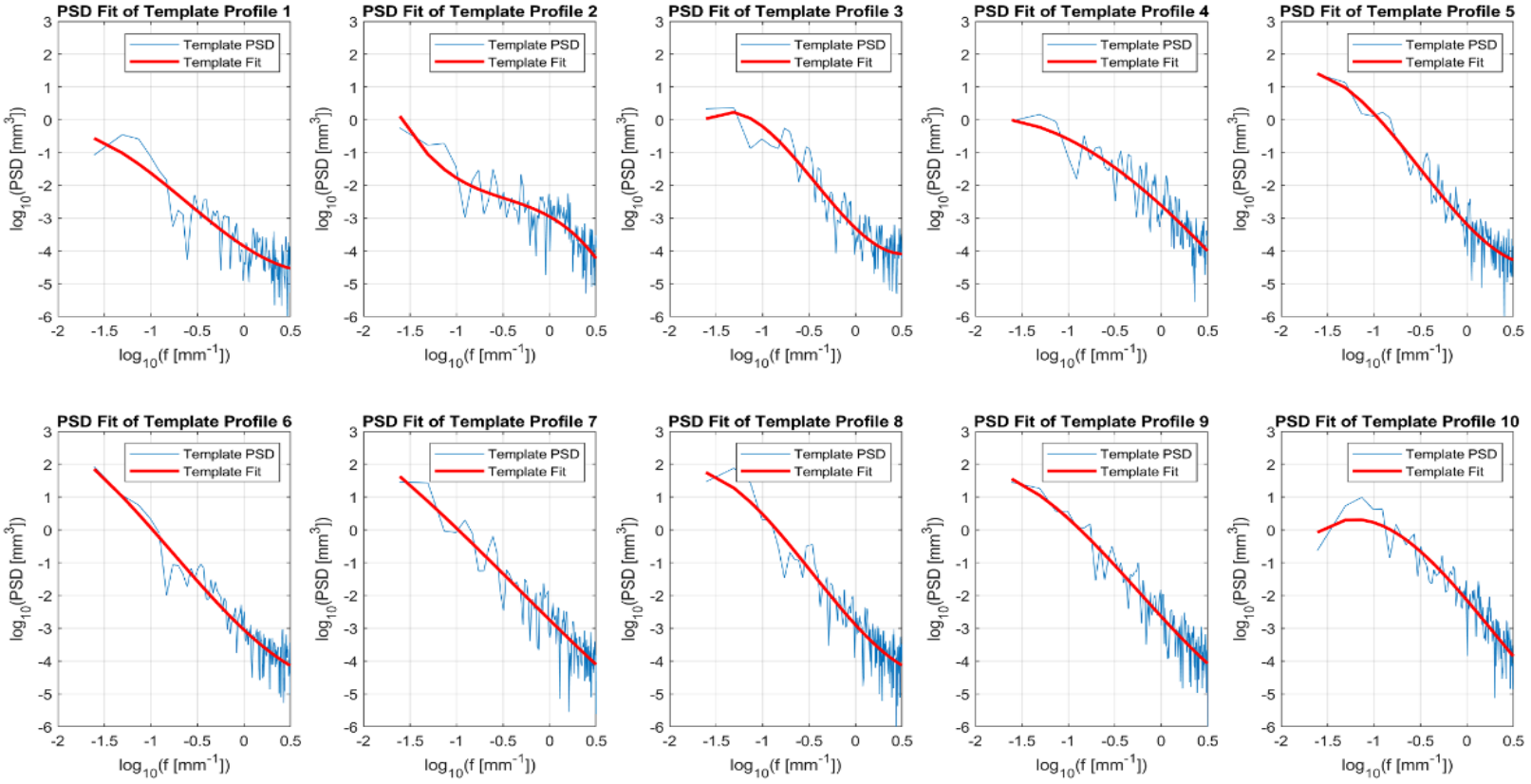

Figure 6.2. PSD plots of reference profiles from Barton and Choubey (1977).

For the estimation of a given surface profile sample, the sample data is treated in the same way as the reference profiles, and its PSD plot with the third-order polynomial fit is obtained. The lengths and the sampling rate may be different for the sample profile. Thus, the profile needs to be resampled to equalize the number of data points. In order to avoid extrapolation which distorts the data points at the edges, profiles or templates with more data points are downsampled to match the one with a lower number of data points. As an example, a sample profile from Bandis et al. (1983), together with the 8th template from Barton and Choubey (1977) as well as their third-order polynomial fits on the PSD plot of the template are shown in Figure 6.3. It is observed that the PSD fits of the sample and templates are quite similar with some deviation at the lower end of the spatial frequency range.

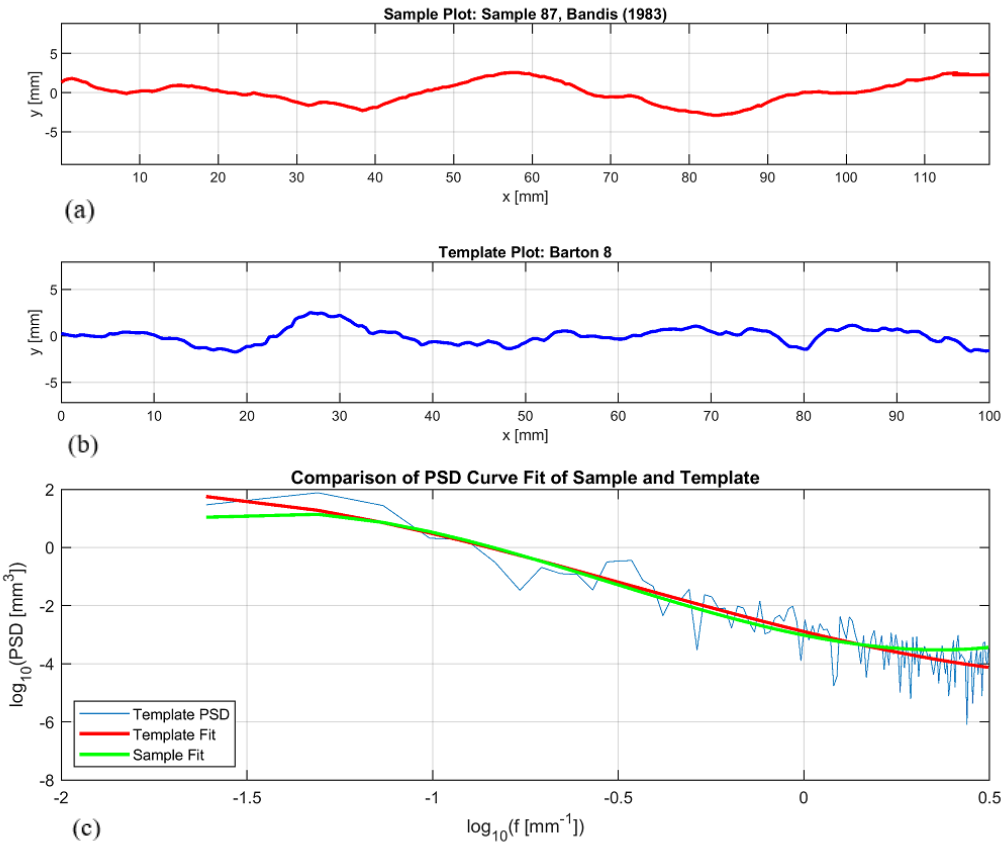

Figure 6.3. Sample (a) and template (b) profiles and polynomial fit superimposed on the template PSD (c).

To estimate the JRC of a sample profile, its third-order polynomial PSD fit is superimposed on the third-order polynomial fits of all 10 templates. As an example, the third-order polynomial fit for a sample profile from Bandis et al. (1983) is superimposed on the third-order polynomial fits of the 10 templates, as shown in Figure 6.4. Thus, the problem is now reduced to the selection of the template having a polynomial fit, which has the highest level of similarity with the polynomial fit of the sample profile. In Figure 6.4, it is relatively easy to see the best fit is obtained with template 8, i.e., JRC range 14-16 with the measured JRC value of 14.1. The similarity between the polynomial fits may not always be so obvious. Further, for an automatic estimation, an objective parameter that can differentiate the similarities between the sample and the templates is needed. Thus, to assess the similarity between the sample and template PSD characteristics objectively, an approach based on the difference between the areas under the polynomial fits of the sample and template curves has been adopted.

In the final stage of the procedure, the difference of area under the sample curve and each template is calculated numerically. The JRC range of the template that has a minimal area between it and the sample profile is assigned as the JRC range for the sample profile, as shown in Figure 6.4. It is now also possible to estimate a JRC value for the sample profile using the area differences for the ranges before and after the JRC range assigned. For this purpose, a rough interpolation, which involves the back-calculated JRC values of the template profiles by Barton and Choubey, is made. The structure for the interpolation is shown in Figure 6.5.

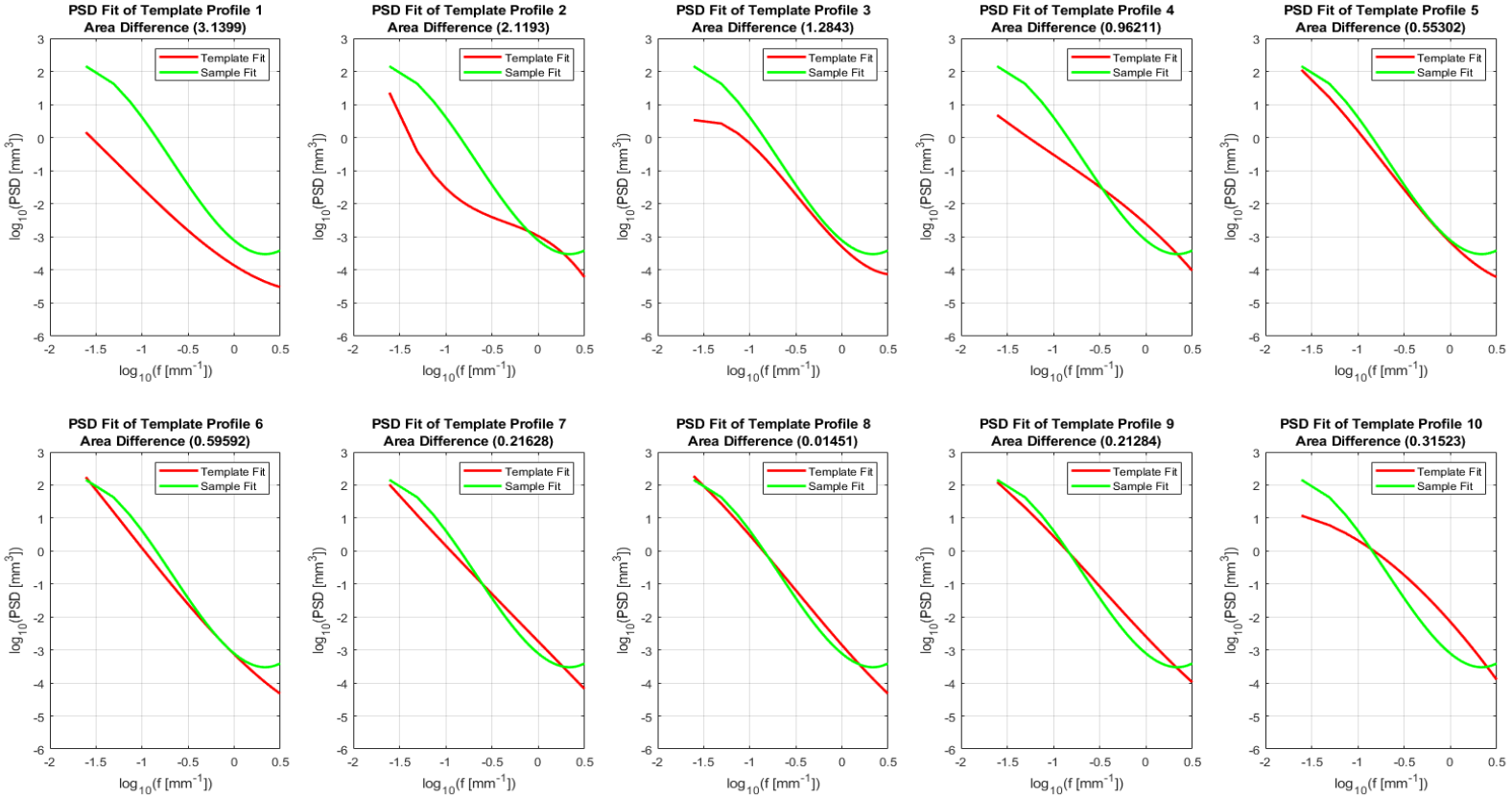

Figure 6.4. Comparison of sample polynomial fit with template polynomial fits.

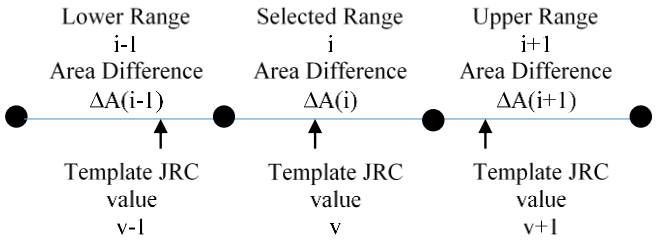

Figure 6.5. Interpolation structure.

In the interpolation procedure, the area differences for the ranges before and after the assigned JRC range, $\Delta A(i-1)$ and $\Delta A(i+1)$, are compared. If $\Delta A(i-1)-\Delta A(i+1)$ is positive, then an interpolation using the assigned and following ranges is performed. For this purpose, the ratio of the area differences $\Delta A(i)-\Delta A(i+1)$ to the template JRC value difference $v(i)-v(i+1)$ is multiplied by the area difference $\Delta A(i)$ for the assigned range and is added to the template JRC value $v(i)$. If the difference in the comparison is negative, then the same interpolation is performed using the previous and the assigned ranges. The interpolation algorithm is given in Eq. (6.11).

$$JRC_s(i) = \begin{cases} v(i) + \left[\dfrac{|\Delta A(i) - \Delta A(i+1)|}{|v(i) - v(i+1)|}\right]\Delta A(i), & \Delta A(i-1) > \Delta A(i+1) \\ v(i) - \left[\dfrac{|\Delta A(i) - \Delta A(i-1)|}{|v(i) - v(i-1)|}\right]\Delta A(i), & \Delta A(i-1) < \Delta A(i+1) \end{cases} \tag{6.11}$$

When the selected range corresponds to the first or last range, the interpolation is performed using the selected, and upper or lower range values, respectively.

The steps of the proposed procedure are summarized below.

1. Prepare the templates. It is suggested to use the digitized template surface profile provided by Li and Zhang (2015) sampled at 0.4 mm. Detrend the data and obtain the PSD for each template and fit a third-order polynomial function to each.

2. Select a section of the sample profile with a nominal length of 100 mm. Discretize, preferably, with a sampling frequency of 0.4, i.e., 251 points. Detrend the data.

3. Use the periodogram algorithm to obtain the PSD of the sample surface profile.

4. Fit a third-order polynomial function to the PSD of the sample surface profile.

5. Calculate numerically the area differences between the PSD function fit of the sample profile and the PSD function fits of the 10 templates.

6. Determine the template for which the smallest area difference is obtained. This will indicate the JRC range to be assigned to the sample profile.

7. An estimate of the JRC value for the sample surface profile may be obtained by making use of an interpolation algorithm involving the back-calculated JRC values of the templates and the area differences for the selected range and the ranges just before and after it.

The method is simple since it consists of a few basic steps only, after the sample profile data has been obtained and preprocessed, a step which is essential in any method. All the steps above are of minimum mathematical complexity, can be performed by common software functions, and if needed the algorithms are readily available in practically all computer languages. Further, the 1st step of the proposed procedure is to be performed once only, as long as the sampling interval for the sample surface profile is not more than 0.4 mm.

In an application in which discontinuity surface data is obtained from the TLS cloud, a 2D surface profile can be extracted, and step 2 can be carried out. A graphical user interface is prepared, and the proposed procedure is implemented to carry the steps starting from step 3 automatically, once the selected sample profile data is loaded. It can be added as a module in a TLS based interactive/semi-automatic/fully automatic computer program to obtain the relevant properties of discontinuities in rock masses.

6.3 Discussion of Results

To evaluate the performance of the proposed procedure, tests are carried out using the source data provided by Li and Zhang (2015), which include 12 digitized profiles from Graselli (2001), 26 profiles from Bandis (1983), and 64 profiles from Bandis (1980). The back-calculated JRC values from tests are also available for these surface profiles. Estimated JRC values for these sample profiles obtained using the proposed method are compared with the back-calculated JRC values in Figure 6.6.

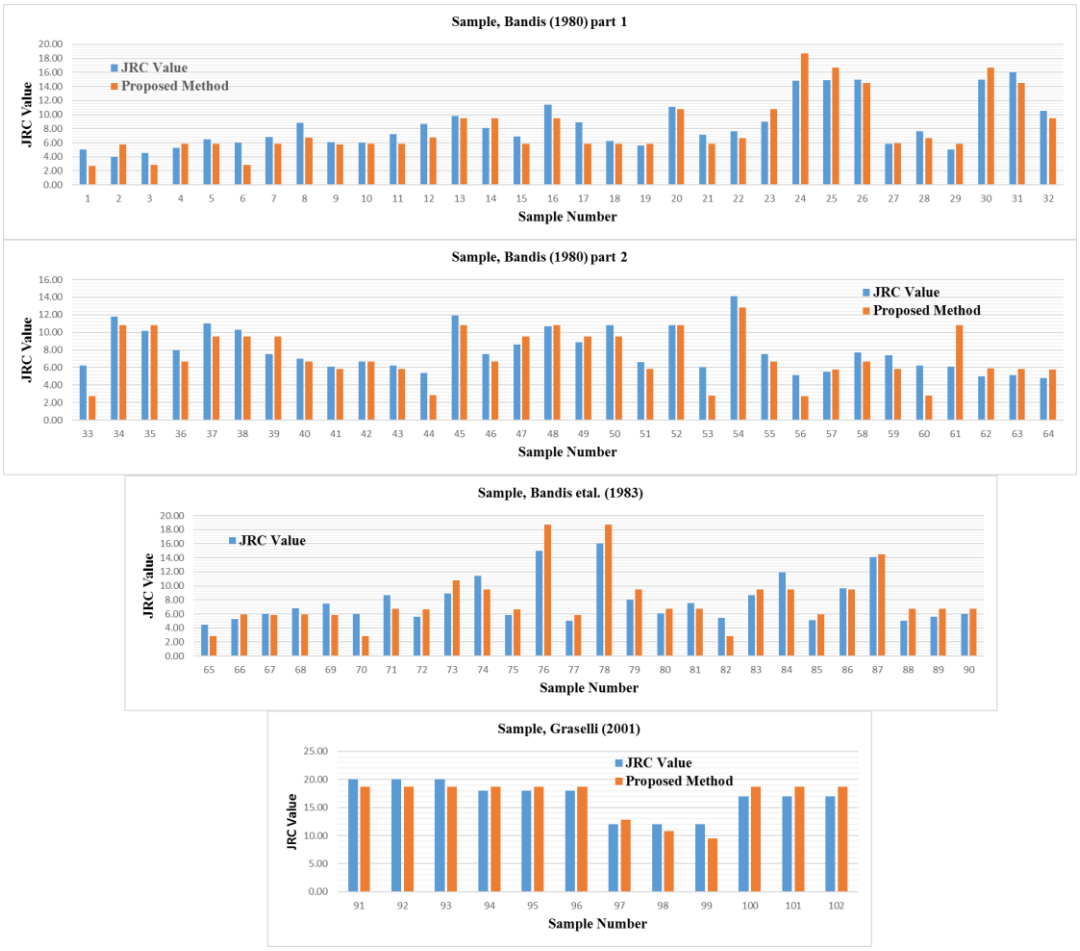

Figure 6.6. Comparison of back-calculated and estimated JRC values.

The Gaussian probability distribution function of the JRC estimation error for the proposed method is given in Figure 6.7. The same plots for the JRC estimation using the Z_2 relations for 0.4 mm sampling interval given by Tse and Cruden (1979), Taton

and Graselli (2013), and Jang et al. (2014) are superimposed on the figure. The mean values and the standard deviations of JRC error estimations for these methods are listed in Table 6.1. The mean values are indications of the accuracy of the JRC estimations, i.e., how close the results are to the true value. The standard deviations correspond to precision. Precision is defined as the degree to which repeated operations under unchanged conditions show the same results and is considered as an indicator of reliability.

The mean estimation errors show considerable shifts to positive values for Z_2 based relations. Thus, these methods overestimate the JRC values, in general. The proposed method, on the other hand, results in almost zero mean estimation error, which means that its accuracy is better. The estimation error is likely to result in a small underestimation, and thus a slightly conservative value of JRC. Further, the standard deviation is smaller for the proposed method. Thus, one may conclude that the proposed method is better both with respect to accuracy and precision when compared with the commonly used statistical approaches to the estimation of JRC.

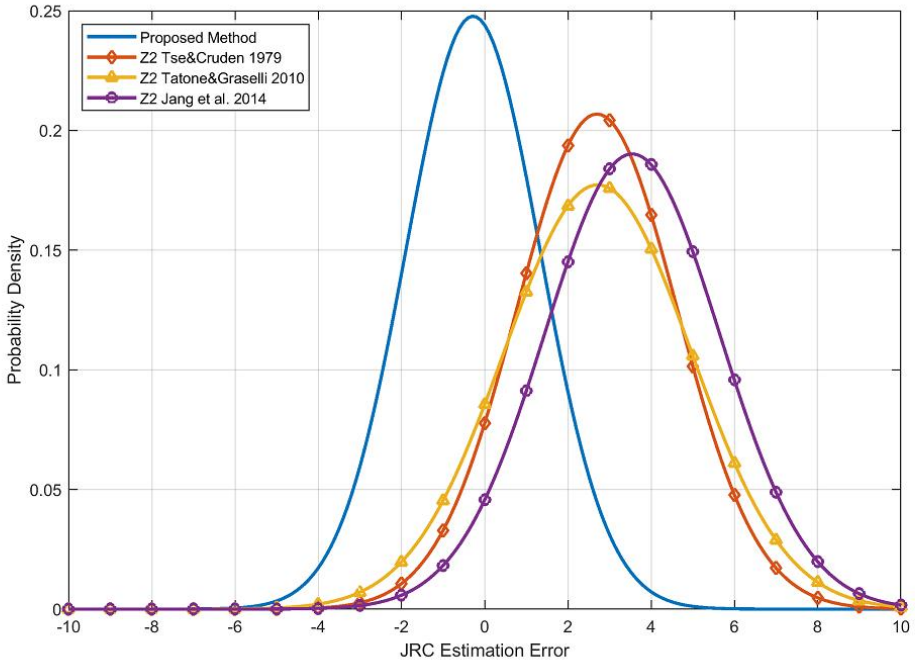

Figure 6.7. Normal probability density distribution of estimation errors.

Table 6.1 Means and standard deviations for JRC estimation.

Method	**μ**	**σ**
Proposed method	-0.281	1.610
Tse and Cruden (1979)	2.698	1.929
Tatone and Graselli (2010)	2.715	2.250
Jang et al. (2014)	3.536	2.105

The proposed method makes use of the entire PSD plot of both the sample and template profiles. However, parts of the PSD plots contain noise or unnecessary information due to spectral leakage. In order to minimize this effect, the PSD plots were trimmed on both low and high frequency ends to see if the results of JRC estimation improved or not. In the first test, the left 50% of the PSD plots and the right 50% were tested separately, as shown in Figure 6.8.

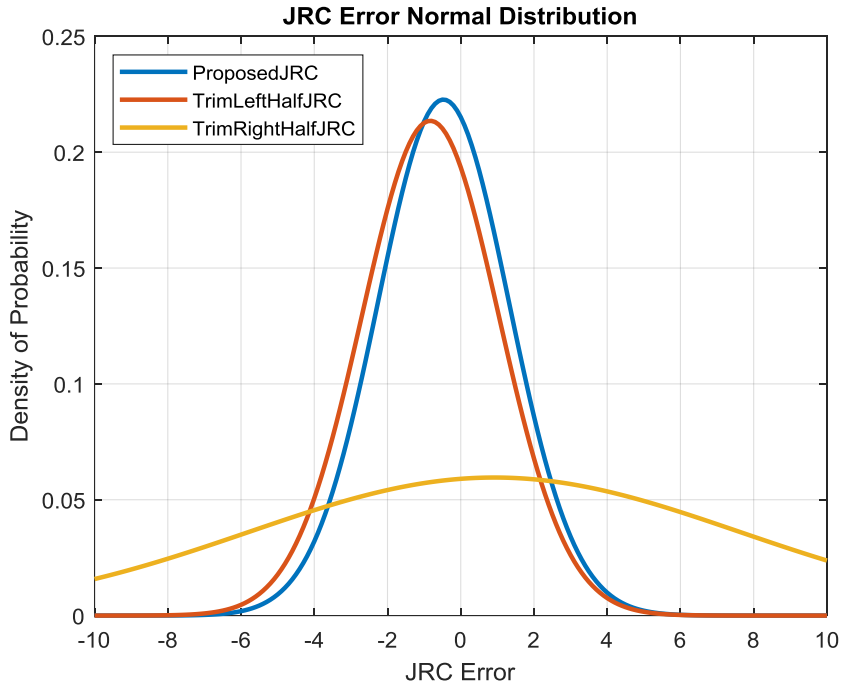

Figure 6.8. Normal probability density distribution of estimation errors for the proposed method (blue) and trimmed PSD plots of high frequency (red) and low frequency (yellow).

The results clearly display that the right 50% of the PSD plots, which correspond to the lower frequencies, lack any form of precision while the left 50%, which corresponds to higher frequencies, are very close to the proposed method. This shows that the JRC estimation results are either affected mostly by higher frequencies or the spectral leakage noise is too much in the lower frequencies. Despite this observation, the lower frequencies may still contain information. Thus, the PSD plots were trimmed at different percentages from lower frequencies and the results are displayed in Figure 6.9.

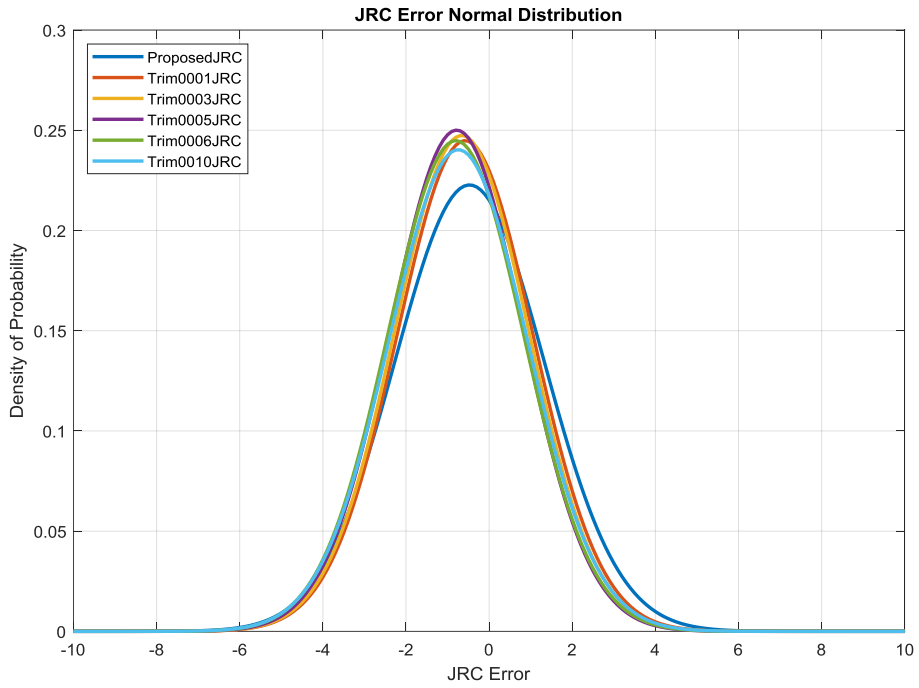

Figure 6.9. Normal probability density distribution of estimation errors for the proposed method and trimmed PSD plots of low frequency (1%, 3%, 5%, 6%, and 10%).

The results are a significant improvement over the proposed method. It is evident that trimming the lower frequencies which are subject to spectral leakage improves the precision of the JRC estimation. Comparing the 1%, 3%, 5%, 6%, and 10% trimmed plots, it can be seen that precision increases and peaks at 5%, then begins to decline at 6% and beyond. From this, it can be said that trimming 5% from the low-frequency end of the PSD plots yields the best results. However, it should be noticed that there is a slight increase in negative bias. Additionally, the effects of trimming the high-frequency end and low-frequency end in different percentages are to be tested as well to find an optimal trimming, Figure 6.10.

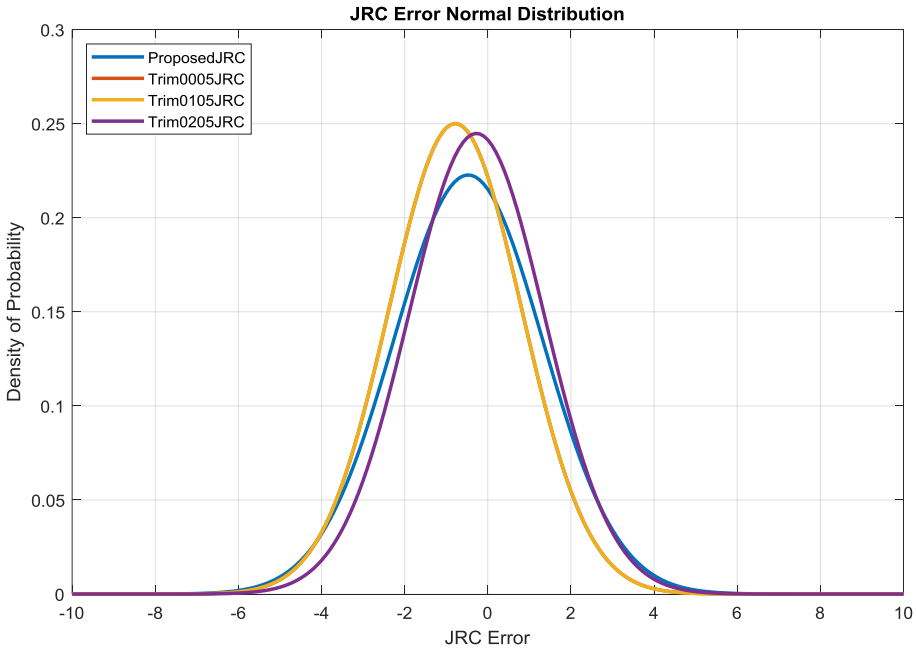

Figure 6.10. Normal probability density distribution of estimation errors for the proposed method and trimmed PSD plots 5% at low frequency and 0%, 1%, and 2% at high frequency ends. Red and yellow plots overlap.

In these plots, the trim at the low-frequency end is kept at 5% while the trim at the high-frequency end changes between 0%, 1%, and 2%. The first thing of notice is that 0% and 1% trims overlap completely. This shows that 1% of the high-frequency end of the PSD plots hold no information regarding JRC estimation. As the trimming percentage increases, it can be seen that the precision gets lower. However, the negative bias of JRC estimation is also lowered. From these results, the 1% and 5% trim and the 2% and 5% trim give close and significantly better results than the full PSD plot results. Determining which one of these two is better, brings up the accuracy-precision bias problem. The former has higher precision but lower accuracy while the latter is the opposite. In this study, the latter is chosen as the negative bias in the former is worse than the original proposed method. In addition, the difference in precision is not great enough. As a result, it is advised to trim 5% from low frequency and 2% from high-frequency end.

Applications requiring analyses of discontinuity surfaces of rock masses on very long scan lines involve the assessment of large numbers of surface profiles for JRC estimation. This task is time consuming, laborious, and costly. Obtaining JRC values by standard tests is not practical, either. The use of the popular methods available in the literature, on the other hand, presents the engineer in charge to choose among a large number of equations proposed for the same purpose. Further, some of these methods are based on procedures that require extensive mathematical operations and are not suitable for use in automatic assessment. A straightforward procedure which is easily implemented in the automatic estimation of JRC for the discontinuity surface profiles, while at the same time is at least as accurate and reliable as the well-known and commonly used methods, is needed.

The method proposed in this study can be used for automated processes in JRC estimation for large numbers of sample profiles. As distinct from previous attempts making use of the PSD as an intermediate tool, the proposed method directly uses the PSD of the reference and sample surface profiles. The procedure is based on the similarity between the PSD of the sample and the 10 JRC template profiles. It is not influenced by the sampling frequency and does not require separate correlations for surface profiles sampled at different intervals. The comparison of the results with those from the well-known and commonly used Z_2 method, in trials with a large number of cases available in the literature, show that the method yields more accurate and precise estimations. Another positive aspect of the proposed method is the almost zero mean for the estimation error as compared to the considerable positive estimation error for the well-known and commonly used Z_2 method. The proposed method is particularly suited to the automatic evaluation and can be easily programmed as a module that can be embedded into larger software for the determination of discontinuity properties of rock masses.

CHAPTER 7

APPLICATION OF PROPOSED METHOD TO A CASE AREA

Point cloud analysis involves large amounts of data and requires complex calculations through processes with a relatively high number of steps. To carry out these steps, an easy to use and flexible Graphical User Interface is to be developed for time efficiency. The commercial software Matlab (2019a) has many useful commands and utilities that are used in point cloud applications. In this study, a special GUI, Discontinuity Analysis, on the Matlab platform is developed. The GUI is designed in modular form and as such can be further extended and modified without damaging its integrity.

The main window of the GUI is shown in Figure 7.1. The GUI consists of three main sections that can be seen as three columns on the main window. The three columns of the GUI are used consecutively for the complete analysis of a data set. They can be used, however, independently if appropriate data is available. The GUI also contains an independent module, Profile Analyzer, which can be accessed by a button in the lower right corner of the window, for detailed surface profile analysis for the estimation of the JRC of a sample profile.

Details on the design and capabilities of the GUI are given in this chapter. The algorithms and equations used to extract discontinuity sets and determine their properties are explained in detail. The use of the software is also illustrated with a case study throughout the chapter in which all the calculations are carried out step by step.

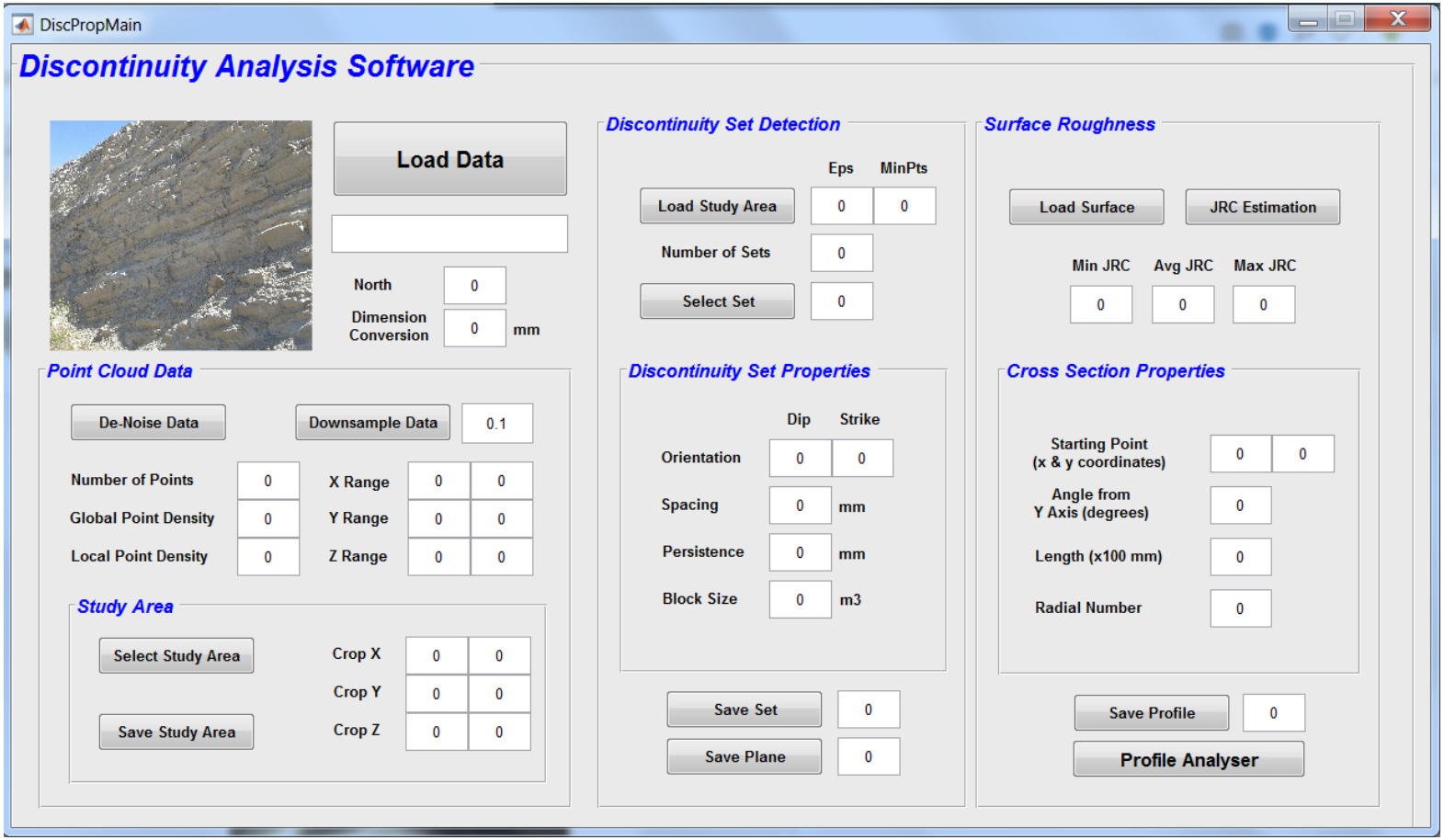

Figure 7.1. Matlab GUI for Discontinuity Analysis

7.1 Data Loading and Preprocessing

The point cloud data of a rock slope excavated for limestone in El Campello, Spain named ‘00 Raw data - Site10 Ouray1 – Mesh.ply’, obtained from Riquelme et al. (2014), is used in the work in order to test the capabilities of the algorithms to be used in the Matlab program. The point cloud data and its photograph are displayed in Figure 7.2. The sample is three meters long across the Y-axis. It has two distinct and visible joint surfaces in its upper half. The lower half has been weathered severely, thus hiding the joint surfaces. A slice from the upper half was taken to experiment with possible ways to detect discontinuity planes of the joints.

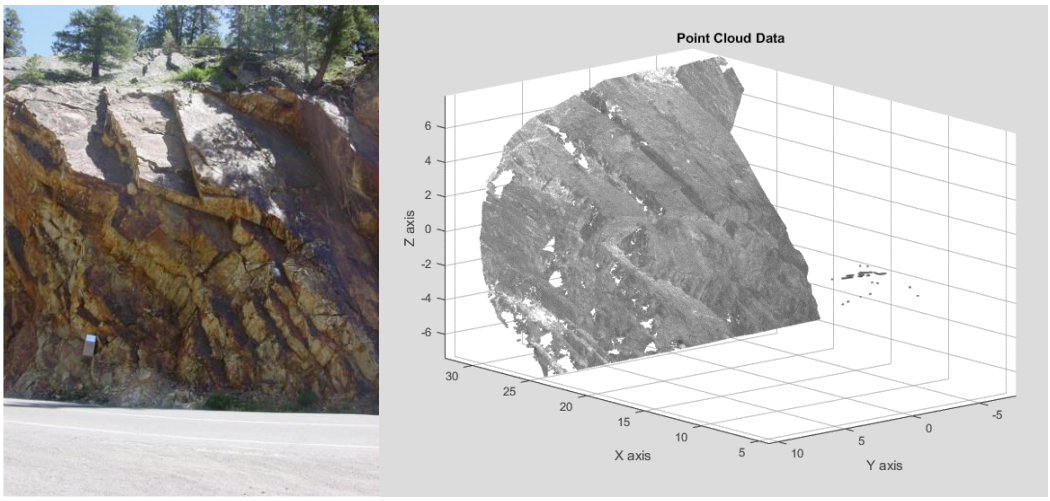

Figure 7.2. Point Cloud data used for Matlab case study and its photograph, Riquelme et al. (2014).

The first section of the GUI is for loading point cloud data and perform preprocessing. The ‘Load Data’ button opens a browser that starts in the ‘Samples’ folder. Three types of point cloud data, including .ply, .las, and .mat, can be loaded. The software will extract the data from point clouds and form a .mat array called ‘obj’. Each row of ‘obj’ is a point with x, y, and z coordinates. This 3D array is then displayed in a window named ‘Figure 1’ using the pcshow function of Matlab as seen in Figure 7.3.

The program assumes the azimuth (north) is along the Y-axis. However, it is possible to change the north direction by entering an angle value next to the ‘North’ section of the GUI. This will rotate the north clockwise by the amount entered in degrees. ‘Dimension Conversion’ section is for converting Matlab’s distance unit into millimeters. In the case of the data used in this study, the Y-axis is known to be three meters (3000 mm) in length. Since the difference between the minimum and maximum Y values is 18.4194, the value to be entered next to ‘Dimension Conversion’ is 162.872 mm.

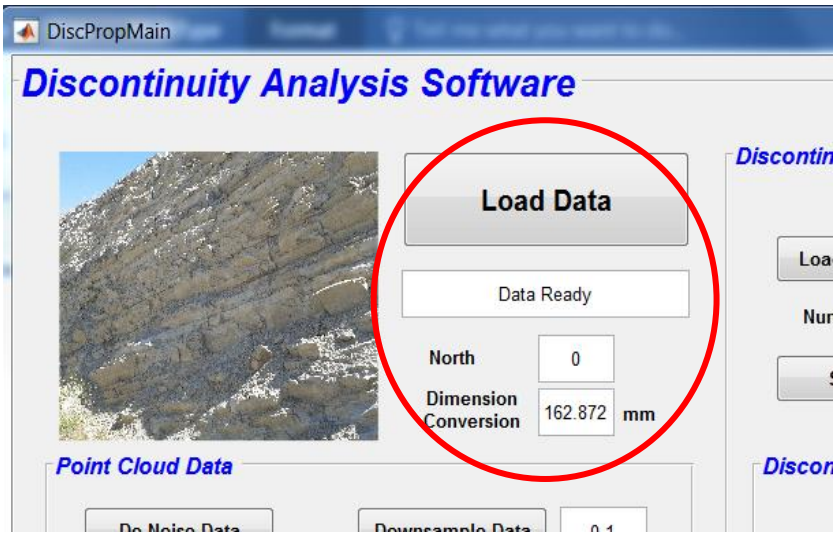

(a)

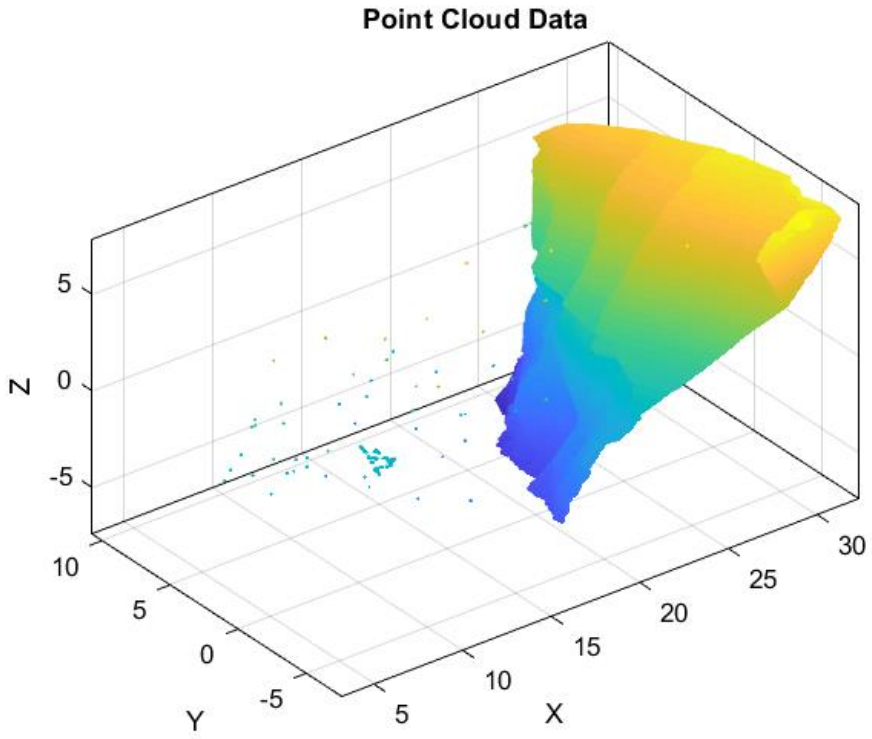

(b)

Figure 7.3. (a) Load Ply Data function and (b) ply data in display.

Once the point cloud data is loaded, additional information is provided by the program in the Point Cloud section below the Load Data section, Figure 7.4. The minimum and maximum values of X, Y, and Z axes are given and from there the dimensions of the data can be obtained. Using 'Dimension Conversion' the dimensions of the data can be found in millimeters as well.

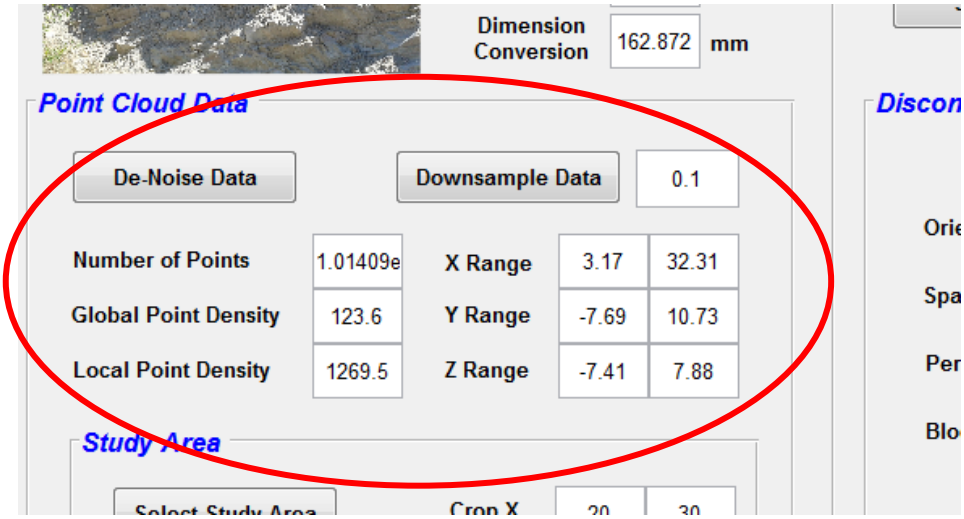

Figure 7.4. Information on point cloud data.

The number of 3D points (data) and global point density (points per unit volume) are also provided. Local point density is provided after selecting a study area. 'De-noise Data' and 'Downsample Data' functions were explained in Chapter 4. All information regarding the number of points and point density will change once either function is used.

'Select Study Area' gets minimum and maximum values entered on the GUI to crop the point cloud data loaded in the previous step. The cropping is done for X, Y, and Z dimensions separately, hence the dimensions of the data must be checked from the Point Cloud Data section to get the desired portion of the data accurately. The study area box will be displayed on the original point cloud data with red borders as seen in Figure 7.5(a). The cropped data is displayed on the full data in a pop-up window as shown in Figure 7.5(b). Once the study area is obtained, the Local Point Density value can be observed from the Point Cloud Data section.

The result can be saved as a .mat file using the 'Save Study Area' function. This is necessary as the next part of the GUI is requires study area data being loaded to function. It should be noted that selecting a study area is entirely optional. However, as can be seen, by the sample used in this case study, there are data points irrelevant to the study being conducted. These data increase the dimensions of the axes and drop the point density. Additionally, parts of the original data might be considered representative in terms of the discontinuity properties. Thus, determining a region of interest and selecting it as a study area is important.

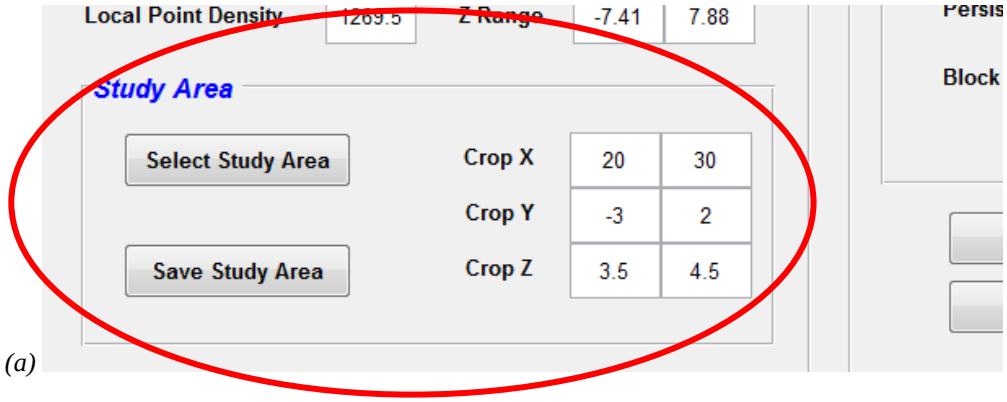

(a)

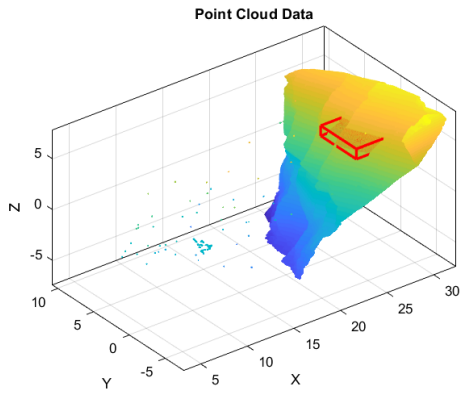

(b)

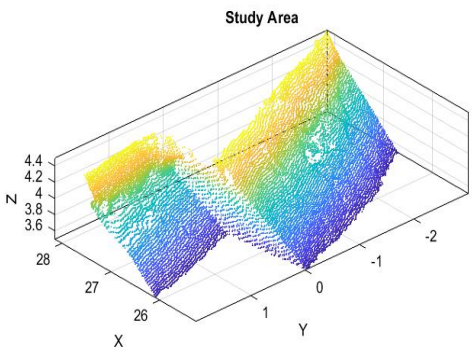

(c)

Figure 7.5. (a) Select the Study Area function in use. (b) Study area displayed on full point cloud data (c) Study area separated from full cloud data.

7.2 Discontinuity Set Detection

Once the region of interest is obtained as a study area, it can be loaded into the second stage of the Discontinuity Analysis GUI. 'Discontinuity Set Detection' section deals with finding and displaying discontinuity sets within the point cloud data of the rock surface, Figure 7.6. As shown in this figure, for the selected region of interest two discontinuity sets have been found. The point cloud data allows users to examine the 3D surface from different angles and thus determine discontinuity sets and planes visually. However, this study aims to accomplish this automatically without resorting to user interference and expertise. The easiest way to accomplish this is the use of the plane detection algorithms.

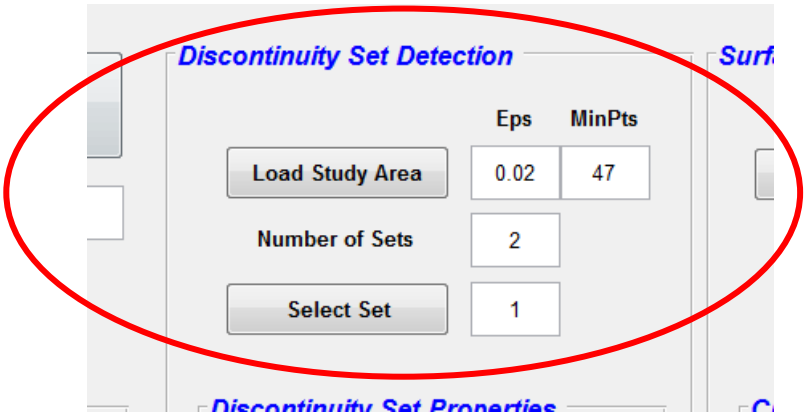

Figure 7.6. Discontinuity Set Detection section of the GUI.

Plane detection methods were discussed in detail in Chapter 5. Since discontinuity sets are a group of planes with similar orientations, it was concluded that the classification of each point was to be done according to their surface normals. DBSCAN was determined to be the most effective tool in this regard. The ε and MinPts for the case study were chosen as 0.02 and 47, respectively. 'Load Study Area' button is used to load .ply, .las, or .mat point cloud files and immediately applies DBSCAN on the data. Figures 7.7. and 7.8. show the resulting EGI and absolute EGI plots along with the dip and strike diagrams.

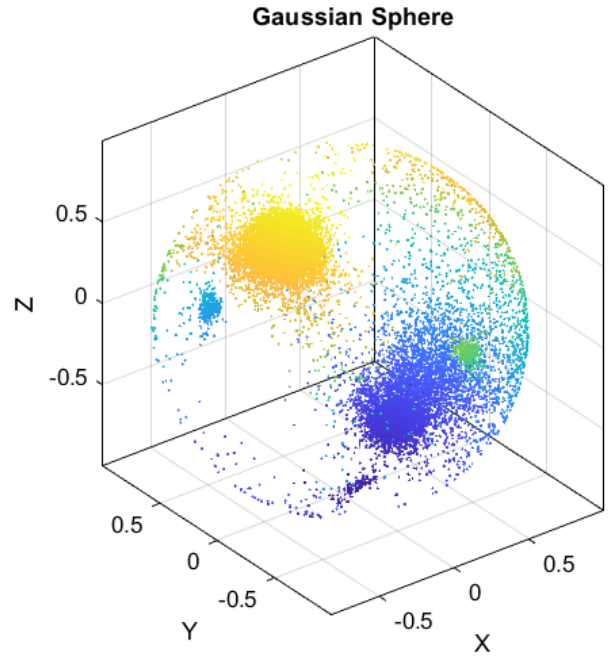

(a)

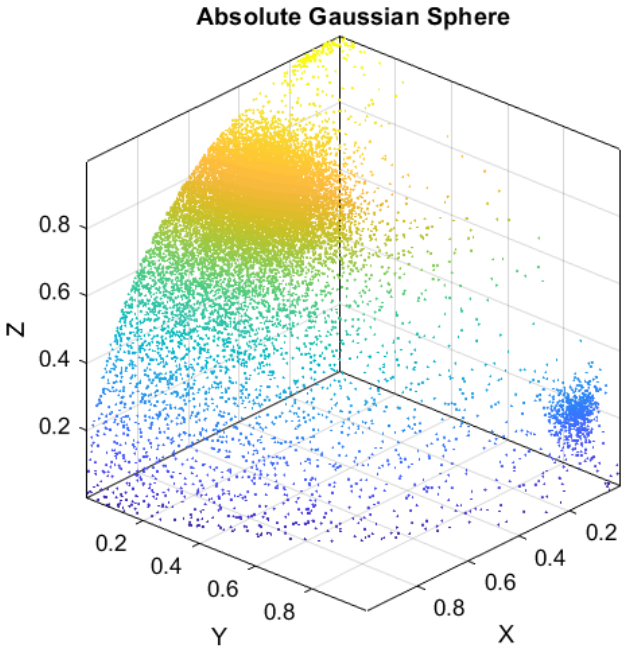

(b)

Figure 7.7. Generate Surface Normals function in use with (a) EGI and (b) absolute EGI.

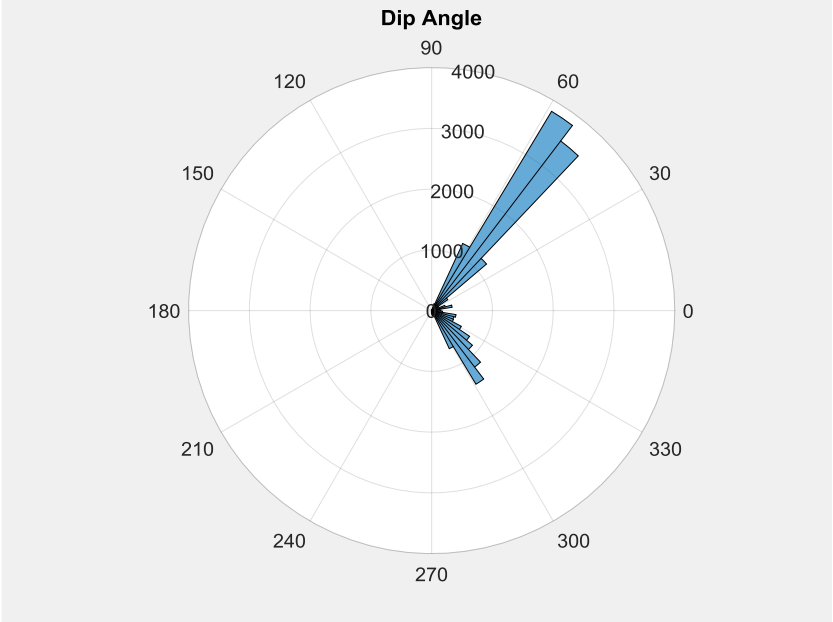

(a)

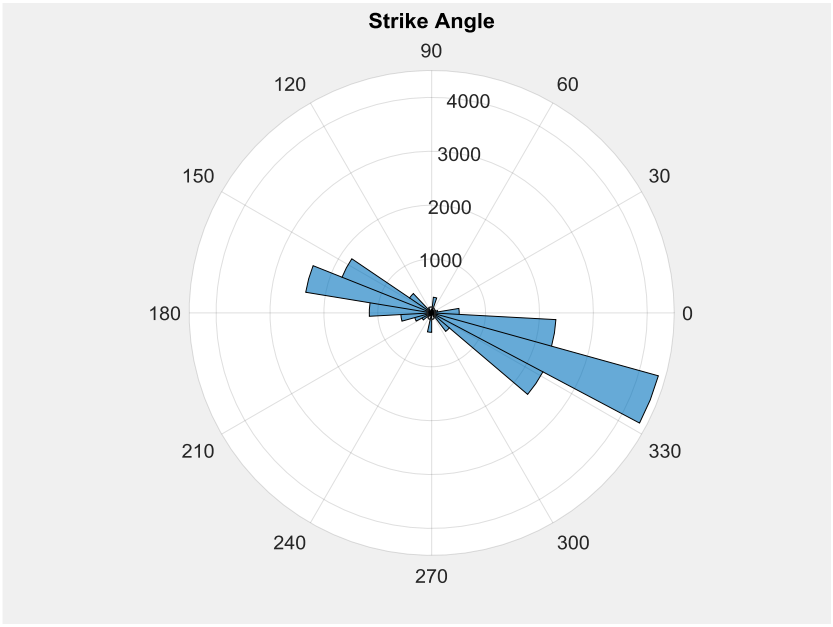

(b)

Figure 7.8. (a) Dip and (b) strike angles of surface normals.

In the study area used, two different discontinuity sets detected is shown in Figure 7.9. The points in the first set are colored in white while the second set is colored in green. It is seen that the first set has two surfaces (planes) and the second set has only one plane. As a result, only the first discontinuity set is capable of providing all discontinuity properties that the program can determine since properties like spacing and block size require two or more surfaces to be calculated.

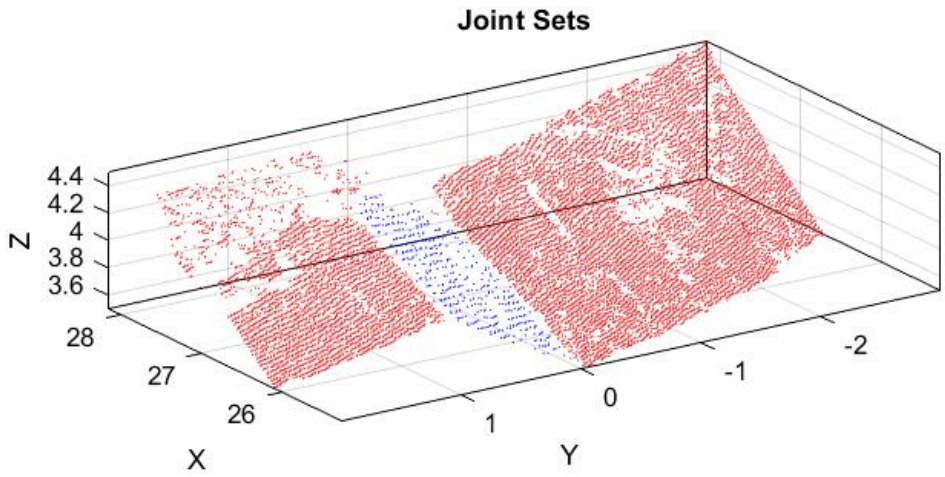

Figure 7.9. Discontinuity sets with case study region of interest.

The next step is to analyze a discontinuity set. The set number to be examined is to be entered next to the 'Select Set' button in Figure 7.6. Pressing the button will activate another DBSCAN to detect planes within the set, Figure 7.10. New Eps and MinPts values of 0.3 and 100 are used to detect the two planes within set one since a smaller area is examined now. Once the plane detection is completed the discontinuity properties are calculated automatically.

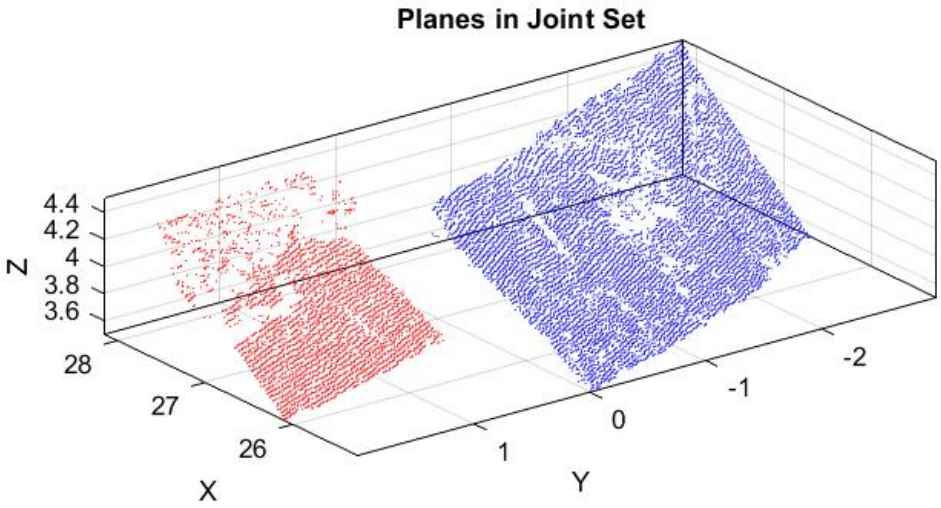

Figure 7.10. Planes within the first discontinuity set.

7.3 Discontinuity Set Properties

Orientation is calculated using the average surface normal of the plane. The angle between this unit vector and the azimuth (Y-axis by default) gives the strike angle. The angle between the normal and the horizontal plane (XY plane by default) yields the dip angle. The Matlab code is given below.

```
for i=1:m;
  data=C(:,:,i);
  data( ~any(data,2), : ) = [];
  pt=pointCloud(data);
  pt=pcdenoise(pt);
  data=[pt.Location(:,1),pt.Location(:,2),pt.Location(:,3)];
  eval(sprintf('Class%d = data',i));
  ClassName=sprintf('Class%d',i);
  assignin('base',ClassName,data);
  ClassName=evalin('base',ClassName);

  n=abs(pcnormals(pointCloud(ClassName)));
  n=mean(n);
```

```
  dip_angle=acosd(dot(n,hnorm));
        if dip_angle>90
            dip_angle=180-dip_angle;
        end
    DipAngle=sprintf('DipAngle%d',i);
    assignin('base',DipAngle,dip_angle);
    strike_angle=acosd(dot(n,vnorm));
        if strike_angle>90
            strike_angle=180-strike_angle;
        end
    StrikeAngle=sprintf('StrikeAngle%d',i);
    assignin('base',StrikeAngle,strike_angle);
end
```

Even though plane fitting method was discarded in Chapter 5 for use in discontinuity set detection, it is still useful in determining discontinuity spacing. Each plane (Class in the code) is fitted with a plane using Affine_fit function from which the plane equation belonging to the surface is extracted. Then the distance between the plane equation of one surface and the mean point of the next surface is calculated. This is repeated for each successive plane. The average spacing is then displayed as the spacing of the discontinuity set. The Matlab code is as follows.

```
IDX=evalin('base','IDX');
Clust=unique(IDX);
m=size(Clust,1);
for k=1:m
    ClassName=sprintf('Class%d',k);
    data=evalin('base',ClassName);
    [n,V,p]=affine_fit(data);

    eval(sprintf('n%d = n',k)); % find normal
    N=sprintf('n%d',k);
    assignin('base',N,n);

    eval(sprintf('p%d = p',k)); % find center point
    P=sprintf('p%d',k);
    assignin('base',P,p);

    d=-(n(1)*p(1)+n(2)*p(2)+n(3)*p(3));
    eval(sprintf('d%d = d',k));
    D=sprintf('d%d',k);
    assignin('base',D,d);
end
```

```
clc

DS=inf;
Distance=0;
for k=1:(m-1)
    N=sprintf('n%d',k);
    n=evalin('base',N);
    D=sprintf('d%d',k);
    d=evalin('base',D);

    for i=1:m
        if i~=k
           P=sprintf('p%d',i);
           p=evalin('base',P);

ds=abs(n(1)*p(1)+n(2)*p(2)+n(3)*p(3)+d)/sqrt(n(1)^2+n(2)^2+n(3)^2);

           if ds<DS
              DS=ds;
           end

           Spacing=sprintf('DS%d',k);
           assignin('base',Spacing,DS);
        end
    end

    Distance=Distance+DS;
    assignin('base','Distance',Distance);
end
clc
SP=str2num(get(handles.edit22,'string')); % Size of one pixel (mm)
Discontinuity_Spacing=(Distance*SP)/(m-1);
assignin('base','Discontinuity_Spacing',Discontinuity_Spacing);
set(handles.edit13,'String',sprintf('%.1f',Discontinuity_Spacing));
```

Persistence and block size are found together. Both of these properties can be very misleading as they only represent the region of interest. To accurately determine the persistence and block size of the whole rock mass, the user should select the study area well. Ideally, the discontinuity sets should be smaller than the region of interest to get proper results. Even after these caveats, finding persistence is still a tricky subject. In this case study, there are two discontinuity sets and the largest planes within each set are chosen to represent the persistence instead of the average distance.

The persistence of a set is found in this program by translating and rotating the plane of interest to the XY plane using Affine_fit. The center point of the fitted plane is translated to the origin (0,0,0), while a rotation matrix is used to rotate the fitted

plane to the horizontal plane. The surface data is translated and rotated along with the fitted plane. For the next step, the Z coordinates of the rotated plane are ignored. The boundary and the area of this new plane are found using the Matlab function 'boundary'. The corner points of the close-fitting rectangular region around the boundary are determined and the distances between them are calculated. The long side is the persistence of this set while the short side is the persistence of the second discontinuity set. Finally, the area of the largest plane is multiplied with the discontinuity spacing to find block size, Figure 7.11.

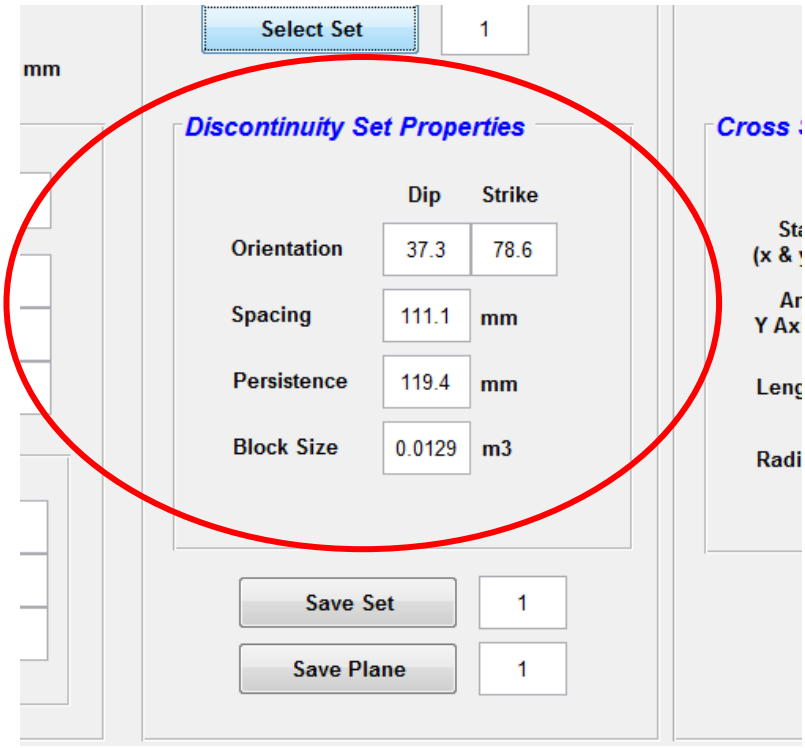

Figure 7.11. Discontinuity Set Properties section of the GUI with results from set one of the case study sample.

The Matlab code for finding persistence and block size is provided below.

```
for k=1:m
    ClassName=sprintf('Class%d',k); % loading surfaces for
translation
    data=evalin('base',ClassName);
    [S1,S2] = meshgrid([-1 0 1]);
    [n,V,p]=affine_fit(data); % plane fitting
    N=size(data,1);
    localz1=cross(data(100,:)-p, data(N,:)-p);
    unitz1=localz1/norm(localz1,2);
    localx1=data(100,:)-p;
    unitx1=localx1/norm(localx1,2);
    localy1=cross(localz1, localx1);
    unity1=localy1/norm(localy1,2);
    T1=[unitx1(:), unity1(:), unitz1(:), p(:); 0 0 0 1];
    C1=[data,ones(N,1)];
    data_new=T1\C1';
    area3d=data_new(1:3,:)'; % surface translated and rotated onto
xy plane
    area=[area3d(:,1),area3d(:,2)]; % remove z axis to obtain 2d
surface
    [b,A]=boundary(area(:,1),area(:,2)); % determine boundary and
area
    SP=str2num(get(handles.edit22,'string'));
    Area(k)=A*(SP^2); % surface area of plane within joint set
    [q1,r1]=min(area(:,2));
    [q2,r2]=min(area(:,1));
    [q3,r3]=max(area(:,1));
    [q4,r4]=max(area(:,2));
    corner1=area(r1,:); % corner point at min Y value
    corner2=area(r2,:); % corner point at min X value
    corner3=area(r3,:); % corner point at max X value
    corner4=area(r4,:); % corner point at max Y value
    cr1=[corner1(:,1),corner1(:,2);corner2(:,1),corner2(:,2)];
    Side1(k)=pdist(cr1,'euclidean'); % length of side connecting
corner 1&2
    cr2=[corner1(:,1),corner1(:,2);corner3(:,1),corner3(:,2)];
    Side2(k)=pdist(cr2,'euclidean'); % length of side connecting
corner 1&3
end
persist1=mean(Side1)*SP; % average persistence in one direction
(mm)
persist2=mean(Side2)*SP; % average persistence in perpendicular
direction (mm)
assignin('base','persist1',persist1);
assignin('base','persist2',persist2);
set(handles.edit15,'String',sprintf('%.1f',persist1)); % display
average persistence of joint set

BlockSize=mean(Area)*Discontinuity_Spacing/(10^9); % average block
volume (m^3)
assignin('base','BlockSize',BlockSize);
set(handles.edit16,'String',sprintf('%.4f',BlockSize)); % display
block size
```

As stated earlier, these properties are accurate only in carefully selected study areas. Even though the process is automatic, poor selection of a region of interest or poor data will result in erroneous discontinuity properties. Once the analysis is complete, each discontinuity set can be saved in .mat files. The number of the set should be entered next to the ‘Save Set’ button. Similarly, planes within a set can be saved individually with the ‘Save Plane’ button. The next step will involve a roughness analysis on a single plane.

7.4 Surface Roughness

The final section of the GUI’s main window is Surface Roughness (Figure 7.12), in which surface profiles are obtained from cross-sections on the rock surface point cloud data. Similar to the Discontinuity Set Detection section, Surface Roughness can work independently from the other two sections provided that preprocessed data is available. The ‘Load Surface’ button is used to load .ply, .las, and .mat point cloud files. The program fits a plane to the data using the Affine_fit function in order to translate the mean point of the data to the origin and rotate the fitted plane along with the data onto the XY plane, Figure 7.13.

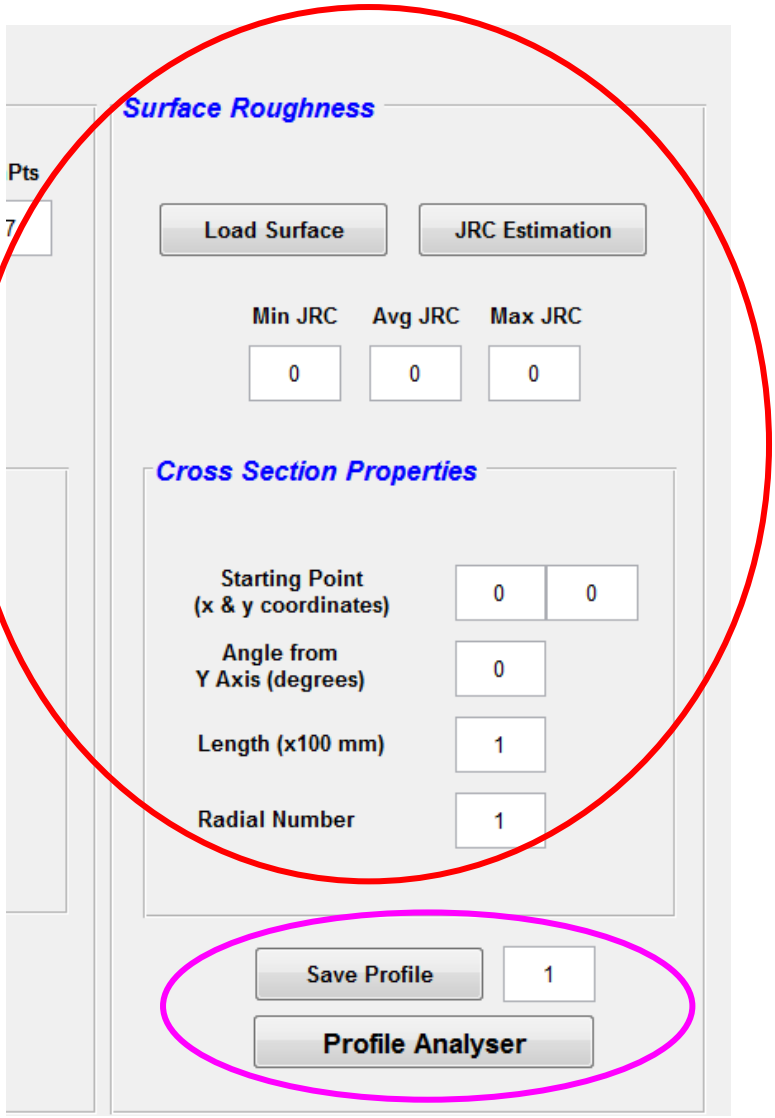

Figure 7.12. Surface Roughness section of Discontinuity Analysis GUI.

The Matlab code is given below.

```
%-----------------------
% Load Point Cloud & Translate to X-Y Plane
%-----------------------
[fileload,pathload,FilterIndex]=uigetfile({'*.mat';'*.las';'*.ply';
'*.*'},'Load Surface','samples\');
if isequal(fileload,0)
    return
else
    CurrentDataFileName=[pathload,fileload];
    [filepath,name,ext]=fileparts(CurrentDataFileName);
    if ext=='.las'
        obj=lasdata(CurrentDataFileName);
        X=obj.x;
        Y=obj.y;
        Z=obj.z;
        obj=[X,Y,Z];
    end
    if ext=='.ply'
        obj=pcread(CurrentDataFileName);
        X=obj.Location(:,1);
        Y=obj.Location(:,2);
        Z=obj.Location(:,3);
        obj=[X,Y,Z];
    end
    if ext=='.mat'
        obj=load(CurrentDataFileName);
        obj=cell2mat(struct2cell(obj));
    end
end
assignin('base','obj',obj);
%-----------------------
[S1,S2] = meshgrid([-1 0 1]);
[n,V,p]=affine_fit(obj);
N=size(obj,1);
localz1=cross(obj(100,:)-p, obj(5000,:)-p);
unitz1=localz1/norm(localz1,2);
localx1=obj(100,:)-p;
unitx1=localx1/norm(localx1,2);
localy1=cross(localz1, localx1);
unity1=localy1/norm(localy1,2);
T1=[unitx1(:),unity1(:),unitz1(:),p(:); 0 0 0 1];
C1=[obj,ones(N,1)];
obj_new=T1\C1';
obj_new= obj_new(1:3,:)';
assignin('base','obj_new',obj_new);

figure(9), pcshow(obj_new);
title('Surface Plane Translated to X-Y Plane');
xlabel('X');
ylabel('Y');
zlabel('Z');
```

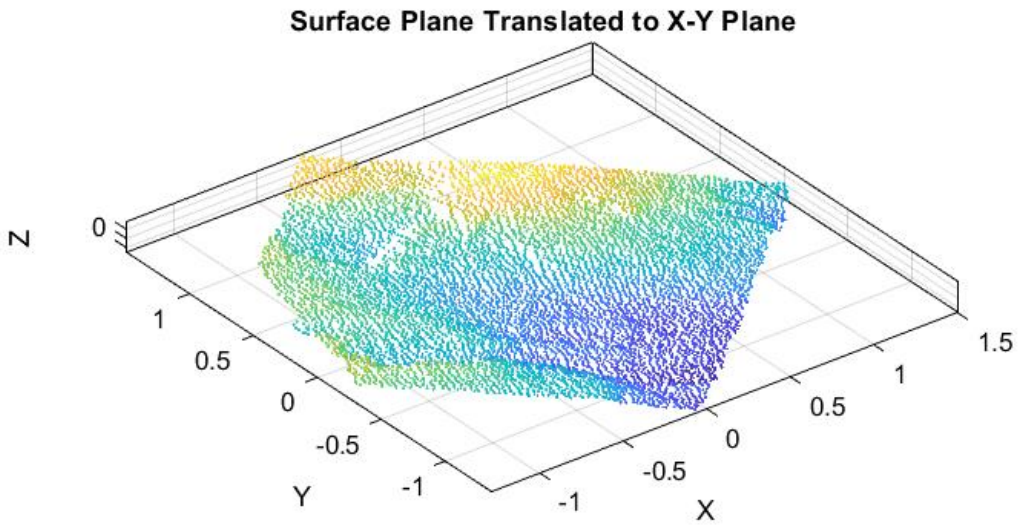

Figure 7.13. Translation and rotation of loaded point cloud data.

The next step is the 'JRC Estimation' button. To be able to accomplish the estimation of JRC, first, the cross-section properties must be established, Figure 7.14. The program allows the user to draw a cross-section anywhere on the surface data. The cross-section generation starts from an origin point on the XY plane determined by the user in which the default point is (0,0). Users can start the cross-section from anywhere on the surface as long as it is within the dimensions of the data. From there the program draws a cross-section towards a direction determined by the user in which Y-axis is the default direction. Users can enter the angle from Y-axis to set the direction of the cross-section. Figure 7.14. shows two cross-sections with the default and altered origin (-0.5,-0.5) and direction (180) values.

It should be noted that each cross-section is 100 mm in length in accordance with the value entered in Dimension Conversion explained in Subsection 7.2. This cross-section length is enforced to match JRC profile templates in order to avoid resampling cross-sections or the template profiles. The length of cross-sections can be increased by user input, but it will always be multiplications of 100 mm and every 100 mm segment of this larger cross-section will be subject to JRC estimation individually.

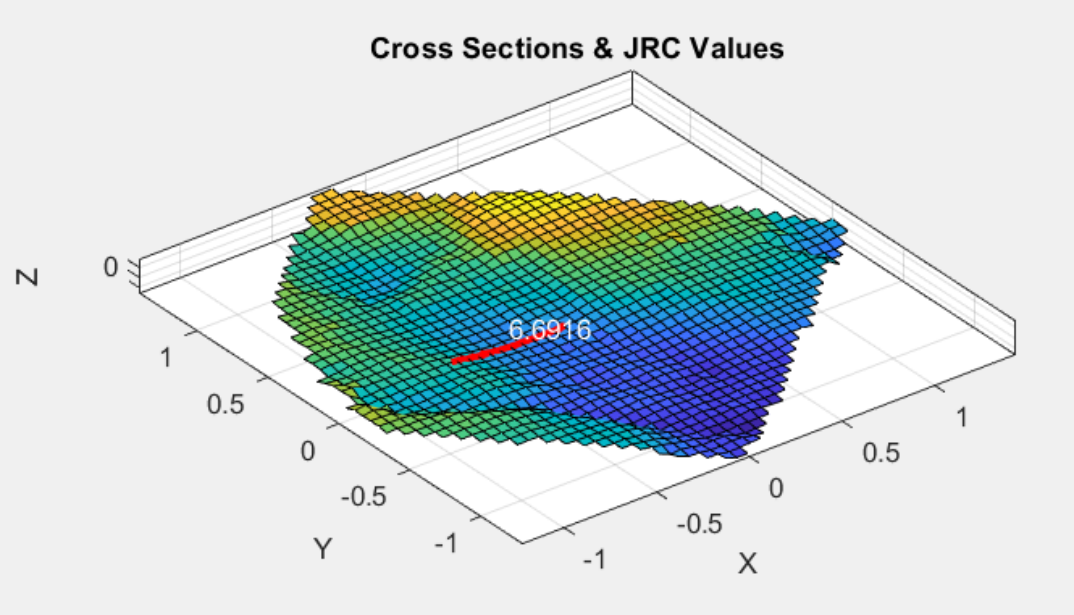

(a)

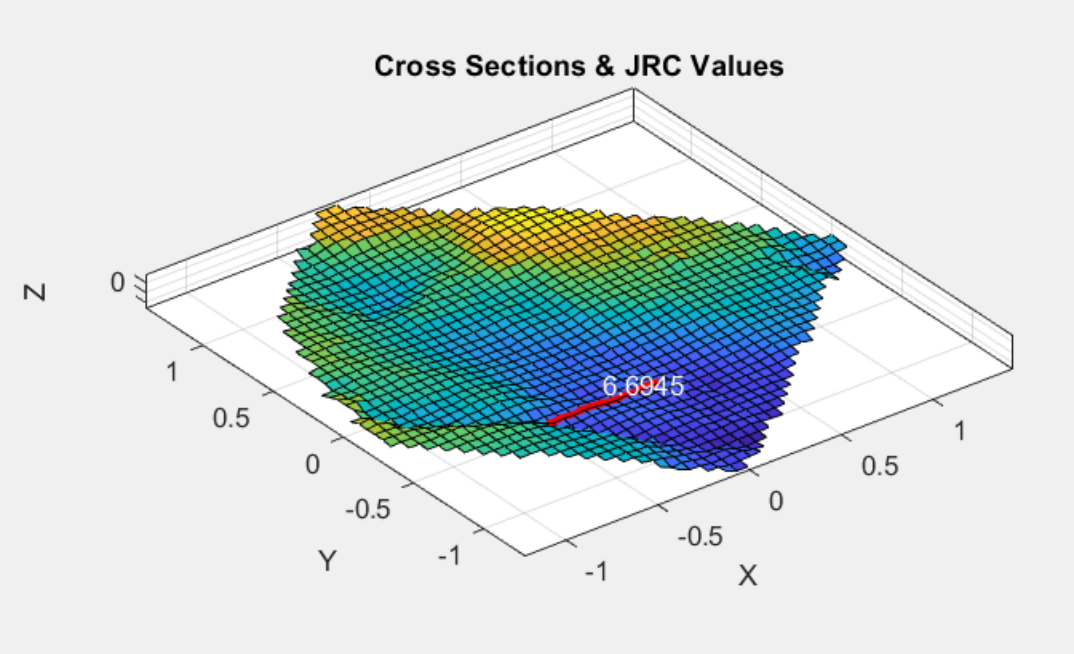

(b)

Figure 7.14. (a) Cross-section with default origin (0,0) and direction (0) values. (b) Cross-section with altered origin (-0.5,-0.5) and direction (180) values.

Another feature in this program is the generation of cross-sections radially around the origin point. This allows the generation of multiple cross-sections from which the JRC of the surface, not just a single line, can be better estimated. The number of cross-sections within the radial setup only needs to divide 360^0 without any fraction. It should be noted that increasing the number of cross-sections to be generated will increase stress on processing.

After generating the cross-sections, the 10 template profiles for JRC from Barton and Choubey (1977) are loaded automatically. The process for JRC estimation that follows has been discussed in Chapter 6 in detail. During this process, each cross-section is duplicated. The base cross-section is reserved for plotting on the point cloud surface for visual purposes. The duplicate cross-section is de-trended and is used as a sample profile in the JRC estimation process. De-trending is vital in this process since the profiles obtained from cross-sections may have wildly different JRC values depending on the slope of the point cloud data. For this case study, six cross-sections were generated for the default origin, direction, and length, Figure 7.15.

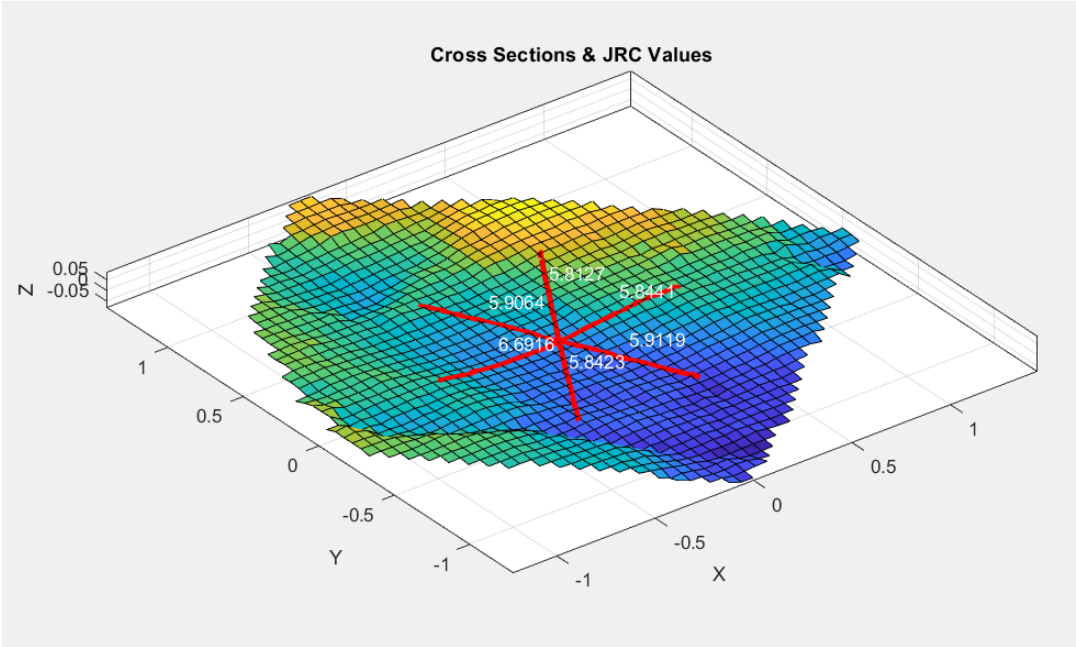

Figure 7.15. Six radial cross-sections around (0,0) with their JRC values.

Once JRC values are obtained for each profile, the minimum, average, and maximum JRC values are displayed on GUI, Figure 7.16. Individual JRC values are shown on the pop-up figure, Figure 7.15., as well. From these results, one can determine the direction of slip and overall roughness of the surface. It is advised to use roughness analysis on surface data with high point density in order to get the most accurate results. Finally, each profile generated from cross-sections can be saved individually for the final section in which the profile roughness in detail.

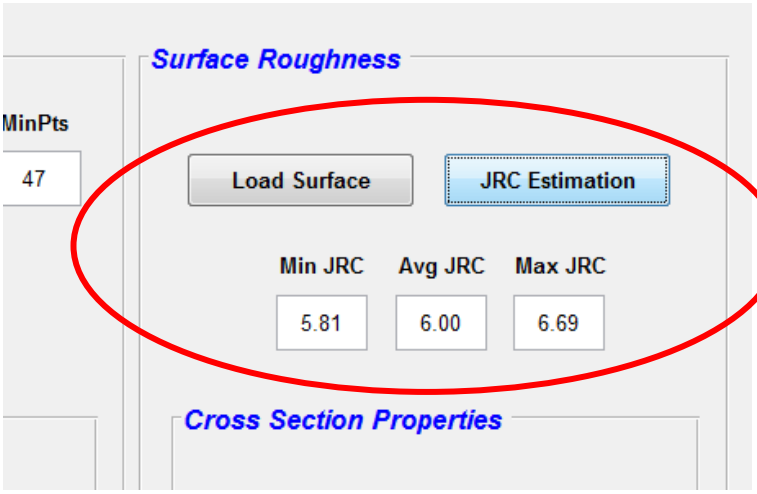

Figure 7.16. Result of JRC estimation for six cross-sections.

7.5 Profile Analyzer

At the bottom of the Surface Roughness section in the main GUI window is the 'Profile Analyzer' button, Figure 7.12. Pressing it will open a new GUI as shown in Figure 7.17. This GUI can be used independently to determine the JRC of the surface profiles by loaded when the 'Load Sample Profile Button'. While Profile Analyzer GUI is an optional part of the Discontinuity Analysis software, it is still an important component for analyzing surface profiles for JRC estimation in detail. Profile Analyzer was the software developed to apply the novel JRC estimation using PSD, explained in Chapter 6. Unlike the main program, this GUI can only analyze 2D surface profiles.

On the left side of the GUI, the 10 reference (template) JRC surface profiles from Barton and Choubey (1977) are displayed, in case the user wishes to make a visual comparison. On the right-hand side of the GUI are three windows. The first window is for the sample profile, the second window is for the template profile to which the sample is compared to, and the final window displays the PSD and the line fit for both sample and template profiles.

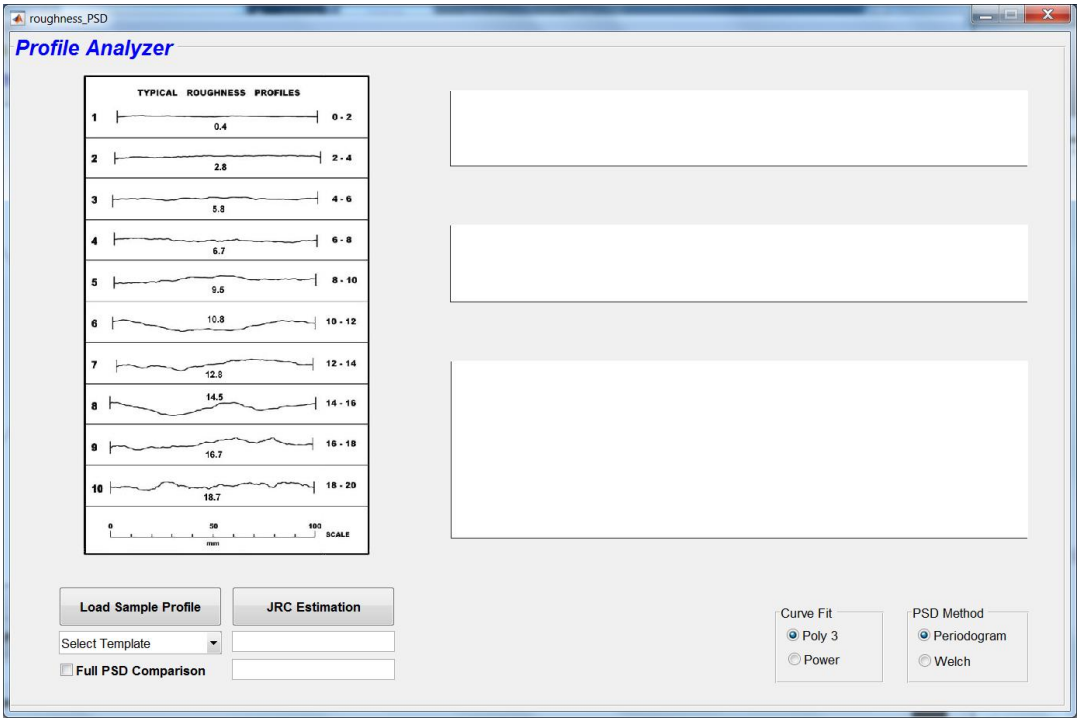

Figure 7.17. Profile Analyzer GUI.

The ‘Load Sample Profile’ button is used to load any surface profile in .mat format. These profiles are simple arrays of X-Y coordinates. The program will not accept any other file format for analysis. Once the sample profile is loaded, it will be plotted in the top window on the right, Figure 7.18. The sample profile used in this case study is obtained from the earlier Subsection 7.5., which is obtained from the cross-section with default origin, direction, and length. The JRC value was then estimated to be 6.69.

The next step is pressing the ‘JRC Estimation’ button, which will initiate the process that was explained in detail in Chapter 6. Unlike the Surface Roughness section, Profile Analyzer allows users to change the method of PSD and Curve Fit. Periodogram was found to be overall the superior option to Welch, but users can still activate the Welch method to see its results. Similarly, users can choose the power curve fit instead of the 3rd-degree polynomial. It should be noted that power fit puts additional strain on processing.

Once the JRC estimation is completed, the second window from the top on the right side of the GUI will display the template profile that the sample matches. The text box under the ‘JRC Estimation’ button will give the JRC range, while the second text box will give the interpolated JRC value for the sample profile. The third window from the top on the right side of the GUI will display the PSDs and curve fits of both sample and template profiles. In all plots in this GUI, anything related to the sample profile is colored green and anything related to the template profile is colored red with varying line thickness. All of these can be observed in Figure 7.18.

If the ‘Full PSD Comparison’ box is checked, a pop-up window will display the comparison of the sample profile’s PSD fit against all 10 template profiles’ PSD fits, Figure 7.19. The area difference between curves is provided in each sub-plot of the window for examination. It should be noted that visual comparison can be deceptive as the calculation of the area difference between the sample and template PSD fits may have positive and negative value ranges when the curves intersect.

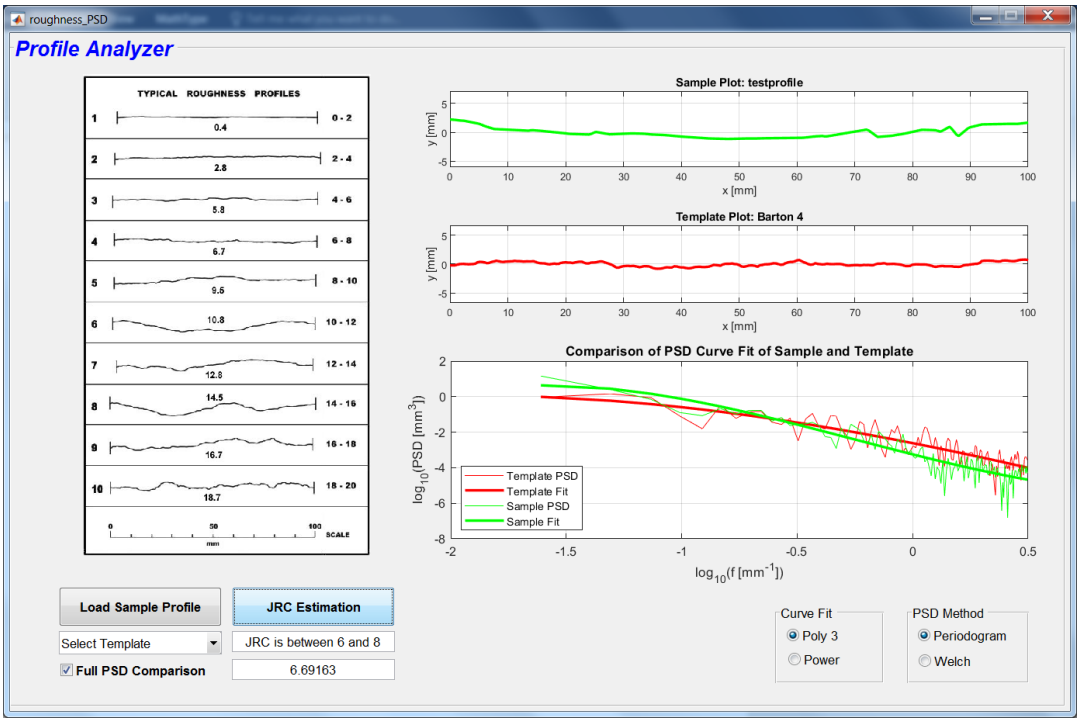

Figure 7.18. Sample profile obtained from the Surface Roughness section.

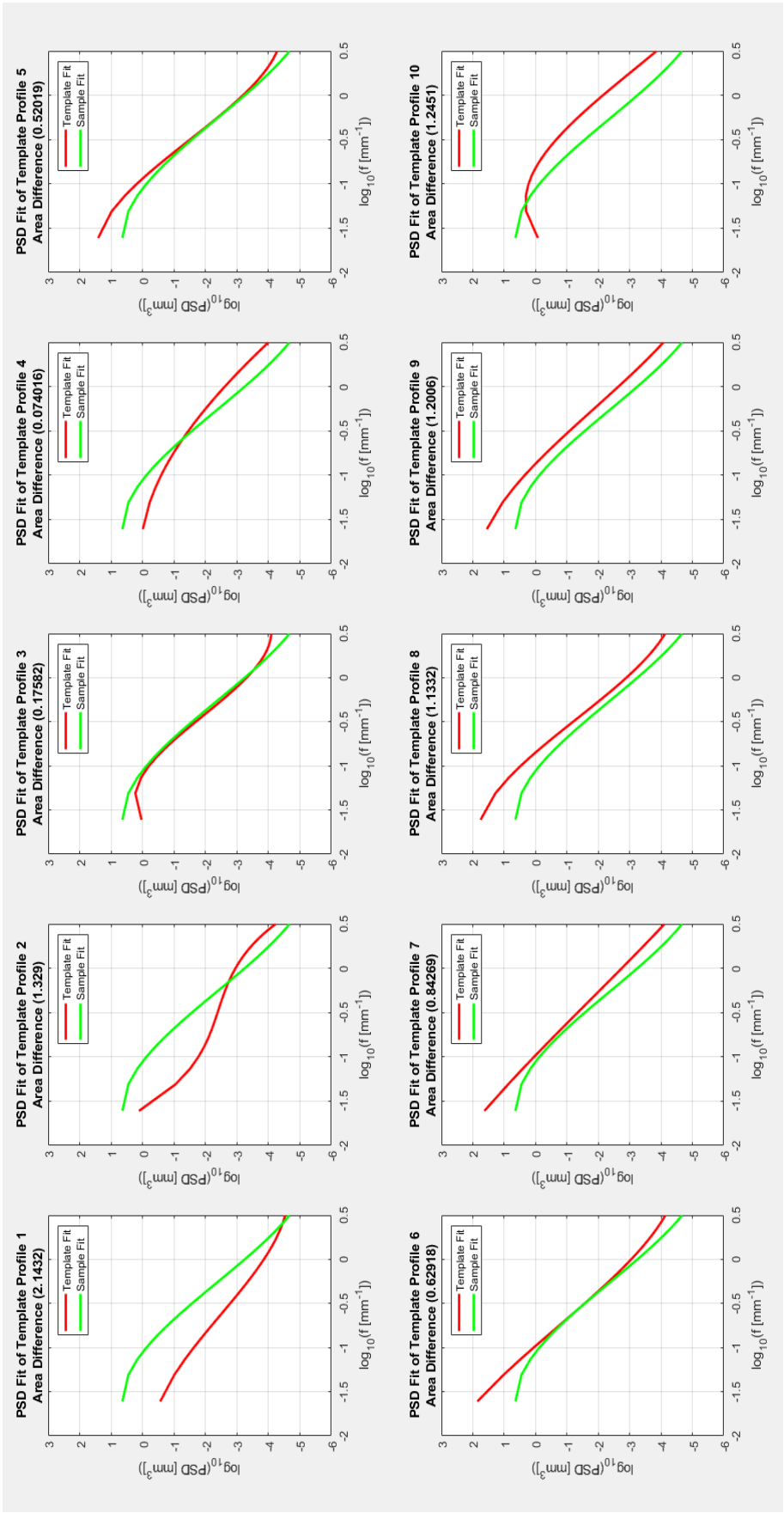

Figure 7.19. Full comparison of the sample profile and all 10 template profiles

CHAPTER 8

APPLICATION OF AREAL JRC ESTIMATION TO CASE AREAS

8.1 Areal JRC Estimation

In this section, the novel method for estimating JRC will be extended to apply to a surface area. Certain parts of the rock outcrop represented by the point cloud data of Riquelme (2014) are used for this purpose. As stated in earlier chapters, the rock outcrop dimension is 3x3 meters (x & y) and as a result, the unit distance corresponds to 162.78 mm. The rock outcrop has two distinct joint sets. The first set has three clear surfaces, while the second set has two clear and one fractured surfaces, as seen in Figure 8.1. The bottom half, beneath Z=1, is unsuitable for JRC estimation because of the significant irregularities formed by fracturing and weathering. It should be noted that there are numerous areas in the upper half deemed suitable for JRC estimation that is also fractured. These small areas will be isolated and removed during the case study.

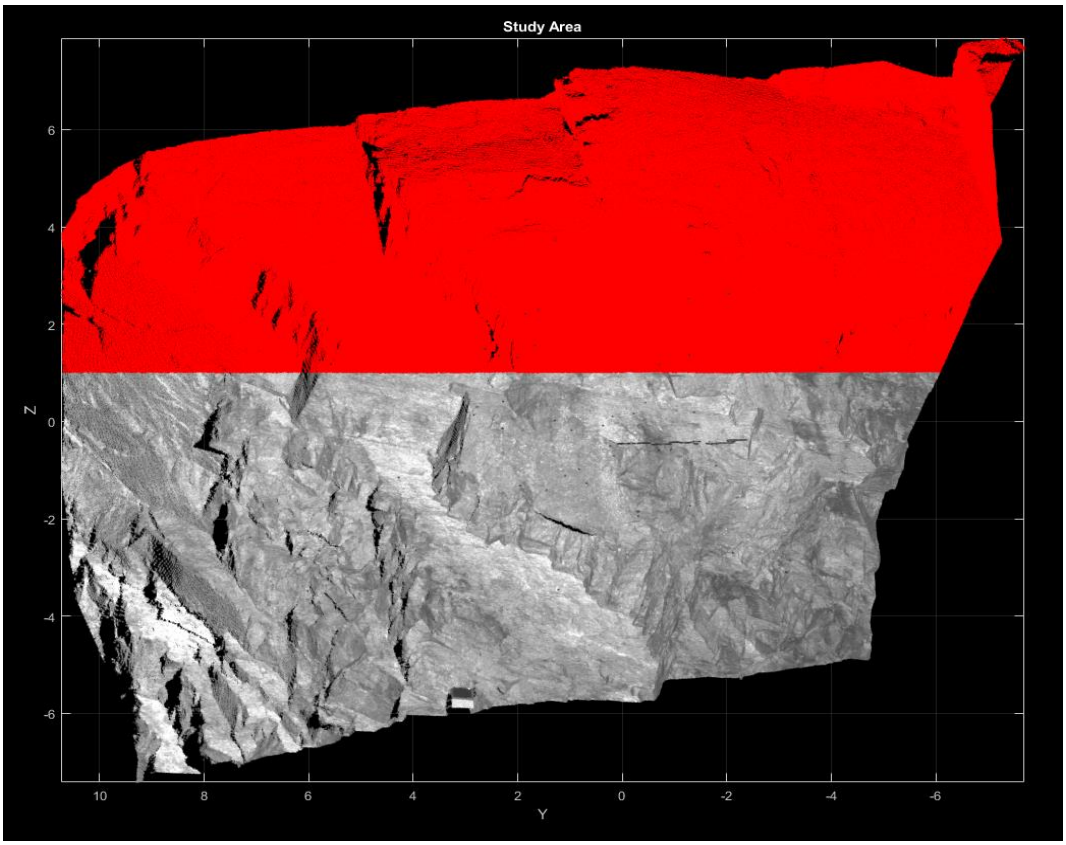

Figure 8.1. Region (red) was selected for JRC estimation.

Discontinuity Analysis Software was used to determine the joint sets, as explained in Chapter 7. Since the amount of data was too large for the operation, the data was divided into boxes of the size of [10,10,1] as seen in Figure 8.2. These individual boxes were classified to find the joint sets. Point cloud data that didn't belong to any major joint set (the two main joint sets) were classified as Class 0 and were removed. Next, the point cloud data that had similar orientations were combined to form the joint sets.

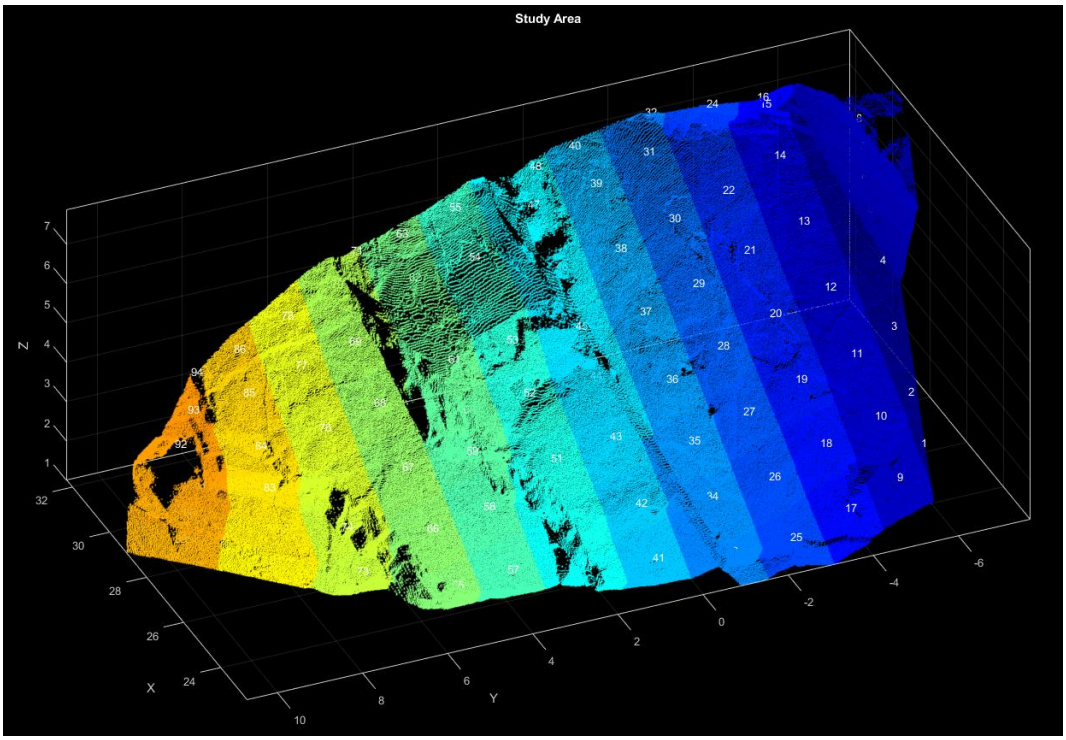

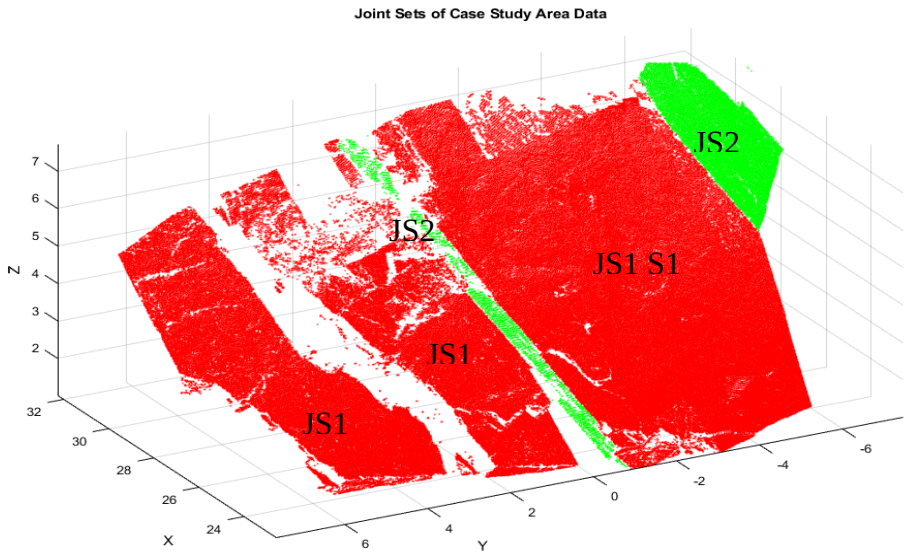

Figure 8.2. Data divided into boxes for classification and the results displaying the joint sets.

The discontinuity sets in Figure 8.2. are Joint Set 1 (red) and Joint Set 2 (green). Joint Set 1 has three planar surfaces, namely Surface 1, Surface 2, and Surface 3 from right to left, respectively. Joint Set 2 has two planar surfaces, named Surface 1 and Surface 2 from right to left, respectively. The potential third surface for the second joint set was found to be too irregular for JRC estimation. Joint Set 2 Surface 2 also has its irregularities and lack of point cloud data in certain areas. However, this surface was kept in the case study to display the shortcomings of such poor data when estimating JRC.

Joint Set 1 Surface 1 will be used to describe the process of the application of the novel JRC estimation method for three-dimensional surfaces. For this purpose, the circular JRC estimation introduced in Chapter 7 is used. In the first step, the data of Joint Set 1 Surface 1 is fitted with a plane using the 'Affine_fit' function. This fitted plane is then rotated and translated onto the XY plane with its center point matching the origin. The point cloud data is rotated and translated the same way as the fitted plane.

The next step is creating a grid, shown in Figure 8.3(a), for the centers of the JRC estimation circles. The grid dimension is 5 cm on both x and y axes. The grid placed on the XY plane is then cropped so that all JRC circles and their profiles have values. The surface chosen from the first joint set had 636 grid points as shown in Figure 8.3(b). Each JRC estimation area will be defined by four 10 cm long profiles with the center of the circle coinciding with the midpoint of the profiles as seen in Figure 8.4. Thus, these profiles define circles with a 5 cm radius. As the circles are moved along and across the grid, they will overlap by 5 cm in the cardinal directions.

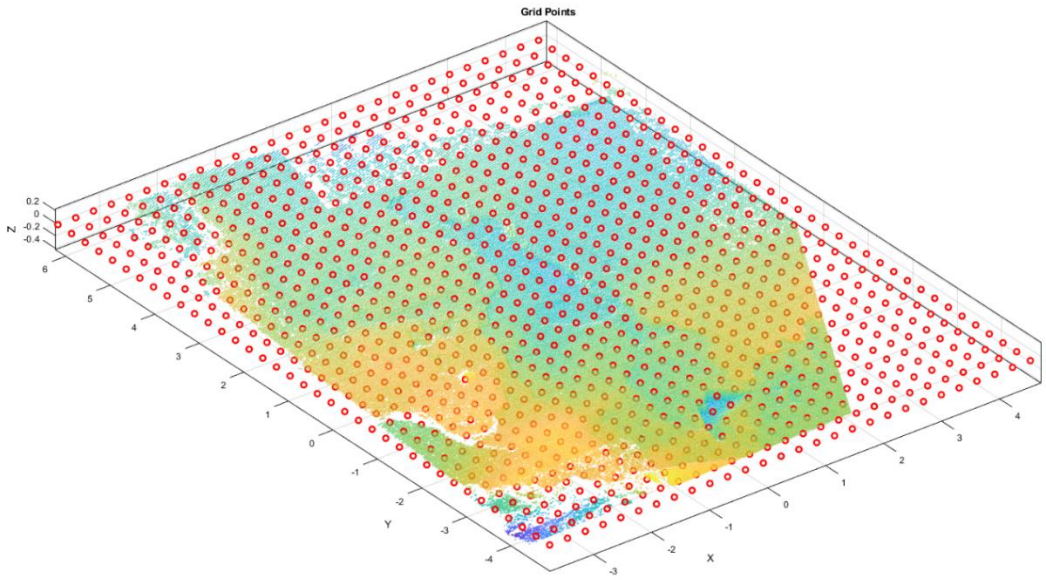

(a)

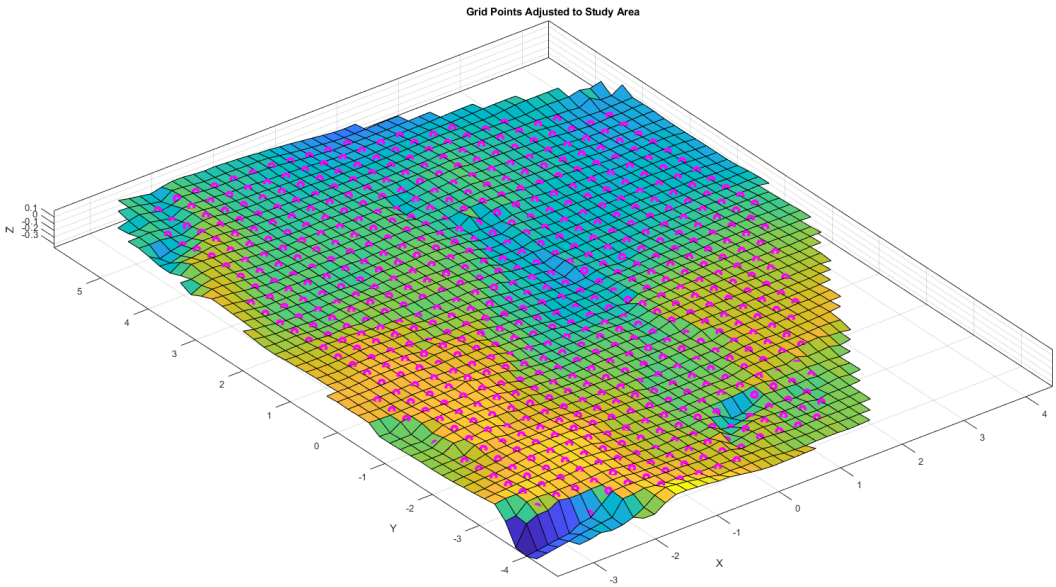

(b)

Figure 8.3. Grid points and their adjustment to the study area.

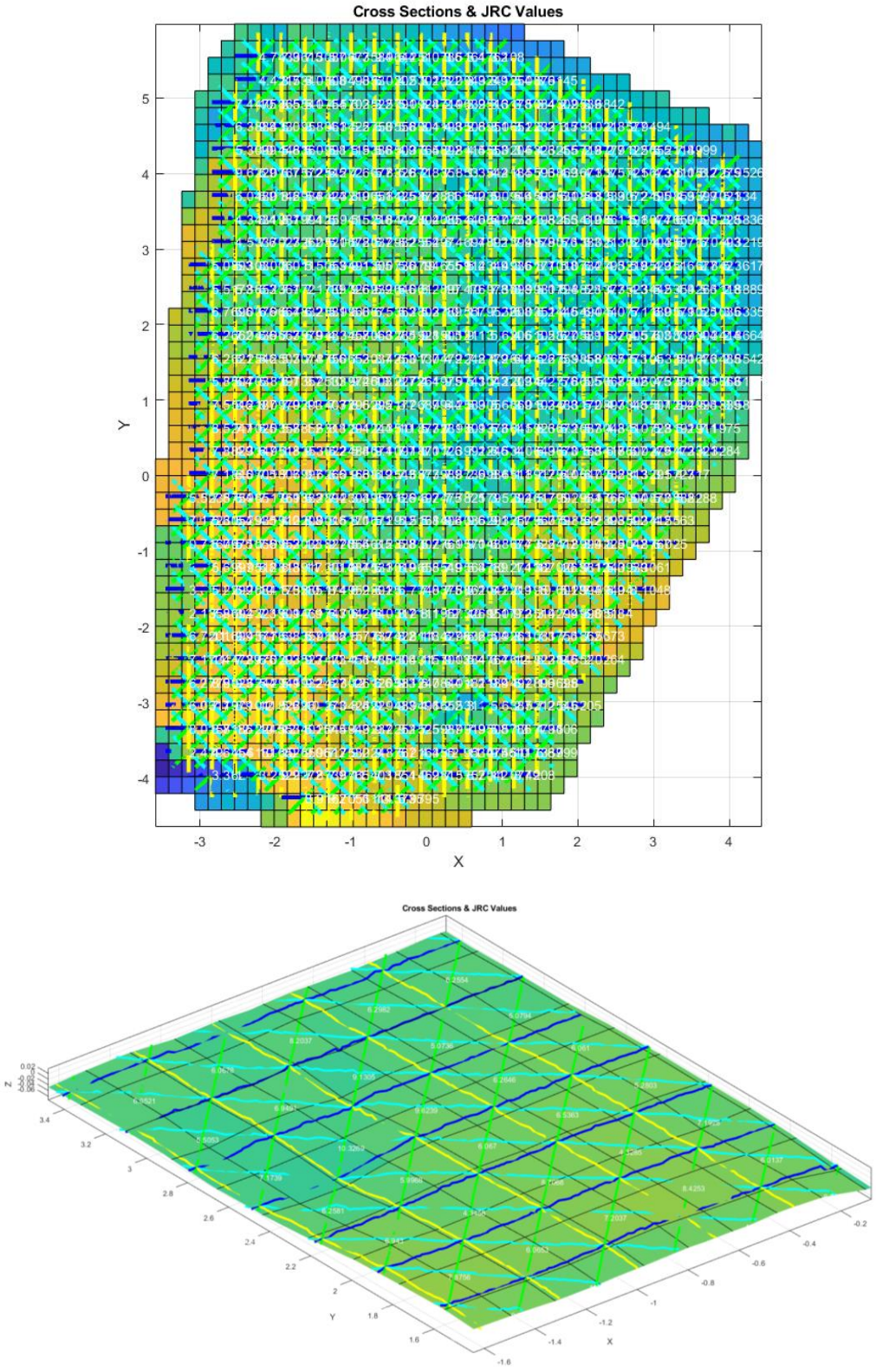

Figure 8.4. JRC estimation areas of the whole study area and a close-up of a section.

The JRC of each circular area is the average JRC of the four profiles in that area. Once the JRC values over every grid point are obtained, a JRC map is produced to show the variation of the JRC across the discontinuity surface. Figure 8.5. shows that the JRC map is consistent with the point cloud data as more jagged areas have higher JRC, while areas lacking data have JRC values close to zero. In this discontinuity surface, the minimum, maximum, and average JRC values estimated are respectively; 0.71, 13.78, and 6.35.

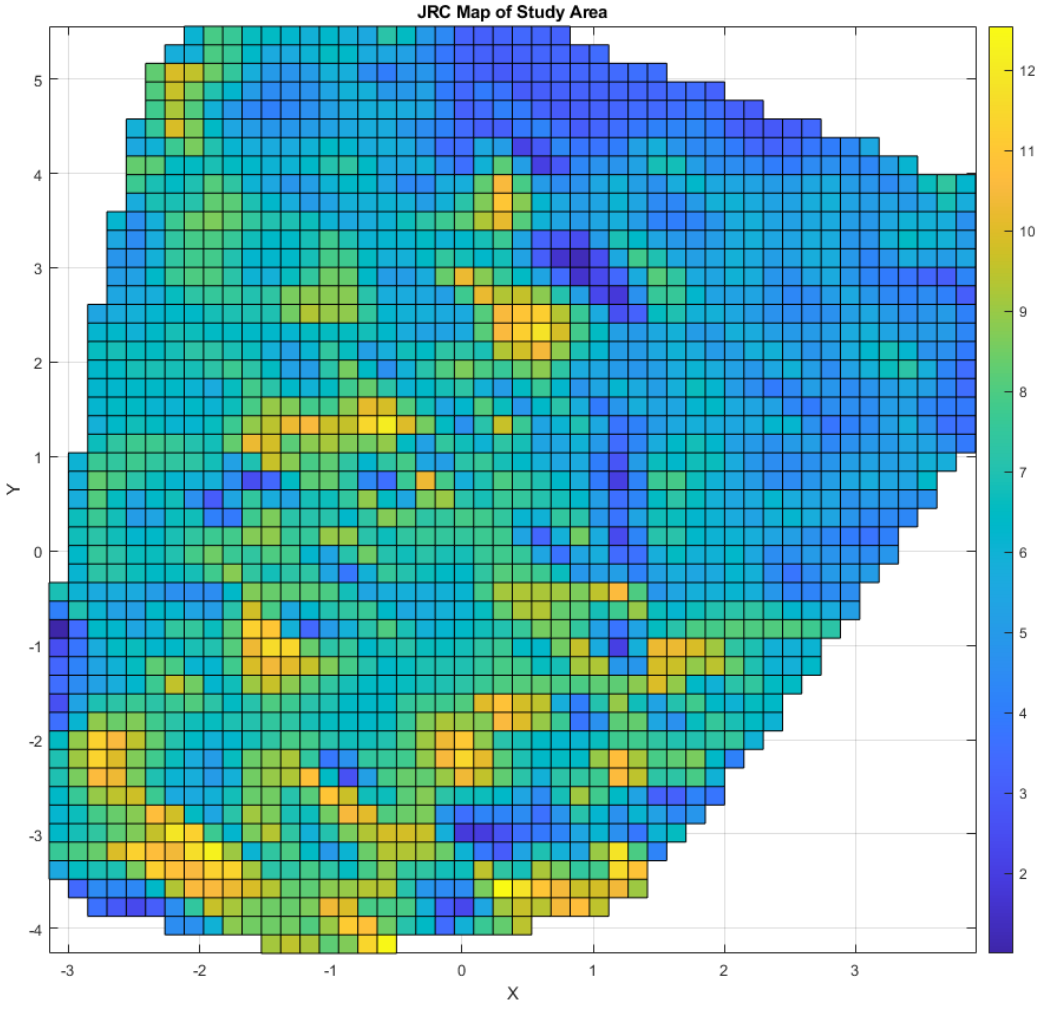

Figure 8.5. JRC map of Joint Set 1 Surface 1.

From these results, it could be said that this discontinuity surface may be represented by a JRC value of 6.35. However, it should be noted that localized missing and distorted data on the surface can affect the results. Figure 8.6. displays the distribution of JRC values within Barton's reference profiles. Outlier JRC results can be on both ends, especially at higher JRC values. As a result, the few extreme JRC values should be removed before calculating the average JRC for the surface. Statistical significance level α=0.05 is applied to the JRC values obtained from the study surface. The results can be seen in Figure 8.6. and be compared to the original distribution of JRC values.

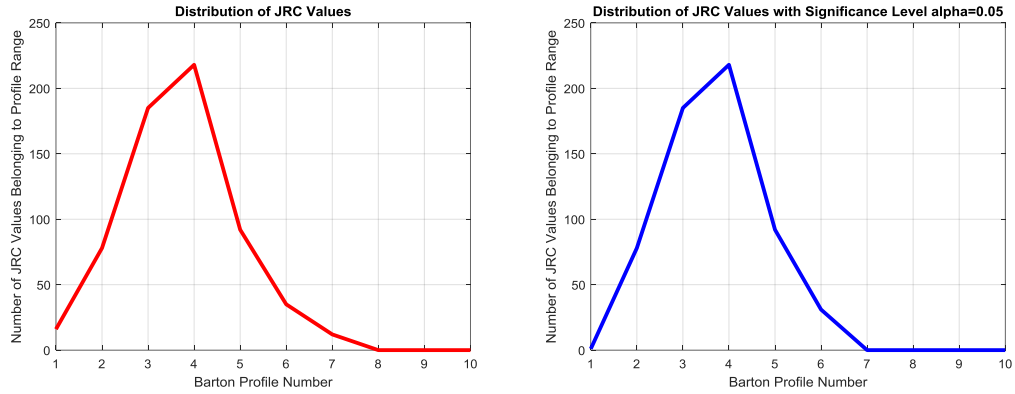

Figure 8.6. Distribution of JRC values of study area according to reference profiles of Barton and Choubey (1977) and same data for significance level α=0.05.

The mean JRC of the new distribution is 6.32, which indicates that outliers do not influence the result of the analysis significantly for this particular exercise. It can be concluded that removing outliers is optional when trying to determine the JRC of a surface. However, it should be noted that this will depend on the number of JRC values obtained from a surface. The less the number of JRC data, the more likely outliers will influence the average JRC of the surface. On the question of whether these outliers are important or not, it should be noted that each outlier represents the mean JRC of a circular area on a surface with a 5 cm radius. Thus, the removal of outliers should be considered according to the size of the area of the discontinuity surface.

The process explained for the Joint set 1 Surface 1 is applied to the rest of the case study surfaces; Joint Set 1 Surface 2, Joint Set 1 Surface 3, Joint Set 2 Surface 1, and Joint Set 2 Surface 2. The process and the resulting JRC maps can be seen in Figures 8.7. to 8.10.

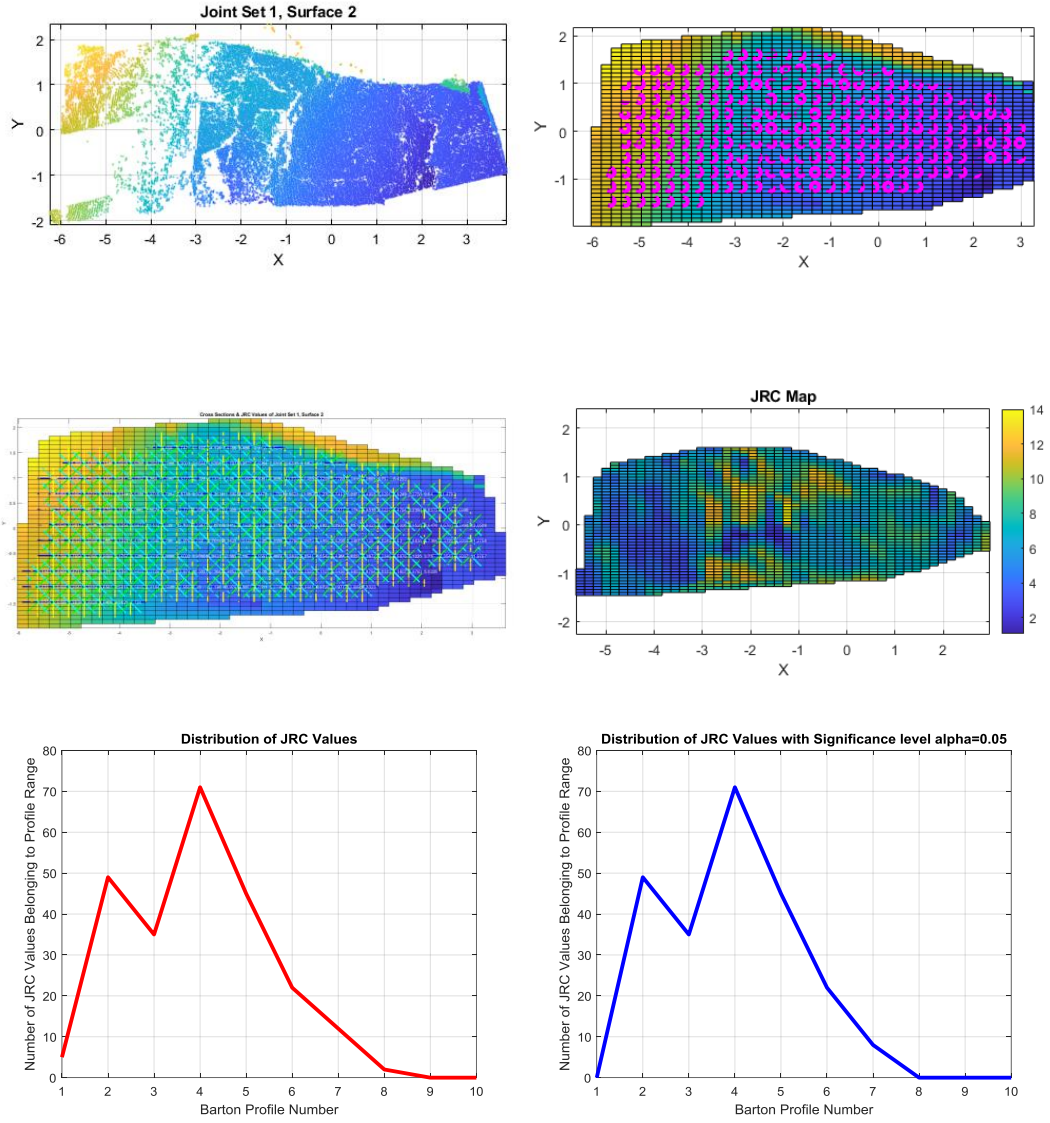

Figure 8.7. JRC estimation process of Joint Set 1, Surface 2.

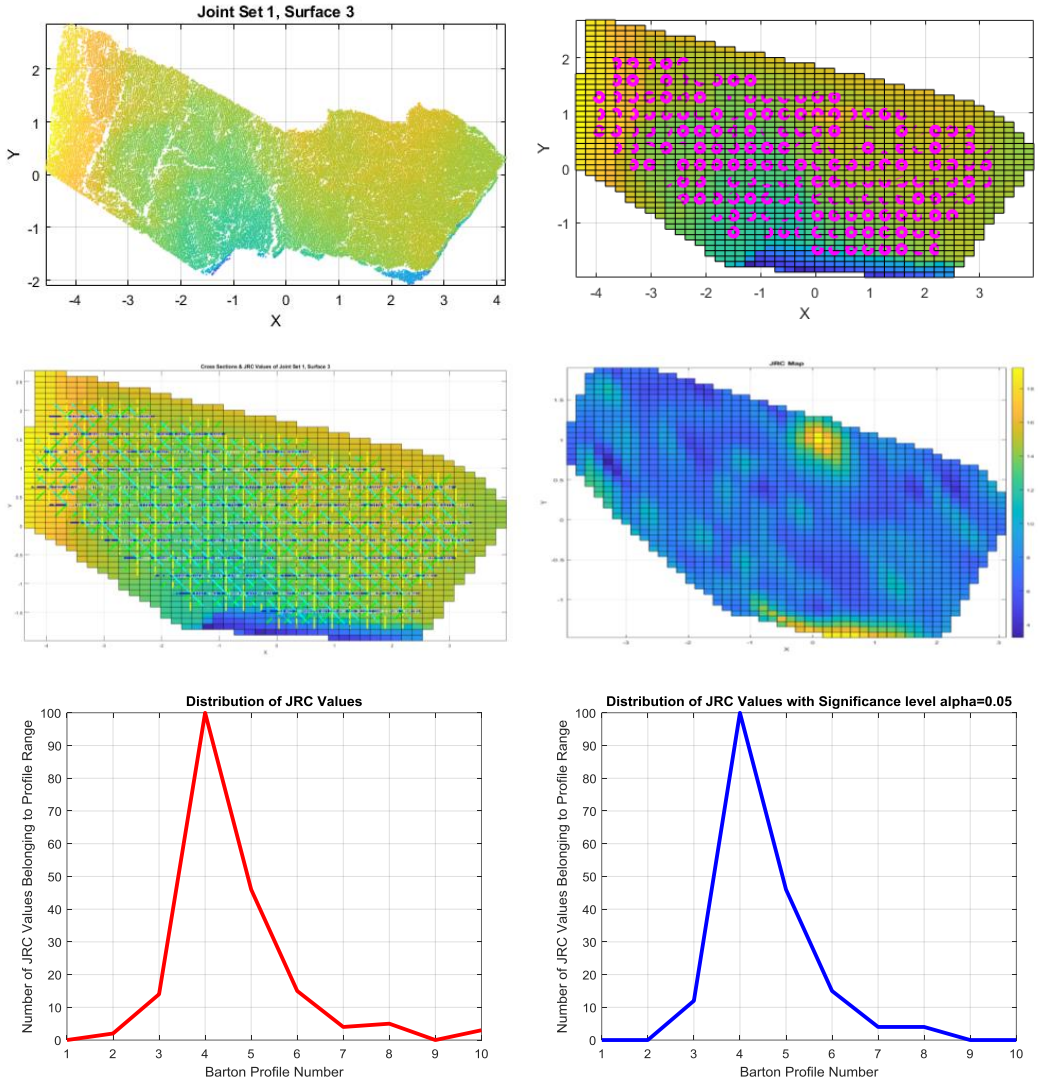

Figure 8.8. JRC estimation process of Joint Set 1, Surface 3.

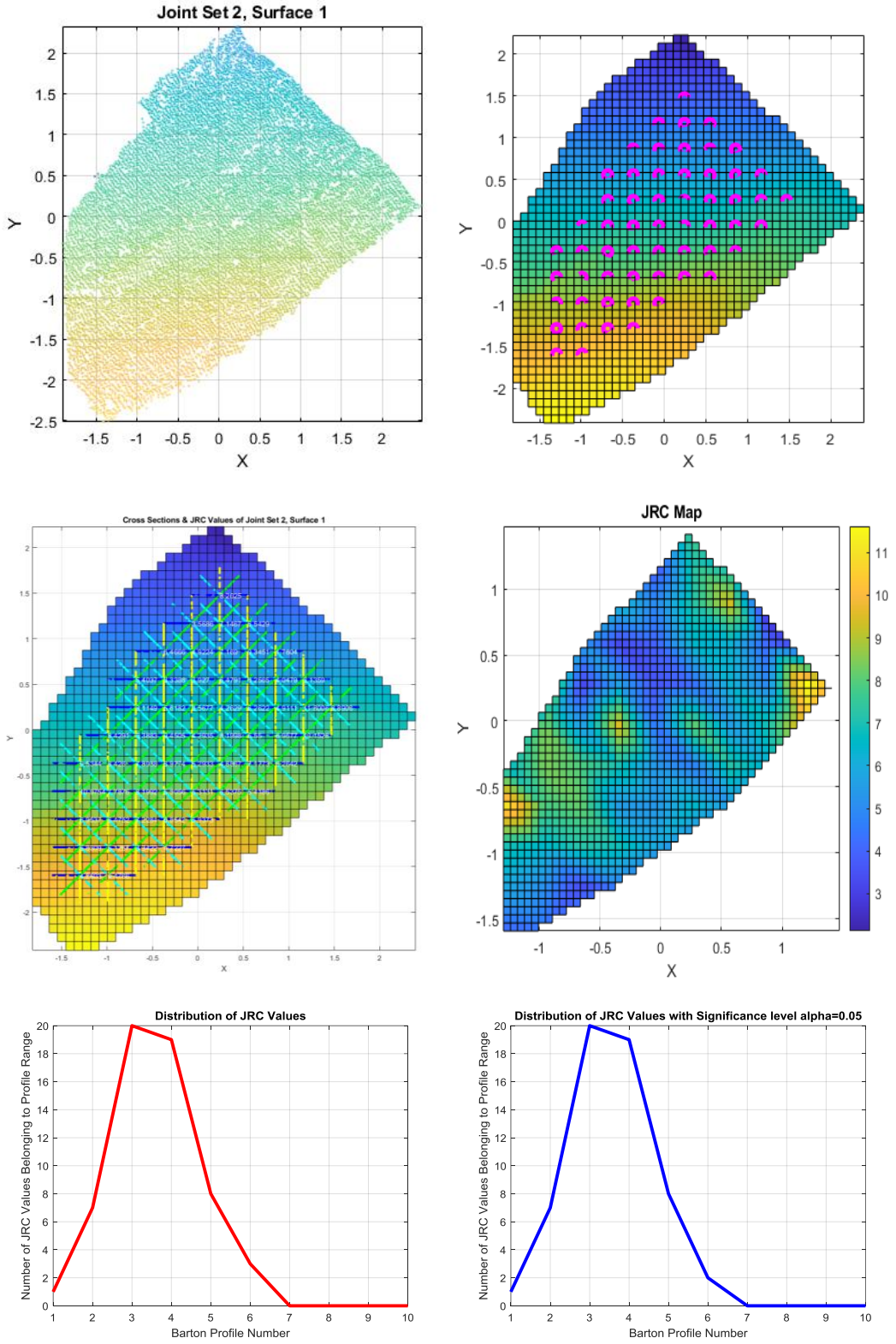

Figure 8.9. JRC estimation process of Joint Set 2, Surface 1.

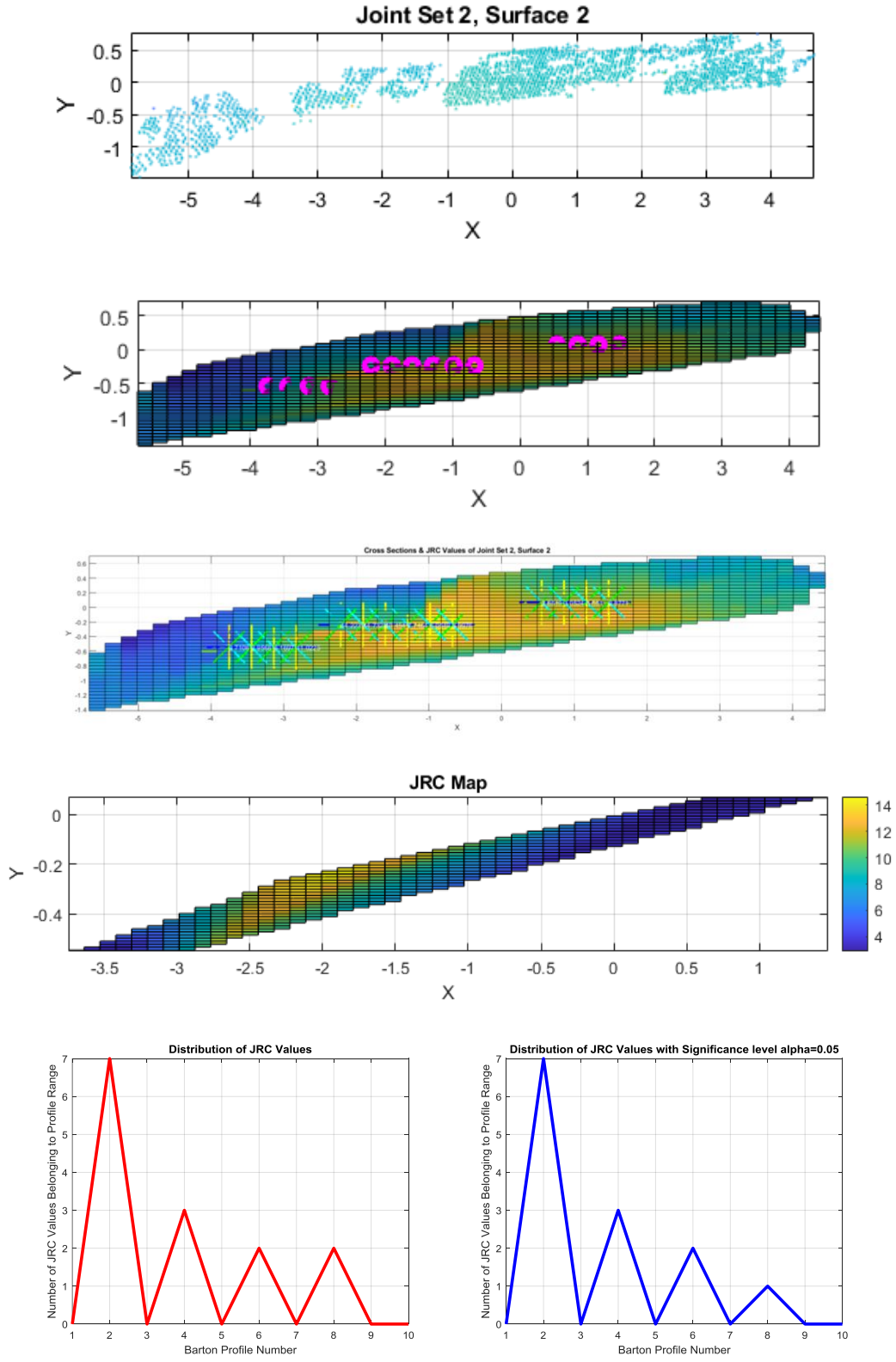

Figure 8.10. JRC estimation process of Joint Set 2, Surface 2.

8.2 JRC Estimation Using Representative Regions

In the previous section, the entire data of the study area was used. This is impractical on several fronts. First, the processing time for the JRC determination of the entire surface can be too long depending on the amount of data. Second, there can be irregularities on the surface. Jagged surface or distorted point cloud in certain areas can increase the JRC of the surface, while lack of data will result in flat surfaces with near-zero JRC. To avoid such outliers and missing data, a smaller but representative area of the surface can be chosen for JRC estimation.

In this case study, representative regions are selected only for the surfaces of Joint Set 1, since the surfaces of Joint Set 2 are already too small. While selecting representative regions, it is essential to avoid irregular surfaces formed due to mechanical fracturing or missing data caused by the use of TLS during data gathering. It is also important to keep the representative region large enough so that a sufficient amount of JRC estimation circles can fit in it. After numerous tests, it is observed that representative regions should be larger than 200 mm in all dimensions in order to produce a healthy JRC map of the surface. The coordinates of the representative regions of the three surfaces of Joint Set 1 are listed below.

- Joint Set 1 Surface 1: x [22.5, 32.25] y [-5, -2] z [3, 5]
- Joint Set 1 Surface 2: x [23.14, 31.77] y [0, 2.5] z [2.5, 3.7]
- Joint Set 1 Surface 3: x [23.94, 30.86] y [3.3, 5.5] z [1.6, 3]

The representative regions and their positions on the surfaces are displayed in Figure 8.11. The same process for JRC estimation is applied to the representative surfaces. The resulting JRC maps are shown in Figure 8.12. to 8.14. for all three surfaces. The resulting JRC values are given in Table 8.1. for comparison with the JRC values obtained from full surface data.

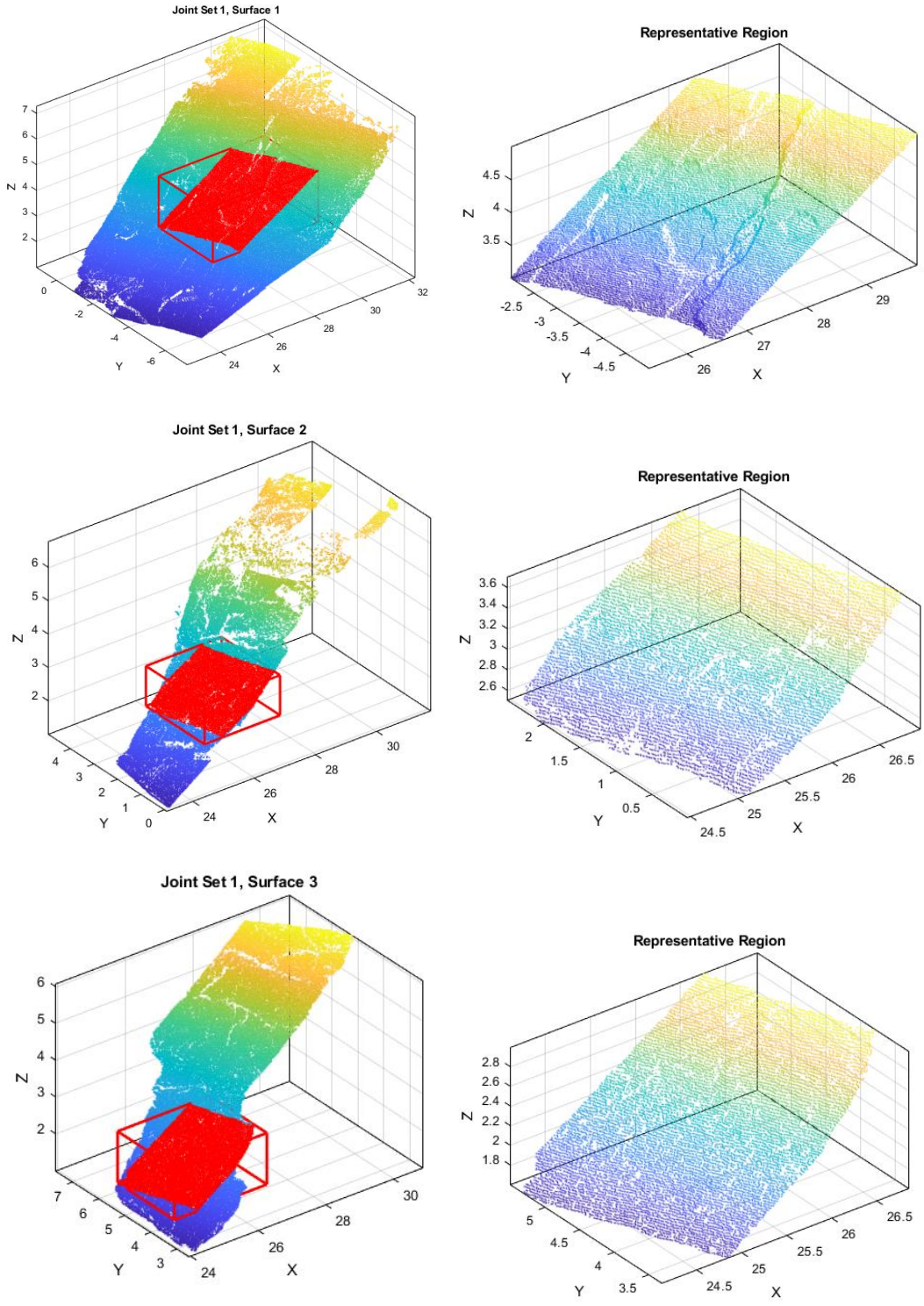

Figure 8.11. Representative regions selected from the three surfaces of the first joint set.

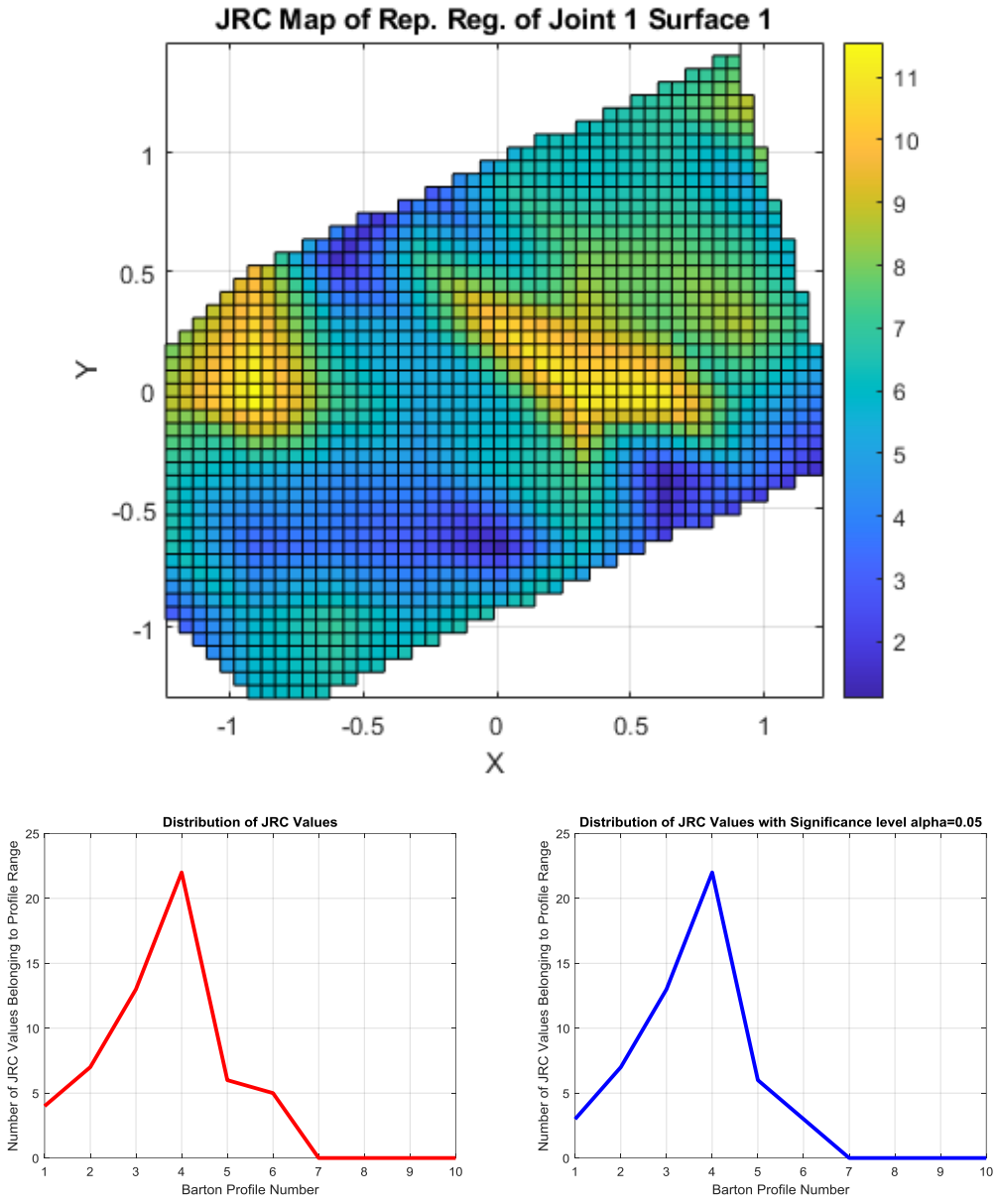

Figure 8.12. JRC map and value distribution of Joint Set 1, Surface 1.

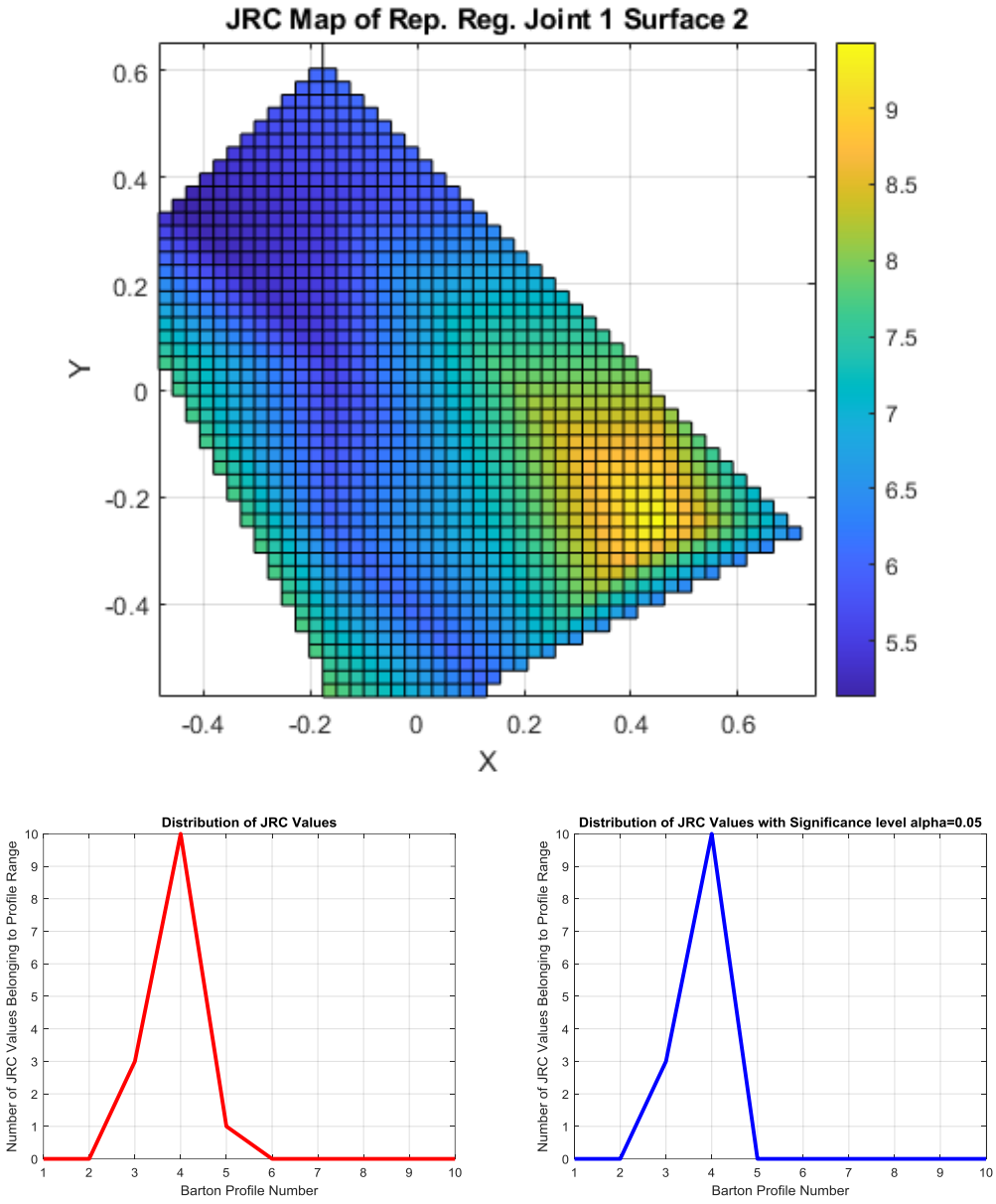

Figure 8.13. JRC map and value distribution of Joint Set 1, Surface 2.

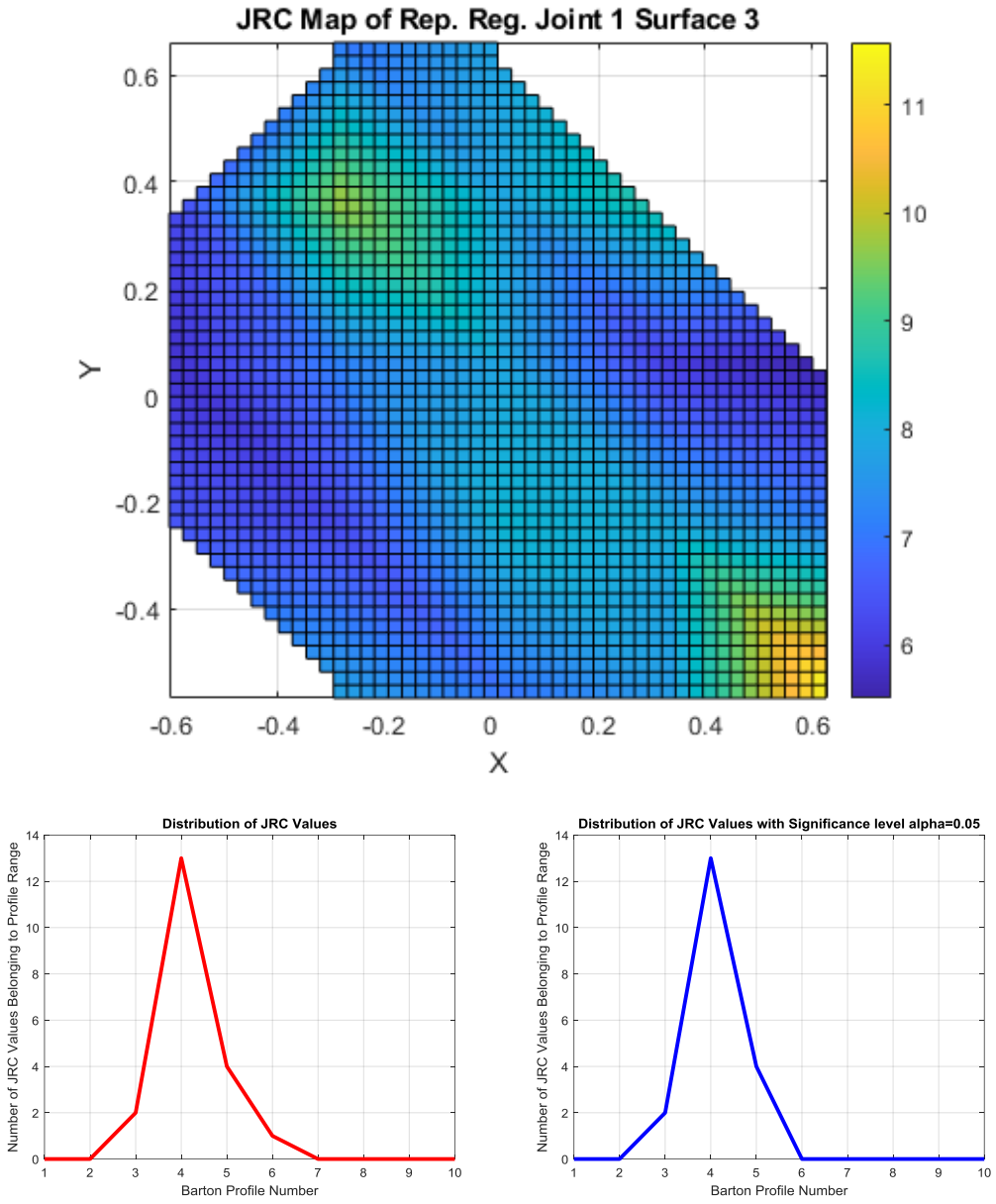

Figure 8.14. JRC map and value distribution of Joint Set 1, Surface 3.

Table 8.1 Estimated minimum, maximum, and mean JRC values and the standard deviation of JRC values for discontinuity surfaces of case study data.

	Full Data								Representative Data							
	Min JRC	**Mean JRC**	**Max JRC**	**STD**	**Min JRC α=0.05**	**Mean JRC α=0.05**	**Max JRC α=0.05**	**STD α=0.05**	**Min JRC**	**Mean JRC**	**Max JRC**	**STD**	**Min JRC α=0.05**	**Mean JRC α=0.05**	**Max JRC α=0.05**	**STD α=0.05**
Joint Set 1 Surface 1	0.72	6.35	13.78	2.35	1.89	6.32	11.54	2.04	0.94	6.15	11.71	2.61	1.00	6.04	11.30	2.35
Joint Set 1 Surface 2	0.76	6.88	14.20	2.99	2.19	6.82	13.75	2.67	5.10	6.74	9.50	1.24	5.10	6.53	7.88	1.00
Joint Set 1 Surface 3	2.72	8.15	20	2.62	4.76	7.96	15.25	1.95	5.51	7.51	11.57	1.43	5.51	7.29	9.78	1.09
Joint Set 2 Surface 1	1.78	6.19	11.80	2.04	1.78	6.09	10.98	1.74	-	-	-		-	-	-	-
Joint Set 2 Surface 2	2.86	6.65	14.73	4.30	2.86	6.02	14.22	3.77	-	-	-		-	-	-	-

8.3 Discussion and Conclusions

Joint Set 1 Surface 1 has the largest area with high point density, with some irregularities at the center. While a large representative region can be selected, it will always include the irregular parts of the surface. The difference between the full and representative data is not significant in terms of the mean JRC. However, the standard deviation shows that the representative region is worse in terms of JRC distribution with respect to the full surface as there are more low and high-end JRC values. At first glance, Joint Set 1 Surface 1 looks ideal for being the representative of the whole discontinuity set. However, detailed examination reveals that the irregular features in the surface's center make this surface less reliable in estimating JRC.

Joint Set 1 Surface 2 has irregular point cloud data in its upper half, most of which were removed during the plane detection process. Hence, the representative region for the second surface was selected from the lower half with a smaller area relative to the first surface. The mean JRC results are higher compared to the first surface even when the representative region is used. The differences between the JRC values, however, are not significant as they both share the 4^{th} Barton and Choubey reference profile, with JRC values of 6 to 8.

Joint Set 1 Surface 3 had no irregularities resulting from TLS data acquisition. However, the small changes in elevation along the surface show that irregularities due to mechanical fracturing are present. These irregularities resulted in even higher JRC values relative to the first surface. The smaller representative region and the presence of an irregular surface might eliminate this surface from being considered as a representative, as it might cause overestimation of the discontinuity set's JRC. However, the JRC values of this surface still lie within the 4^{th} reference profile. Thus, this surface should not be disqualified as unsuitable for JRC estimation.

Joint Set 2 Surface 1 and Surface 2 both did not have sufficient area to produce representative regions. Surface 1 had a decent point density and little to no irregularities. Its mean JRC value matched that of Joint Set 1 Surface 1. Joint Set 2 Surface 2 on the other hand, is problematic due to its small area and TLS based irregularities. While the mean JRC value seems to match that of Joint Set 2 Surface 1, the large areas of missing data cannot be ignored. Missing data produces artificial smooth surfaces in the JRC estimation process, which will lower the mean JRC. Further, it is observed from Table 8.1. that the standard deviation of the JRC values is almost four times those of other surfaces. The low number of JRC estimation circles coupled with the missing data disqualifies Joint Set 2 Surface 2 from being suitable for JRC estimation.

It is advised that representative regions and the significance level $\alpha=0.05$ are both used in estimating the JRC. This allows users to find JRC of large discontinuity surfaces efficiently with a minimal margin of error. The selection of representative regions is of great importance since it will determine how accurate the JRC results will be. The representative regions should include as few irregularities as possible while being large enough to have more than 10 JRC estimation circles. These circles should not be lined up, in order to represent the surface better. In conclusion, the novel JRC estimation method can be utilized for entire discontinuity surfaces and not just for single profiles.

CHAPTER 9

CONCLUSION

Rock shear strength is one of the most significant parameters of rock failure criteria. Shear strength of jointed rock masses plays a vital role in geological engineering applications such as slope stability analysis, mining, tunneling, and dam construction. The shear strength of rock masses is primarily determined by their discontinuity surfaces. Thus, it is imperative to determine discontinuity properties to determine the shear strength of the rock masses. To obtain discontinuity properties, the conventional approach has been the collection of data in areas of interest by manual fieldwork. Thus, surveyors have to estimate the discontinuity properties of the entire area using the data collected.

In recent years, however, traditional methods for data collection in field surveys are being replaced by the applications of newer data-gathering technologies such as TLS. These technologies allow surveyors to collect data from large areas in less time and often in much greater detail, providing a point cloud data of the surface. However, TLS is only a tool for gathering data. In order to analyze this data, an accompanying methodology to extract the relevant information as truthfully as possible is required. To be able to work with huge amounts of data and derive discontinuity properties in a short time, an accompanying software in which the methodology, is implemented is also necessary.

To accomplish this process more efficiently without the use of extensive laboratory testing and time-consuming field survey, a computer program called Discontinuity Analysis has been developed in this study. The steps of deriving discontinuity parameters from the point cloud data have been clearly identified. For each step, the available methods have been evaluated with respect to their accuracy and efficiency. After the methodology to be followed has been completed, a GUI is developed on the Matlab platform.

The Discontinuity Analysis software provides facilities to load, preprocess, and detect discontinuity sets from point cloud data obtained from TLS. The determination of the number, orientation, spacing, persistence, and block size of these discontinuity sets is automated. The software allows the user to select regions of interest in the survey area, to lower the processing requirements of the hardware. Discontinuity Analysis software is thus a user friendly and extensively automatized tool for the determination of discontinuity properties in a single GUI.

Among the discontinuity properties, the automatic estimation of the JRC value for surface profiles is rather complicated. The conventional approach depends on the visual comparison of the samples with standard reference profiles. There are some methods in the literature based on the use of statistical parameters and fractal dimensions which can be incorporated in an automatic procedure. However, these methods have many different varieties and they have been shown to give different results. Therefore, a new method to determine the JRC value of a sample profile objectively and accurately is needed for use in an automatic procedure. After testing statistical, similarity, and fractal methods, it has been decided to use power spectral density as the tool for determining JRC. While PSD is commonly used in other fields of engineering, its use has been limited to an intermediate tool in some of the researches for the estimation of JRC.

The method proposed in this study can be used for automated processes in JRC estimation for large numbers of sample profiles. As distinct from previous attempts making use of the PSD as an intermediate tool, the proposed method directly uses the PSD of the reference and sample surface profiles. In trials with a large number of cases available in the literature, the comparison of the results obtained with those from the well-known and commonly used methods, show that the method yields more accurate and precise estimations. Another positive aspect of the proposed method is the almost zero mean for the estimation error. The proposed method is particularly suited to the automatic evaluation and can be easily programmed as a module that can be embedded into larger software for the determination of discontinuity properties of rock masses.

The proposed method is further extended into estimating the JRC of entire surface areas by the use of multiple profiles to find the mean JRC of areas they cover. The case study of this areal JRC estimation method displayed that it is possible to estimate the JRC of entire discontinuity sets using carefully selected representative areas.

In conclusion, a methodology for the determination of discontinuity surface properties of rock masses using TLS point cloud data has been accomplished. It is implemented in software for automated extraction of the parameters.

9.1 Recommendations

Despite the extensive capabilities of Discontinuity Analysis Software and Profile Analyzer, there are still some features that can be added. The ability to drape photographs or images onto the point cloud data can allow for additional discontinuity properties to be determined. Images provide color and from such data, properties such as filling and aperture can also be extracted. Additionally, an approach for the automatic determination of the parameters Eps and MinPts for the DBSCAN application will improve the automation of the process.

This study has displayed the potential of PSD in studying roughness and rock mechanics. It is clear that with the current level of research, determining the JRC of a rock surface is still limited. The use of surface profiles generated from cross-sections of a rock surface should now be extended to the definition of the overall roughness of the surface. The current JRC estimation method can still be influenced by users, as they select the location, direction, and the number of profiles to be analyzed.

It is recommended that future work should be focused on finding JRC for the entire surfaces instead of individual profiles. The PSD of 3D surfaces can be obtained from the point cloud data. Thus, the method proposed for the estimation of JRC values of surface profiles may be extended to the estimation of the JRC value for the whole surface of interest. In the case of the analysis of surface profiles, the standard reference profiles provided by Barton and Choubey are available. However, there are no similar reference surfaces with known JRC values for comparison in the case of 3D surfaces. Thus, reference 3D surfaces with JRC values determined by laboratory testing are required. Once this is accomplished, the proposed method for surface profiles can be extended to the estimation of the roughness of an entire surface.

REFERENCES

Abellán, A., Vilaplana, J.M., Martínez, J., 2006. Application of a long-range Terrestrial Laser Scanner to a detailed rockfall study at Vall de Núria (Eastern Pyrenees, Spain). Eng. Geol. 88, 136–148. http://dx.doi.org/10.1016/j.enggeo.2006.09.012.

Abellán, A., Jaboyedoff, M., Oppikofer, T., Vilaplana, J.M., 2009. Detection of millimetric deformation using a terrestrial laser scanner: experiment and application to a rockfall event. Nat. Hazards Earth Syst. Sci. 9, 365–372. http://dx.doi.org/10.5194/nhess-9-365-2009.

Abellán, A., Calvet, J., Vilaplana, J.M., Blanchard, J., 2010. Detection and spatial prediction of rockfalls by means of terrestrial laser scanner monitoring. Geomorphology 119, 162–171. http://dx.doi.org/10.1016/j.geomorph.2010.03.016.

Abellán, A., Vilaplana, J.M., Calvet, J., García-Sellés, D., Asensio, E., 2011. Rockfall monitoring by Terrestrial Laser Scanning – case study of the basaltic rock face at Castellfollit de la Roca (Catalonia, Spain). Nat. Hazards Earth Syst. Sci. 11, 829–841. http://dx.doi.org/10.5194/nhess-11-829-2011.

Abellán, A., Oppikofer, T., Jaboyedoff, M., Rosser, N.J., Lim, M., Lato, M.J., 2014. Terrestrial laser scanning of rock slope instabilities. Earth Surf. Process. Landf. 39, 80–97. http://dx.doi.org/10.1002/esp.3493.

Alameda-Hernandez P, Jimênez-Perâlvarez J, Palenzuela JA, El Hamdouni R, Irigaray C, Cabrerizo MA, Chacôn J. 2014. Improvement of the JRC calculation using different parameters obtained through a new survey method applied to rock discontinuities, Rock Mech Rock Eng., 47(6):2047–2060.

Alba, M., Barazzetti, L., Fabio, F., Scaioni, M., 2011. Filtering vegetation from terrestrial point clouds with low-cost near infrared cameras. Ital. J. Remote Sens. 55–75. http://dx.doi.org/10.5721/ItJRS20114325.

Alcock SG, Ludbrook GD, Owen T, and Dockree R. 2010. Using the Power Spectral Density method to characterise the surface topography of optical surfaces, Proceedings of SPIE - The International Society for Optical Engineering, 7801.

Alessio SM. 2016. Digital Signal Processing and Spectral Analysis for Scientists: Concepts and Applications, New York, Springer.

Altuntaş C., Yıldız F., and Scaioni M. 2016. Laser Scanning and Data Integration for Three-Dimensional Digital Recording of Complex Historical Structures: The Case of Mevlana Museum, ISPRS Int. J. Geo-Inf. 2016, 5, 18; doi:10.3390/ijgi5020018.

ArcGIS. What is a LAS dataset? Available from: https://desktop.arcgis.com/en/arcmap/10.3/manage-data/las-dataset/what-is-a-las-dataset-.htm [Accessed December 2019]

Aryal, A., Brooks, B.A., Reid, M.E., Bawden, G.W., Pawlak, G.R., 2012. Displacement fields from point cloud data: application of particle imaging velocimetry to landslide geodesy. J. Geophys. Res. Earth Surf. 117, F01029. http://dx.doi.org/10.1029/2011JF002161.

Aryal, A., Brooks, B.A., Reid, M.E., 2015. Landslide subsurface slip geometry inferred from 3-D surface displacement fields. Geophys. Res. Lett. 42, 2014GL062688. http://dx.doi.org/10.1002/2014GL062688.

Bae D-S, Kim K, Koh Y, Kim J. 2011. Characterization of Joint Roughness in Granite by Applying the Scan Circle Technique to Images from a Borehole Televiewer, Rock Mech Rock Eng., 44(4):497-504.

Baek N., Shin W., Kim K. J., 2017. Geometric Primitive Extraction from LiDAR-scanned Point Clouds, Cluster Comput 20:741–748.

Baldo, M., Bicocchi, C., Chiocchini, U., Giordan, D., Lollino, G., 2009. LIDAR monitoring of mass wasting processes: the Radicofani landslide, Province of

Siena, Central Italy. Geomorphology 105, 193–201. http://dx.doi.org/10.1016/j.geomorph.2008.09.015.

Bandis SC. 1980. Experimental studies of scale effects on shear strength and deformation of rock joint. PhD thesis, University of Leeds.

Bandis SC, Lumsden AC, Barton NR. 1983. Fundamentals of rock joint deformation, Int J Rock Mech Min Sci Geomech Abstr., 20(6):249–68.

Barton N, Choubey V. 1977. The shear strength of rock joints in theory and practice, Rock Mech Rock Eng., 10(1–2):1–54.

Beer AJ, Stead D, Coggan JS. 2002. Technical note estimation of the joint roughness coefficient (JRC) by visual comparison, Rock Mech Rock Eng., 35(1):65–74.

Belem T, Homand-Etienne F, Souley M. 2000. Quantitative Parameters for Rock Joint Surface Roughness, Rock Mech Rock Eng., 33(4):217-242.

Besl P. J. and McKay N. D., 1992. A method for registration of 3-D shapes. IEEE Transactions on Pattern Analysis and Machine Intelligence, vol. 14, no. 2, pp. 239-256, doi: 10.1109/34.121791.

Bistacchi, A., Griffith, W.A., Smith, S.A.F., Di Toro, G., Jones, R., Nielsen, S., 2011. Fault roughness at seismogenic depths from lidar and photogrammetric analysis. Pure Appl. Geophys. 168, 2345–2363. http://dx.doi.org/10.1007/s00024-011-0301-7.

Bitenc M., Kieffer D. S., and Khoshelham K., 2016. Evaluation of Wavelet and Non-Local Mean Denoising Of Terrestrial Laser Scanning Data for Small-Scale Joint Roughness Estimation, The International Archives of the Photogrammetry, Remote Sensing and Spatial Information Sciences, Volume XLI-B3, 2016, XXIII ISPRS Congress, 12–19 July 2016, Prague, Czech Republic.

Blasone, G., Cavalli, M., Marchi, L., Cazorzi, F., 2014. Monitoring sediment source areas in a debris-flow catchment using terrestrial laser scanning. Catena 123, 23–36. http://dx.doi.org/10.1016/j.catena.2014.07.001.

Blyth, G.G.H., de Freitas, M.H., 1974. A Geology for Engineers, sixth ed. Edward Arnold, London.

Bourke P. PLY - Polygon File Format. Available from: http://paulbourke.net/dataformats/ply/ [Accessed November 2016]

Bremer, M., Sass, O., 2012. Combining airborne and terrestrial laser scanning for quantifying erosion and deposition by a debris flow event. Geomorphology 138, 49–60. http://dx.doi.org/10.1016/j.geomorph.2011.08.024.

Brideau, M.A., Massey, C.I., Archibald, G.C., Jaboyedoff, M., 2012. Terrestrial Photogrammetry and LiDAR Investigation of the Cliffs Associated with the Seismically Triggered Rockfalls during the February and June 2011 Christchurch Earthquakes. CRC Press, United States, United States, pp. 1179–1185.

Brodsky, E.E., Gilchrist, J.J., Sagy, A., Collettini, C., 2011. Faults smooth gradually as a function of slip. Earth Planet. Sci. Lett. 302, 185–193. http://dx.doi.org/10.1016/j.epsl.2010.12.010.

Brown SR, Scholz CH. 1985. Broad bandwidth study of the topography of natural rock surfaces, Jour. Geophys. Res., 90(B14):12575-12582.

Candela, T., Renard, F., Bouchon, M., Brouste, A., Marsan, D., Schmittbuhl, J., Voisin, C., 2009. Characterization of fault roughness at various scales: implications of three-dimensional high resolution topography measurements. Pure Appl. Geophys. 166, 1817–1851. http://dx.doi.org/10.1007/s00024-009-0521-2.

Candela, T., Renard, F., Schmittbuhl, J., Bouchon, M., Brodsky, E.E., 2011. Fault slip distribution and fault roughness. Geophys. J. Int. 187, 959–968. http://dx.doi.org/10.1111/j.1365-246X.2011.05189.x.

Candela, T., Renard, F., 2012. Segment linkage process at the origin of slip surface roughness: evidence from the Dixie Valley fault. In: Fault Zone Structure, Mechanics and Evolution in Nature and Experiment. J. Struct. Geol. 45. pp. 87–100. http://dx.doi.org/10.1016/j.jsg.2012.06.003.

Cao T., Xiao A., Wu L. and Mao L. 2017. Automatic fracture detection based on Terrestrial Laser Scanning data: A new method and case study, Computers & Geosciences 106, 209–216.

Carr J. R. and Benzer W. B., 1991. On the Practice of Estimating Fractal Dimension, Mathematical Geology, Vol 23, No. 7.

Carrea, D., Abellan, A., Derron, M.-H., Jaboyedoff, M., 2015. Automatic Rockfalls Volume Estimation Based on Terrestrial Laser Scanning Data, in: Engineering Geology for Society and Territory - Volume 2. Springer, Cham, pp. 425–428. http://dx.doi.org/10.1007/978-3-319-09057-3_68.

Chen N., Kemeny J., Jiang Q., and Pan Z., 2017. Automatic extraction of blocks from 3D point clouds of fractured rock, Computers & Geosciences, Volume 109, Pages 149-161. https://doi.org/10.1016/j.cageo.2017.08.013

Cheng Q. 1997. Multifractal Modeling and Lacunarity Analysis, Math Geol., 29(7):919-932.

Cheung CF, Chan KC, and Lee WB. 2003. A Power Spectrum Analysis of Surface Generation in Ultraprecision Machining of Al SiC Metal Matrix Composites, Materials and Manufacturing Processes, 18(6):929-942.

Chunxia J., et al., 2017. “Evaluation of fractal dimension of soft terrain surface”, Journal of Terramechanics 70, 27–34.

Collins, B.D., Kayen, R., Reiss, T., Sitar, N., 2007. Terrestrial LIDAR Investigation of the December 2003 and January 2007 Activations of the Northridge Bluff

Landslide, Daly City, California (USGS Numbered Series No. 2007–1079), Open-File Report. U.S. Geological Survey, Reston, VA.

Conner, J.C., Olsen, M.J., 2014. Automated quantification of distributed landslide movement using circular tree trunks extracted from terrestrial laser scan data. Comput. Geosci. 67, 31–39. http://dx.doi.org/10.1016/j.cageo.2014.02.007.

Corsini, A., Castagnetti, C., Bertacchini, E., Rivola, R., Ronchetti, F., Capra, A., 2013. Integrating airborne and multi-temporal long-range terrestrial laser scanning with total station measurements for mapping and monitoring a compound slow moving rock slide. Earth Surf. Process. Landf. 38, 1330–1338. http://dx.doi.org/10.1002/esp.3445.

Data Clustering Algorithms. k-means clustering algorithm. Available from: https://sites.google.com/site/dataclusteringalgorithms/k-means-clustering-algorithm [Accessed November 2016]

Dearman, W.R., 1991. Engineering Geological Mapping. Butterworth-Heineman, Oxford. Deere, D.U., 1964. Technical description of rock cores for engineering purposes. Rock Mech. Rock. Eng. 1, 107–116.

Develi K, Babadagli T. 1998. Quantification of Natural Fracture Surfaces Using Fractal Geometry, Mathematical Geometry, 30(8):671-998.

Dunning, S.A., Massey, C.I., Rosser, N.J., 2009. Structural and geomorphological features of landslides in the Bhutan Himalaya derived from Terrestrial Laser Scanning. In: Geomorphology, Dating, Triggering, Modelling, and Hazard Assessment of Large Landslides. 103. pp. 17–29. http://dx.doi.org/10.1016/j.geomorph.2008.04.013.

Duparré A, Ferre-Borrull J, Gliech S, Notni G, Steinert J, and Bennett JM. 2002. Surface characterization techniques for determining the root-mean-square roughness and power spectral densities of optical components, Applied Optics, 41(1):154-171.

Durst PJ, Mason LM, McKinley B, Baylot A. 2011. Predicting RMS surface roughness using fractal dimension and PSD parameters, Journal of Terramechanics, 48:105-111.

Einstein, H.H., Veneziano, D., Baecher, G.B., and O'Reilly, K.J. 1983. The effect of discontinuity persistence on rock slope stability. International Journal of Rock Mechanics and Mining Sciences and Geomechanics Abstracts, 20(5): 227–236.

(PDF) Analysis of the removability and stability of rock blocks by considering the rock bridge effect. Available from: https://www.researchgate.net/publication/283185886_Analysis_of_the_removability_and_stability_of_rock_blocks_by_considering_the_rock_bridge_effect [accessed Dec 16 2019].

Ester M., Kriegel H. P., Sander, J., and Xu. X. 1996. A Density Based Algorithm for Discovering Clusters in Large Spatial Databases with Noise, KDD-96.

Fekete S, Diederichs M, Lato V. 2010. Geotechnical and operational applications for 3-dimensional laser scanning in drill and blast tunnels, Tunneling and Underground Space Technology, 25: 614–628.

Feng, Q., Sjögren, P., Stephansson, O., Jing, L., 2001. Measuring fracture orientation at exposed rock faces by using a non-reflector total station. Eng. Geol. 59, 133–146. http://dx.doi.org/10.1016/S0013-7952(00)00070-3.

Fischler M. A. and Bolles R. C. 1981. Random Sample Consensus: A Paradigm for Model Fitting with Applications to Image Analysis and Automated Cartography, Communications of the ACM, 24(6):381–395.

Ge Y., Kulatilake P. H. S. W., Tang H., and Xiong C. 2014. Investigation of natural rock joint roughness, Computers and Geotechnics, Volume 55, January 2014, Pages 290-305. https://doi.org/10.1016/j.compgeo.2013.09.015

GeoCue Group Support. What is the LAS format? Available from: https://support.geocue.com/what-is-the-las-format/ [Accessed August 2019]

Gigli G. and Casagli N. 2011. Semi-automatic extraction of rockmass structural data from high resolution LIDAR point clouds, International Journal of Rock Mechanics & Mining Sciences 48, 187–198.

Goodin C., Stevens M., Villfane-Rosa F. J., McKinley B., Gates B. Q., Durst P., Mason G., and Baylot A. 2017. Calculating fractal parameters from low-resolution terrain profiles, Journal of Terramechanics, 72, 21–26.

Graselli G. 2001. Shear Strength of Rock Joints Based on Quantified Surface Description. PhD Thesis, Ecole Polytechnique Federale De Lausanne (EPFL).

Grasselli G and Egger P. 2003. Constitutive law for the shear strength of rock joints based on three-dimensional surface parameters, International Journal of Rock Mechanics and Mining Sciences, 40(1):25–40.

Haddad, D.E., Akciz, S.O., Arrowsmith, J.R., Rhodes, D.D., Oldow, J.S., Zielke, O., Toke, N.A., Haddad, A.G., Mauer, J., Shilpakar, P., 2012. Applications of airborne and terrestrial laser scanning to paleoseismology. Geosphere 8, 771–786. http://dx.doi.org/10.1130/GES00701.1.

Harris FJ. 1987. On the use of windows for harmonic analysis with the discrete Fourier transform, Proceedings of the IEEE, 66(1):51-83.

Heckmann, T., Bimböse, M., Krautblatter, M., Haas, F., Becht, M., Morche, D., 2012. From geotechnical analysis to quantification and modelling using LiDAR data: a study on rockfall in the Reintal catchment, Bavarian Alps, Germany. Earth Surf. Process. Landf. 37, 119–133. http://dx.doi.org/10.1002/esp.2250.

Hills, E.S., 1972. Elements of Structural Geology, second ed. Chapman and Hall, London.

Hobbs, B.E., 1976. An Outline of Structural Geology. Wiley, New York.

Hoek, E., Brown, E.T., 1980a. Underground Excavation in Rock. Institution of Mining and Metallurgy, London, UK.

Hsiung SM, Ghosh A, Ahola MP, Chowdhury AH. 1993. Assessment of Conventional Methodologies for Joint Roughness Coefficient Determination, Int. J. Rock Mech. Min. Sci. & Geomech. Abstr., 30(7):825-829.

Huang SL, Oelfke SM, Speck RC. 1992. Applicability of fractal characterization and modelling to rock joint profiles, Int. J. Rock. Mech. Min. Sci. & Geomech. Abstr., 29(2):89–98.

ISRM (International Society for Rock Mechanics). 1987. Suggested methods for the quantitative description of discontinuities in rock masses, Int. Jour. Rock Mech. Min. Sci. and Geomech Abstr., 15:319-368.

Jacobs T, Junge T, Pastewka L. 2017. Quantitative characterization of surface topography using spectral analysis, Surface Topography: Metrology and Properties, 5(1).

Janeras, M., Navarro, M., Arnó, G., Ruiz, A., Kornus, W., Talaya, J., Barberà, M., López, F., 2004. LiDAR applications to rock fall hazard assessment in Vall de Núria. In: 4th ICA Mountain Cartography Workshop. Vall de Nuria, Catalonia, Spain.

Jang H-S, Kang S-S, Jang B-A. 2014. Determination of Joint Roughness Coefficients Using Roughness Parameters, Rock Mech Rock Eng., 47:2061–2073.

Jahn R and Truckenbrodt H. A. 2004. Simple fractal analysis method of the surface roughness, Journal of Materials Processing Technology, 145:40-45.

Jaboyedoff, M., Metzger, R., Oppikofer, T., Couture, R., Derron, M.-H., Locat, J., Turmel, D., 2007. New Insight Techniques to Analyze Rock-slope Relief Using DEM And 3Dimaging Cloud Points: COLTOP-3D Software.

Presented at the 1st Canada - U.S. Rock Mechanics Symposium, American Rock Mechanics Association.

Jaboyedoff, M., Oppikofer, T., Minoia, R., Locat, J., Turmel, D., 2008. Terrestrial LIDAR investigation of the 2004 rockslide along Petit Champlain street, Québec City (Québec, Canada). In: 4th Canadian Conference on Geohazards: From Causes to Management. Presse de l'Université Laval, pp. 295–301.

Jaboyedoff, M., Demers, D., Locat, J., Locat, A., Locat, P., Oppikofer, T., Robitaille, D., Turmel, D., 2009a. Use of terrestrial laser scanning for the characterization of retrogressive landslides in sensitive clay and rotational landslides in river banks. Can. Geotech. J. 46, 1379–1390. http://dx.doi.org/10.1139/T09-073.

Jaboyedoff, M., Pedrazzini, A., Loye, A., Oppikofer, T., 2009b. Earth flow in a complex geological environment: the example of Pont Bourquin, Les Diablerets (Western Switzerland). In: Landslides Processes – From Geomorphologic Mapping Dynamic Modeling. Presented at the Landslide Processes Conference, Strasbourg, France, pp. 131–137.

Jaboyedoff, M., Pedrazzini, A., Loye, A., Oppikofer, T., 2009b. Earth flow in a complex geological environment: the example of Pont Bourquin, Les Diablerets (Western Switzerland). In: Landslides Processes – From Geomorphologic Mapping Dynamic Modeling. Presented at the Landslide Processes Conference, Strasbourg, France, pp. 131–137.

Jaboyedoff, M., Oppikofer, T., Abellán, A., Derron, M.-H., Loye, A., Metzger, R., Pedrazzini, A., 2010. Use of LIDAR in landslide investigations: a review. Nat. Hazards 61, 5–28. http://dx.doi.org/10.1007/s11069-010-9634-2.

Jing L, Nordlund E, Stephansson O. 1992. An Experimental Study on the Anisotropy and Stress-dependency of the Strength and Deformability of Rock Joints, Int. J. Rock. Mech. Min. Sci. & Geomech. Abstr., 29(6):535-542.

Kana DD, Fox DJ, Hsiung SM. 1996. Interlock/Friction Model for Dynamic Shear Response in Natural Jointed Rock, Int. J. Rock. Mech. Min. Sci. & Geomech. Abstr., 33(4):371-386.

Kasperski, J., Delacourt, C., Allemand, P., Potherat, P., Jaud, M., Varrel, E., 2010. Application of a terrestrial laser scanner (TLS) to the study of the Séchilienne landslide (Isère, France). Remote Sens. 2, 2785–2802. http://dx.doi.org/10.3390/rs122785.

Kemeny, J.M., Turner, A.K., 2008. GROUND-BASED LiDAR Rock Slope Mapping and Assessment (Final Report No. FHWA-CFL/TD-08-006). Federal Highway Administration Central Federal Lands Highway Division.

Klinkenberg B. A. 1994. Review of methods used to determine the fractal dimension of linear features, Math. Geology, 36(1):23-46.

Kokkalas, S., Jones, R.R., McCaffrey, K.J.W., Clegg, P., 2007. In: Quantitative Fault Analysis at Arkitsa, Central Greece, Using Terrestrial Laser-Scanning ("LiDAR"). Proceedings of the 11th International Congress XXXVII. Bull. Geol. Soc. Greece.

Kromer, R.A., Hutchinson, D.J., Lato, M.J., Gauthier, D., Edwards, T., 2015. Identifying rock slope failure precursors using LiDAR for transportation corridor hazard management. Eng. Geol. 195, 93–103. http://dx.doi.org/10.1016/j.enggeo.2015.05.012.

Kuhn, D., Prüfer, S., 2014. Coastal cliff monitoring and analysis of mass wasting processes with the application of terrestrial laser scanning: a case study of Rügen, Germany. Geomorphology 213, 153–165. http://dx.doi.org/10.1016/j.geomorph.2014.01.005.

Lato, M., Diederichs, M.S., Hutchinson, D.J., Harrap, R., 2009. Optimization of LiDAR scanning and processing for automated structural evaluation of discontinuities in rockmasses. Int. J. Rock Mech. Min. Sci. 46, 194–199. http://dx.doi.org/10.1016/j.ijrmms.2008.04.007.

Lee YH, Carr JR., Barr DJ, Haas, CJ. 1990. The fractal dimension as a measure of the roughness of rock discontinuity profiles, Int J Rock Mech Min Sci., 27(6):453–464.

Lehtomäki M., Jaakkola A., Hyyppä J., Lampinen J., Kaartinen H., Kukko A., Puttonen E., and Hyyppä H. 2016. Object Classification and Recognition from Mobile Laser Scanning Point Clouds in a Road Environment, IEEE Transactions On Geoscience and Remote Sensing, Vol. 54, No. 2.

Leygue A. Mathworks. Plane fit. Available from: http://www.mathworks.com/Matlabcentral/fileexchange/43305-plane-fit [Accessed November 2016]

Li Y, Huang R. 2015. Relationship between joint roughness coefficient and fractal dimension of rock fracture surfaces, Int J Rock Mech Min Sci., 75:15–22.

Li Y, Zhang Y. 2015. Quantitative estimation of joint roughness coefficient using statistical parameters, Int J Rock Mech Min Sci., 77:27–35.

Lorbeer R, Pastow J, Sawannia M, Klinkenberg P, Förster DJ, Eckel, H. 2018. Power Spectral Density Evaluation of Laser Milled Surfaces, Materials, 11(1):50-60.

Maerz NH, Franklin JA, Bennett CP. 1990. Joint roughness measurement using shadow profilometry, Int J Rock Mech Min Sci., 27(5):329–343.

Mah, J., Samson, C., McKinnon, S.D., Thibodeau, D., 2013. 3D laser imaging for surface roughness analysis. Int. J. Rock Mech. Min. Sci. 58, 111–117. http://dx.doi.org/10.1016/j.ijrmms.2012.08.001.

Mathworks a, 3-D Point Cloud Registration and Stitching. Available from: http://www.mathworks.com/help/vision/examples/3-d-point-cloud-registration-and-stitching.html [Accessed November 2016]

Mathworks b, pcdenoise. Available from: http://www.mathworks.com/help/vision/ref/pcdenoise.html [Accessed November 2016]

Micromouse Productions. XYZ Files. Available from: http://www.micromouse.ca/xyz_files.html [Accessed November 2016]

Muralha J, Graselli G, Tatone B, Blümel M, Chryssanthakis P, Yujing J. 2014. ISRM Suggested Method for Laboratory Determination of the Shear Strength of Rock Joints: Revised Version, Rock Mechanics Rock Eng., 47:291-302.

Myers NO. 1962. Characterization of surface roughness, Wear, 5(3):182-189.

Newland DE. 2005. An Introduction to Random Vibrations and Spectral Analysis, London, Longman.

Olariu, M.I., Ferguson, J.F., Aiken, C.L.V., Xu, X., 2008. Outcrop fracture characterization using terrestrial laser scanners: deep-water Jackfork sandstone at Big Rock Quarry, Arkansas. Geosphere 4, 247–259. http://dx.doi.org/10.1130/GES00139.1.

Oldow, J.S., Singleton, E.S., 2008. Application of terrestrial laser scanning in determining the pattern of late Pleistocene and Holocene fault displacement from the offset of pluvial lake shorelines in the Alvord extensional basin, northern Great Basin, USA. Geosphere 4, 536–563. http://dx.doi.org/10.1130/GES00101.1.

Olsen, M.J., Allan, J.C., Priest, G.R., 2012a. Movement and erosion quantification of the Johnson Creek, Oregon, landslide through 3D laser scanning. In: GeoCongress 2012a. American Society of Civil Engineers, pp. 3050–3059.

Olsen, M., 2013. In situ change analysis and monitoring through terrestrial laser scanning. J. Comput. Civ. Eng. 29, 04014040. http://dx.doi.org/10.1061/(ASCE)CP.1943-5487.0000328.

Olsen, M.J., Wartman, J., McAlister, M., Mahmoudabadi, H., O'Banion, M.S., Dunham, L., Cunningham, K., 2015. To fill or not to fill: sensitivity analysis of the influence of resolution and hole filling on point cloud surface modeling and individual rockfall event detection. Remote Sens. 7, 12103–12134. http://dx.doi.org/10.3390/rs70912103.

Oppikofer, T., Jaboyedoff, M., Keusen, H.-R., 2008. Collapse at the eastern Eiger flank in the Swiss Alps. Nat. Geosci. 1, 531–535. http://dx.doi.org/10.1038/ngeo258.

Oppikofer, T., Jaboyedoff, M., Blikra, L., Derron, M.-H., Metzger, R., 2009. Characterization and monitoring of the Åknes rockslide using terrestrial laser scanning. Nat. Hazards Earth Syst. Sci. 9, 1003–1019. http://dx.doi.org/10.5194/nhess-9-1003-2009.

Oppikofer, T., Bunkholt, H.S., Fischer, L., Saintot, A., Hermanns, R.L., Carrea, D., Longchamp, C., Derron, M.H., Michoud, C., Jaboyedoff, M., 2012a. Investigation and monitoring of rock slope instabilities in Norway by terrestrial laser scanning. In: Landslides and Engineered Slopes. Protecting Society through Improved Understanding: Proceedings of the 11th International & 2nd North American Symposium on Landslides. Taylor & Francis Group, London, Banff, Canada, pp. 1235–1241.

Oppikofer, T., Hermanns, R.L., Redfield, T.F., Sepulveda, S.A., Duhart, P., Bascunan, I., 2012b. Morphologic description of the Punta Cola rock avalanche and associated minor rockslides caused by the 21 April 2007 Aysen Earthquake (Patagonia, southern Chile). Rev. Asoc. Geol. Argent. 69, 339–353.

Outer AD, Kaashoek JF, and Hack HRGK. 1995. Difficulties With Using Continuous Fractal Theory for Discontinuity Surfaces, Int. J. Rock. Mech. Min. Sci. & Geomech. Abstr., 32(1):3-9.

Palmstrom A. and Broch E. 2006. Use and misuse of rock mass classification systems with particular reference to the Q-system, Tunnelling and Underground Space Technology, 21: 575–593

Pedrazzini, A., Oppikofer, T., Jaboyedoff, M., Pons, I., Guell, M., Chantry, R., Stampfli, E., 2010. Assessment of rockslide and rockfall problems in an active quarry: case study of the Arvel Quarry (Western Switzerland). In: Presented at the ISRM International Symposium - EUROCK 2010. Society for Rock Mechanics, International.

Pickering C. and Aydin A. 2015. Modeling Roughness of Rock Discontinuity Surfaces: A Signal Analysis Approach. Rock Mech Rock Eng.

PCL. The PCL Registration API. Available from: http://pointclouds.org/documentation/tutorials/registration_api.php [Accessed October 2016]

PCL. Estimating Surface Normals in a PointCloud. Available from: http://www.pointclouds.org/documentation/tutorials/normal_estimation.php [Accessed November 2016]

Pollyea, R.M., Fairley, J.P., 2011. Estimating surface roughness of terrestrial laser scan data using orthogonal distance regression. Geology 39, 623–626. http://dx.doi.org/10.1130/G32078.1.

Pollyea, R.M., Fairley, J.P., 2012. Experimental evaluation of terrestrial LiDAR-based surface roughness estimates. Geosphere 8, 222–228. http://dx.doi.org/10.1130/GES00733.1.

Price, N.J., 1966. Fault and Joint Development in Brittle and Semi-Brittle Rock. Pergamon, Oxford, UK.

Priest SD. 1993. Discontinuity Analysis for Rock Engineering. 1st ed. London, Chapman & Hall.

Priest, G.R., Allan, J.C., Niem, A.R., Niem, W.A., Dickenson, S.E., 2008. Johnson Creek Landslide Research Project. Lincoln County, Oregon.

Prokop, A., Panholzer, H., 2009. Assessing the capability of terrestrial laser scanning for monitoring slow moving landslides. Nat. Hazards Earth Syst. Sci. 9, 1921–1928. http://dx.doi.org/10.5194/nhess-9-1921-2009.

Rabatel, A., Deline, P., Jaillet, S., Ravanel, L., 2008. Rock falls in high-alpine rock walls quantified by terrestrial lidar measurements: a case study in the Mont Blanc area. Geophys. Res. Lett. 35, L10502. http://dx.doi.org/10.1029/2008GL033424.

Rahman, Z., Slob, S., Hack, R., 2006. Deriving roughness characteristics of rock mass discontinuities from terrestrial laser scan data. In: Proceedings of the 10th IAEG Congress, Engineering Geology for Tomorrow's Cities. Nottingham, United Kingdom.

Reviversoft, .MAT File Extension. Available from: https://www.reviversoft.com/file-extensions/mat [Accessed December 2019]

Riquelme A. J., Abellan A, Tomas R, Jaboyedoff M. 2014. A new approach for semi-automatic rock mass joints recognition from a 3D point clouds, Computers & Geosciences, 68:38-52.

Riquelme A. J., Abellan A., and Tomas R. 2015. Discontinuity Spacing Analysis in Rockmasses Using 3D Point Clouds, Engineering Geology 195, 185–195.

Roncella R, Forlani G. 2005. Extraction of planar patches from point clouds to retrieve dip and dip direction or rock discontinuities, ISPRS WG III/3-III/4 Workshop Laser Scanning, Enschede, the Netherlands.

Rosser, N., Lim, M., Petley, D., Dunning, S., Allison, R., 2007. Patterns of precursory rockfall prior to slope failure. J. Geophys. Res. Earth Surf. 112, F04014. http://dx.doi.org/10.1029/2006JF000642.

Rotonda, T., Marsella, M., Lizzadro, L., Ricca, A., 2007. Analysis of laser scanner data collected during a survey of faces in a rock quarry. In: Presented at the 11th ISRM Congress. Society for Rock Mechanics, International.

Rowlands, K.A., Jones, L.D., Whitworth, M., 2003. Landslide laser scanning: a new look at an old problem. Q. J. Eng. Geol. Hydrogeol. 36, 155–157. http://dx.doi.org/10.1144/1470-9236/2003-08.

Sagy, A., Brodsky, E.E., Axen, G.J., 2007. Evolution of fault-surface roughness with slip. Geology 35, 283–286. http://dx.doi.org/10.1130/G23235A.1.

Sagy, A., Brodsky, E.E., 2009. Geometric and rheological asperities in an exposed fault zone. J. Geophys. Res. Solid Earth 114, B02301. http://dx.doi.org/10.1029/2008JB005701.

Sayles RS, Thomas TR. 1978. Surface Topography as a nonstationary random process, Nature, 271:431-434.

Schulz, T., Lemy, F., Yong, S., 2005. Laser scanning technology for rock engineering applications. Opt. 3- Meas. Tech. VII Eds Gräun Kahmen Austria 50–59.

Schürch, P., Densmore, A.L., Rosser, N.J., Lim, M., McArdell, B.W., 2011. Detection of surface change in complex topography using terrestrial laser scanning: application to the Illgraben debris-flow channel. Earth Surf. Process. Landf. 36, 1847–1859. http://dx.doi.org/10.1002/esp.2206.

Seers, T.D., Hodgetts, D., 2013. Comparison of digital outcrop and conventional data collection approaches for the characterization of naturally fractured reservoir analogues. Geol. Soc. Lond. Spec. Publ. 374, 51–77. http://dx.doi.org/10.1144/SP374.13.

Seers, T.D., Hodgetts, D., 2016. Extraction of three-dimensional fracture trace maps from calibrated image sequences. Geosphere 12, 1323–1340. http://dx.doi.org/10.1130/GES01276.1.

Slob, S., Hack, R., Turner, A.K., 2002. An approach to automate discontinuity measurements of rock faces using laser scanning techniques. In: Presented at the ISRM International Symposium - EUROCK 2002, International Society for Rock Mechanics.

Slob S., Hack R., Knapen B., Turer, K., Kemeny J. 2005. A Method for Automated Discontinuity Analysis of Rock Slopes with 3D Laser Scanning, TRB Annual Meeting CD-ROM.

Spencer, E.W., 1969. Introduction to the Structure of the Earth. McGraw-Hill, New York.

Strunden, J., Ehlers, T.A., Brehm, D., Nettesheim, M., 2015. Spatial and temporal variations in rockfall determined from TLS measurements in a deglaciated valley, Switzerland. J. Geophys. Res. Earth Surf. 120, 2014JF003274. http://dx.doi.org/10.1002/2014JF003274.

Sturzenegger, M., Stead, D., Froese, C., Moreno, F., Jaboyedoff, M., 2007a. Ground-based and Airborne LiDAR For Structural Mapping of the Frank Slide. Presented at the 1st Canada - U.S. Rock Mechanics Symposium, American Rock Mechanics Association.

Sturzenegger, M., Yan, M., Stead, D., Elmo, D., 2007b. Application and limitations of ground-based laser scanning in rock slope characterization. In: Presented at the 1st Canada - U.S. Rock Mechanics Symposium, American Rock Mechanics Association.

Sturzenegger, M., Stead, D., 2009a. Quantifying discontinuity orientation and persistence on high mountain rock slopes and large landslides using terrestrial remote sensing techniques. Nat. Hazards Earth Syst. Sci. 9, 267–287. http://dx.doi.org/10.5194/nhess-9-267-2009.

Sturzenegger, M., Stead, D., 2009b. Close-range terrestrial digital photogrammetry and terrestrial laser scanning for discontinuity characterization on rock cuts. Eng. Geol. 106, 163–182. http://dx.doi.org/10.1016/j.enggeo.2009.03.004.

Sturzenegger, M., Stead, D., Elmo, D., 2011. Terrestrial remote sensing-based estimation of mean trace length, trace intensity and block size/shape. Eng. Geol. 119, 96–111. http://dx.doi.org/10.1016/j.enggeo.2011.02.005.

Tatone BSA, Grasselli G. 2010. A new 2D discontinuity roughness parameter and its correlation with JRC, Int J Rock Mech Min Sci., 47(8):1391–1400.

Tatone BSA, Grasselli G. 2013. An investigation of discontinuity roughness scale dependency using high-resolution surface measurements, Rock Mech Rock Eng., 46(4):657–681.

Telling J., Lyda A., Hartzell P., and Glennie C. 2017. Review of Earth science research using terrestrial laser scanning, Earth-Science Reviews 169, 35–68.

Teza, G., Galgaro, A., Zaltron, N., Genevois, R., 2007. Terrestrial laser scanner to detect landslide displacement fields: a new approach. Int. J. Remote Sens. 28, 3425–3446. http://dx.doi.org/10.1080/01431160601024234.

Teza, G., Pesci, A., Galgaro, A., 2008a. Grid_strain and grid_strain3: software packages for strain field computation in 2D and 3D environments. Comput. Geosci. 34, 1142–1153. http://dx.doi.org/10.1016/j.cageo.2007.07.006.

Teza, G., Pesci, A., Genevois, R., Galgaro, A., 2008b. Characterization of landslide ground surface kinematics from terrestrial laser scanning and strain field computation. Geomorphology 97, 424–437. http://dx.doi.org/10.1016/j.geomorph.2007.09.003.

Teza, G., Marcato, G., Pasuto, A., Galgaro, A., 2014. Integration of laser scanning and thermal imaging in monitoring optimization and assessment of rockfall hazard: a case history in the Carnic Alps (Northeastern Italy). Nat. Hazards 76, 1535–1549. http://dx.doi.org/10.1007/s11069-014-1545-1.

Tonini, M., Abellan, A., 2014. Rockfall detection from terrestrial LiDAR point clouds: a clustering approach using R. J. Spat. Inf. Sci. 2014, 95–110. http://dx.doi.org/10. 5311/JOSIS.2014.8.123.

Travelletti, J., Oppikofer, T., Delacourt, C., Malet, J.P., Jaboyedoff, M., 2008. Monitoring landslide displacements during a controlled rain experiment using a long-range terrestrial laser scanning (TLS). Int. Arch. Photogramm. Remote Sens. Spat. Inf. Sci. XXXVII 485–490.oy.

Trinks I, Clegg P, McCaffrey K, Jones R, Hobbs R, Holdsworth B, Holliman N, Imber J, Waggott S, Wilson R. 2005. Mapping and analysing virtual outcrops, Visual Geosciences, 10:13–19.

Tse R, Cruden DM. 1979. Estimating joint roughness coefficients. Int J Rock Mech Min Sci., 16(5):303–307.

University at Buffalo Department of Geology, Brunton Compass. Available from: http://www.glyfac.buffalo.edu/mib/course/Figures/Field/ComptonR21.jpg [Accessed November 2020]

Wang C, Wang L, Karakuş M. 2019. A new spectral analysis method for determining the joint roughness coefficient of rock joints, Int J Rock Mech Min Sci., 113:72-82.

Wang Q., Kim MK., Cheng JCP., and Sohn H. 2016. Automated quality assessment of precast concrete elements with geometry irregularities using terrestrial laser scanning, Automation in Construction, 68:170–182.

Wiatr, T., Reicherter, K., Papanikolaou, I., Fernández-Steeger, T., Mason, J., 2013. Slip vector analysis with high resolution t-LiDAR scanning. Tectonophysics 608, 947–957. http://dx.doi.org/10.1016/j.tecto.2013.07.024.

Wiatr, T., Papanikolaou, I., Fernandez Steeger, T., Reicherter, K., 2015. Bedrock fault scarp history; insight from t-lidar backscatter behaviour and analysis of structure changes. Geomorphology 228, 421–431. http://dx.doi.org/10.1016/j.geomorph.2014.09.021.

Wilson, P., Hodgetts, D., Rarity, F., Gawthorpe, R.L., Sharp, I.R., 2009. Structural geology and 4D evolution of a half-graben: new digital outcrop modelling techniques applied to the Nukhul half-graben, Suez rift. Egypt. J. Struct. Geol. 31, 328–345. http://dx.doi.org/10.1016/j.jsg.2008.11.013.

Xie X, Lu X. 2017. Development of a 3D modeling algorithm for tunnel deformation monitoring based on terrestrial laser scanning. Underground Space, 2:16-29.

Xu H-F, Zhao P-S, Li C-F, Tong Q. 2012. Predicting Joint Roughness Coefficients Using Fractal Dimension of Rock Joint Profiles, Applied Mechanics and Materials, 170-173:443-448.

Yang ZY, Lo SC, Di CC. 2001. Reassessing the Joint Roughness Coefficient JRC estimation Using Z2, Rock. Mech. Rock Eng., 34(3):243-251.

Yang ZY, Di CC, Yen KC. 2001. The effect of asperity order on the roughness of rock joints, Int. J. Rock. Mech. Min. Sci., 38:745–752.

Yu X, Vayssade B. 1991. Joint profiles and their roughness parameters, Int J Rock Mech. Min. Sci., 28(4):333–336.

Zaman T. RANSAC Plane Fitting. Available from: http://www.timzaman.com/2011/03/3d-ransac-planaire-oppervlakken-uit-puntwolken/ [Accessed November 2016]

Zhang GC, Karakuş M, Tang HM, Ge YF, Zhang L. 2014. A new method estimating the 2D joint roughness coefficient for discontinuity surfaces in rock masses, Int J Rock Mech Min Sci., 72:191–198.

Zhang L. 2017. Engineering Properties of Rocks, Second Edition, University of Arizona, Tuscon, Arizona, United States.

Zimmer, V.L., Collins, B.D., Stock, G.M., Sitar, N., 2012. Rock fall dynamics and deposition: an integrated analysis of the 2009 Ahwiyah Point rock fall, Yosemite National Park, USA. Earth Surf. Process. Landf. 37, 680–691. http://dx.doi.org/10.1002/esp.3206.

APPENDICES

A. Generic RANSAC Algorithm

```
Given:
    data – a set of observed data points
    model – a model that can be fitted to data points
    n – the minimum number of data values required to fit the model
    k – the maximum number of iterations allowed in the algorithm
    t – a threshold value for determining when a data point fits a model
    d – the number of close data values required to assert that a model
fits well to data

Return:
    bestfit – model parameters which best fit the data (or nul if no good
model is found)

iterations = 0
bestfit = nul
besterr = something really large
while iterations < k {
    maybeinliers = n randomly selected values from data
    maybemodel = model parameters fitted to maybeinliers
    alsoinliers = empty set
    for every point in data not in maybeinliers {
        if point fits maybemodel with an error smaller than t
             add point to alsoinliers
    }
    if the number of elements in alsoinliers is > d {
        % this implies that we may have found a good model
        % now test how good it is
        bettermodel = model parameters fitted to all points in
maybeinliers and alsoinliers
        thiserr = a measure of how well model fits these points
        if thiserr < besterr {
            bestfit = bettermodel
            besterr = thiserr
        }
    }
    increment iterations
}
return bestfit
```

B. Affine_fit Algorithm

```
function [n,V,p] = Affine_fit(T)
    p = mean(T,1); %the mean of the samples belongs to the plane
    [V,D] = eig(T'*T); %Computation of the eigenvectors
    %Extract the normal vector and orthonormal basis of the plane
    n = V(:,1);
    V = V(:,2:end);
end
plot3(p(1),p(2),p(3),'bo','markersize',15,'markerfacecolor','blue');
quiver3(p(1),p(2),p(3),n(1)/3,n(2)/3,n(3)/3,'b','linewidth',2)
[S1,S2] = meshgrid([-1 0 1]);
%generate the pont coordinates
X = p(1)+[S1(:) S2(:)]*V(1,:)';
Y = p(2)+[S1(:) S2(:)]*V(2,:)';
Z = p(3)+[S1(:) S2(:)]*V(3,:)';
%plot the plane
surf(reshape(X,3,3),reshape(Y,3,3),reshape(Z,3,3),'facecolor','blue');
```

CURRICULUM VITAE

PERSONAL INFORMATION

Surname, Name: Ünlüsoy, Deniz
Nationality: Turkish (TC)
Date and Place of Birth: 19 March1987, Ankara
Marital Status: Single
Phone: +90 537 241 91 84
email: deniz.unlusoy@metu.edu.tr

EDUCATION

Degree	Institution	Year of Graduation
MS	METU Geological Engineering	2013
BS	METU Geological Engineering	2010
High School	ODTÜ Geliştirme Vakfı Lisesi	2004

WORK EXPERIENCE

Year	Place	Enrollment
2019	METU OGAM	Project Consultant
2016-2017	İşlem Coğrafi Bilgi Sistemleri	Project Consultant
2009 2010	Maden Tetkik Arama Enstitüsü	Intern Eng. Student
2008	Maden Tetkik Arama Enstitüsü	Intern Eng. Student
2006	ENVY Enerji ve Çevre Yatırımları A.Ş.	Intern Eng. Student

FOREIGN LANGUAGES

Advanced English

PUBLICATIONS

1. Ünlüsoy D. and Süzen M. L. “A New Method for Automated Estimation of Joint Roughness Coefficient for 2D Surface Profiles Using Power Spectral Density”, International Journal of Rock Sciences and Rock Mining, Volume 125, January 2020, 104156.

HOBBIES

PC Gaming, Comic book collection, Science Fiction and Fantasy Novels, Tabletop Games, Movies